8-2012

Dynamical Properties of Ferroelectric Perovskites (Ba,Sr)TiO3 and Pb(Zr,Ti)O3 Systems from First Principles

Jeevaka Weerasinghe
University of Arkansas, Fayetteville

Dynamical properties of Ferroelectric Perovskites (Ba,Sr)TiO_3 and Pb(Zr,Ti)O_3 systems from First principles

Dynamical properties of Ferroelectric Perovskites (Ba,Sr)TiO_3 and Pb(Zr,Ti)O_3 systems from First principles

A dissertation submitted in partial fulfillment
of the requirements for the degree of
Doctor of Philosophy in Physics

By

Jeevaka Lal Weerasinghe
University of Kelaniya
Bachelor of Science in Physics, 2005
University of Arkansas
Master of Science in Physics, 2009

August 2012
University of Arkansas

Abstract

A first-principles-based effective Hamiltonian scheme which incorporates coupling between ferroelectric (FE) and antiferrodistortive (AFD) motions is applied to $Pb(Zr,Ti)O_3$ alloys. It validates the existence of two modes of E symmetry (rather than the single E(1TO) soft mode) in the 50–75 cm^{-1} range for temperatures smaller than 200 K and for compositions falling within the Rhombohedral $R3c$ phase. Coupling between long-range-ordered FE and AFD motions is shown to be the cause of the additional mode and more insight into its nature is provided. This scheme is further used to reveal a field-induced anticrossing involving FE and AFD degrees of freedom for Ti composition of 45%.

Molecular dynamics (MD) simulations, across the morphotropic phase boundary (MPB) of disordered $Pb(Zr,Ti)O_3$ solid solutions at 10 K, confirms the existence of similar additional modes in the the monoclinic Cc and tetragonal $I4cm$ phases. Lifting of degeneracy of E modes in the Cc phase each giving $A' + A''$ modes is seen in accordance with group theory predictions. In particular, a compositional-induced anticrossing occurring within the bridging Cc state is revealed, and the difference in frequency between A' and A'' modes in the Cc state is linked to a quantity introduced here and termed the monoclinic depth. Analytical models are further developed to reproduce and better understand characteristics of these modes across the MPB.

Furthermore, a Fermi resonance (FR) emerging from the *nonlinear* coupling between ferroelectric motions and tiltings of oxygen octahedra is exposed. This FR manifests itself as the doubling of a nominally single FE mode in a purely FE phase, when the resonant frequency of the FE mode is close to the first overtone of the tiltings. It is shown, through the use of an analytical model (that captures the essence of the effect), that the FR is the

result of a nonlinear coupling that is proportional to the spontaneous polarization of the material.

MD simulations incorporating a first-principles-based effective Hamiltonian scheme consisting of FE and strain degrees of freedom, are conducted on (Ba,Sr)TiO_3 (BST) bulks and epitaxially strained $SrTiO_3$ (STO) thick films at finite temperature. The appearance of a central mode (CM) is confirmed and splitting of soft mode (SM) into out-of-plane and in-plane modes is predicted for strained STO films and two CM's are predicted for $Ba_{0.5}Sr_{0.5}TiO_3$ in FE phase. Symmetries of modes in FE phases originating from the soft-mode are discussed. Electrostriction energy is shown to be governing the Curie temperature T_c and determine the type of FE phase transition each system undergoes. The comparatively large electrostriction energy in BST systems is also pointed to be behind the emergence of the CM in PE phase of them.

Moreover, MD simulation are performed of BST bulks and epitaxially strained STO thick films to obtain dielectric tunability $\tau(E)$, as a function of electric field applied along the polarization. Landau-Devoshire theroy based fittings are shown to inaccurately describe $\tau(E)$ in the low-field regime and the presence of strong CM in this regime is claimed to be the cause of this discrepancy in these systems.

This dissertation is approved for recommendation
to the Graduate Council.

Dissertation Director:

Dr. Laurent Bellaiche

Dissertation Committee:

Dr. Huaxiang Fu

Dr. William F. Oliver III

Dr. Gregory J. Salamo

Dr. Douglas E. Spearot

Dissertation duplication release

I hereby authorize the University of Arkansas Libraries to duplicate this thesis when needed for research and/or scholarship.

Agreed_____

(Jeevaka Lal Weerasinghe)

Refused_____

(Jeevaka Lal Weerasinghe)

Acknowledgements

I began my doctoral studies here at the University of Arkansas in the fall of 2006. Since then there were many people who supported me academically and/or personally, without which this journey would not have been possible.

First of all, I am immensely grateful to my advisor Prof. Laurent Bellaiche. Most of my current understanding of the art of computational research of solid state materials comes from him. I learned the art of communication of one's scientific research from him. Especially, I am thankful for taking time to go through manuscripts and this dissertation, from which I learned a lot. More importantly, he is a wonderful human being, and I appreciate very much the patience and understanding he showed, especially in the first couple of years when I had a lot to learn about the research and had course work to complete.

Second, I like to say a big thank you to Prof. Huaxiang Fu. The two courses, Physics at the nanoscale and Statistical physics, not only helped gain a firm understanding of the Physics of my research but most importantly, at a time when I was lost with all the jargon and theories his way of teaching helped me develop a better perspective of what Physics research is all about.

Third, I like to thanks my committee members Prof(s). Fu, Oliver, Salamo and Spearot, from whom I received valuable advice for my research through the annual reviews held.

Fourth, I like to Thank Dr(s). Dawei Wang, Jirka Hlinka and Inna Ponomoreva. I colloborated in my research work with Dr(s). Wang and Hlinka and appreciate their advice, interaction with them helped enrich my knowledge of research matter, while Dr. Ponomoreva demonstrated initially, how to set up simulations.

Fifth, I like to thank David Chaffin and Jeff Pummil at HPC in the University of Arkansas for their ever prompt assistance in resolving HPC issues. I am very grateful to the personal

advice on meditation received from Ajahn Brahm, who is a Buddhist monk (and cambridge physics graduate) in Australia, which has helped me tremondously to keep a more balanced peaceful and happy mind under all vicissitudes of life.

Finally, but by no means the least, I like to thank my wonderful wife Raneetha and my parents Lional and Shiromi. Raneetha was also a graduate student at U. of A. and I very much appreciate the invaluable support and encouragement she gave me throughout my graduate studies. My parents, for raising me and for guiding and encouraging me throught childhood and to this day. Furthermore, I like to thank many friends who supported and adviced.

Contents

CHAPTER 1

Introduction

Ferroelectrics, recognized only in the 20th century have been extensively researched and much sought after ever since, due to their technological promise. Materials which possess a spontaneous polarization, with two or more orientational states in the absence of an electric field that can be shifted from one to another by the application of an electric field, are termed ferroelectrics. Each of the two orientational states are identical in crystal structure, differing only in the orientation of the electric polarization vector under conditions of zero electric field.

Pyroelectricity, or the possession of temperature dependent polarization, in some materials was known from ancient times and properties of pyroelectrics were investigated from the early 1800s. The realization that thermal strain causes the polarity in pyroelectrics led the Curie brothers to discover piezoelectricity in 1880 [**1**], which is the creation of electric polarity by application of stress. However, the first known proper identification of ferroelectricity was only made in 1921 in Rochelle salt by Valasek [**2**]. It is believed that the formation of domains of differently oriented polarization resulting in a lack of any net polarization in virgin single crystals was the reason for the much later discovery of ferroelectricity. Valasek realized that the dielectric properties in Rochelle salt were in many aspects similar in nature to the ferromagnetic properties of iron, in that there was a hysteresis in the field-polarization curve (see[1] Fig. 1.0.1), a transition Curie temperature T_c, and an extremely large dielectric and piezoelectric response in and near the ferroelectric region. Such analogies with ferromagnetism led to the coining of the term 'ferroelectricity' to describe these phenomena, which is a kind of misnomer since iron has nothing to do with them and is in fact absent from most known ferroelectrics.

[1]Source: Dennis L. Polla and Lorraine F. Francis, Ann. Rev. Mat. Sci. 28, 563 (1998).

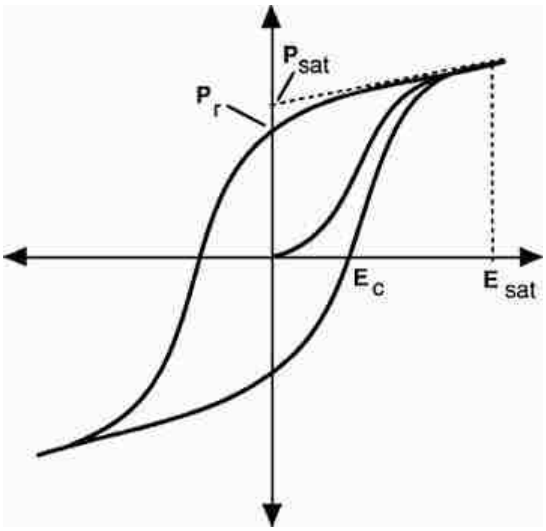

FIGURE 1.0.1. Typical polarization–electric-field hysteresis curve for ferroelectric materials (note that one should trace the curve in the anticlockwise direction). Notation: P_{sat} is the saturation polarization; P_r is the remnant polarization; E_c is the coercive field; E_{sat} is minimum field for saturation of polarization.

Except for the subsequent discovery of ferroelectricity in a series of isomorphous crystals of phosphates and arsenates, principal among them being potasium dyhydrogen phosphate (KH_2PO_4) [**3, 4**], until the mid 1940's no further discoveries of ferroelectrics were made. So there was a growing conviction that ferroelectricity was one of the great accidents of nature. All that changed with the discovery of ferroelectricity in $BaTiO_3$ by Wul and Goldman in 1945 [**5**]. This material was to become the forerunner of the largest single class of all ferroelectrics - the oxygen octahedral ferroelectrics, constituent with BO_6 building blocks (see[2] Fig. 1.0.2). More importantly, the simple 5 atom perovskite structure paved the way for some theoretical progress at the microscopic level.

1.1. Crystallography and ferroelectrics

The subset of the full symmetry group of a Bravais lattice, that contains only operations that leave a particular point fixed, is called the *point group* of the Bravais lattice. There are seven such distinct point groups that a Bravais lattice can have. They define the seven

[2] Source: T. Imai, M. Sasaura, K. Nakamura, and K. Fujiura, NTT Tech. Rev. 5, 9 (2007)

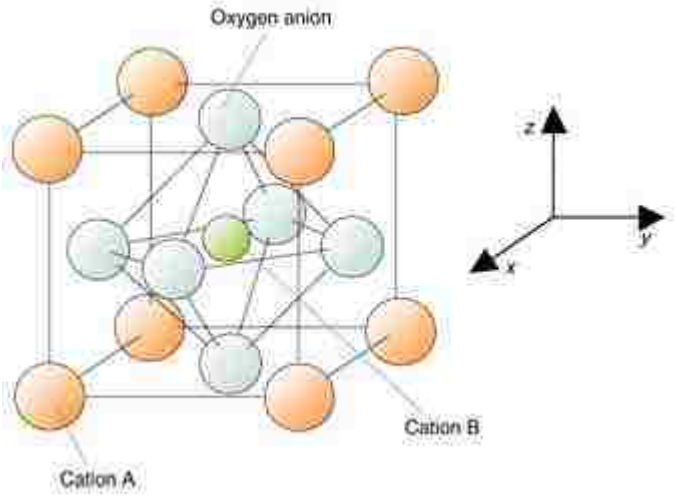

FIGURE 1.0.2. Perovskite ABO_3 structure with oxygen octahedral.

crystal systems: triclinic, monoclinic, orthorhombic, tetragonal, trigonal (also termed rhombohedral), hexagonal and cubic. Moreover, there are 32 distinct possible point groups that a general crystal structure can have. They can be divided between the seven crystal systems, based on the point group of the underlying Bravais lattice for the general structure concerned (see[3] Table 1.1.1) [**6**]. Amongst the 32 point groups, 11 possess a center of symmetry. They are termed centrosymmetric and have no polar properties. For example, if a uniform stress is applied to such a crystal, the resulting movement of charge is symmetrically distributed about the center of symmetry in a way that the relative displacements are fully compensated. All except one of the non-centrosymmetric groups displays electric polarity when subjected to stress. The effect and its converse (i.e., the production of strain by application of electric field) is linear, since reversal of the stimulus results in the reversal of the response and is termed the piezoelectric effect. Of the 20 piezoelectric crystals, 10 have a unique polar axis and they possess a spontaneous polarization (i.e., electric dipole moment per unit volume) which is temperature dependent. Thus, crystals belonging to these 10 groups are termed polar or pyroelectric. Some materials have polar crystals that have a spontaneous polarization, which can be shifted among two or more orientational states giving rise to the signature field-polarization hystersis. These are the ferroelectric crystals.

[3]Source: M. E. Lines and A. M. Glass, Principles and Applications of Ferroelectrics and Related Materials (Clarendon Press, Oxford, 1977).

Crystal System	Point Groups	Centro-symmetric	Piezoelectric	Pyroelectric
Triclinic	1, $\bar{1}$	$\bar{1}$	1	1
Tetragonal	4, $\bar{4}$, 4/m, 422, 4mm, $\bar{4}$2m, 4/mmm	4/m, 4/mmm	4, $\bar{4}$, 422, 4mm, $\bar{4}$2m	4, 4mm
Hexagonal	6, $\bar{6}$, 6/m, 622, 6mm, $\bar{6}$m2, 6/mmm	6/m, 6/mmm	6, $\bar{6}$, 622, 6mm, $\bar{6}$m2	6, 6mm
Monoclinic	2, m, 2/m	2/m	2, m	2, m
Orthorhombic	222, mm2, mmm	mmm	222, mm2	mm2
Trigonal	3, $\bar{3}$, 32, 3m, $\bar{3}$m	3, $\bar{3}$m	3, 32, 3m	3, 3m
Cubic	23, m3, 432, $\bar{4}$3m, m3m	m3, m3m	23, $\bar{4}$3m	–

TABLE 1.1.1. Crstallographic point groups classified based on polar properties.

1.2. The soft-mode theory of ferroelectricity

In 1960, Anderson [**7**] and Cochran [**8**] were the first to propose that to explain ferroelectric behavior, theory at the microscopic level should be cast within the framework of lattice dynamics and that one should focus on the lowest-frequency optical phonon mode at the center of the Brillouin zone, better known as the 'soft mode', for a particular system as the primary ferroelectric instability. Initially, this soft mode description of ferroelectricity was solely used for displacement systems, in which the static ferroelectric properties can be explained by considering systems with small structural displacements from an prototype (usually non-polar) phase. Later on, it evolved to include a fundamental model Hamiltonian which was general enough to include various ferroelectric instabilities resulting in its broader applicability across many different systems. An important aspect of the use of such a Hamiltonian was the inherent realization that ferroelectric and anti-ferroelectric (see section 1.3) transitions are particular cases of the more general concept of structural phase transitions.

The recognition of the significance of the soft mode in describing ferroelectricity triggered an explosion of experimental activity using techniques capable of measuring its frequency and/or wave vector dependent characteristics. These were primarily scattering and resonance techniques involving X-rays, neutrons, light, and ultrasound.

1.2.1. Representation of the vibrational modes. Factor group methods for calculation of symmetry properties leads to the irreducible representations of the Raman active

Crystal System	Point Groups	Representation of Raman active modes
Monoclinic	2	$A(y)$, $B(x,z)$
	m	$A'(x,z)$, $A''(y)$
	2/m	A_g, B_g
Orthorhombic	222	A, $B_1(z)$, $B_2(y)$, $B_3(x)$
	mm2	$A_1(z)$, A_2, $B_1(x)$, $B_2(y)$,
	mmm	A_g, B_{1g}, B_{2g}, B_{3g}
Trigonal	3	$A(z)$, $E(x)$, $E(y)$
	3	A_g, E_g, E_g
	32	A_1, $E(x)$, $E(y)$
	3m	$A_1(z)$, $E(y)$, $E(-x)$
	3m	A_{1g}, E_g, E_g
Tetragonal	4	$A(z)$, B, $E(x)$, $E(y)$
	4	A, $B(z)$, $E(x)$, $E(-y)$
	4/m	A_g, B_g, E_g, E_g
	422	$A_1(z)$, B_1, B_2, $E(x)$, $E(y)$
	4mm	A_1, B_1, B_2, $E(-y)$, $E(x)$
	42m	A_1, B_1, $B_2(z)$, $E(y)$, $E(x)$
	4/mmm	A_{1g}, B_{1g}, B_{2g}, E_g, E_g
Hexagonal	6	$A(z)$, $E_1(x)$, $E_1(y)$, E_2, E_2
	6	$A(z)$, E'', E'', $E'(x)$, $E'(y)$
	6/m	A_g, E_{1g}, E_{1g}, E_{2g}, E_{2g}
	622	A_1, $E_1(x)$, $E_1(y)$, E_2, E_2
	6mm	$A_1(z)$, $E_1(y)$, $E_1(-x)$, E_2, E_2
	6m2	A_1', E'', E'', $E'(x)$, $E'(y)$
	6/mmm	A_{1g}, E_{1g}, E_{1g}, E_{2g}, E_{2g}
Cubic	23	A, E, E, $F(x)$, $F(y)$, $F(z)$
	m3	A_g, E_g, E_g, F_g, F_g, F_g
	432	A_1, E, E, F_2, F_2, F_2
	43m	A_1, E, E, $F_2(x)$, $F_2(y)$, $F_2(z)$
	m3m	A_{1g}, E_g, E_g, F_{2g}, F_{2g}, F_{2g}

TABLE 1.2.1. Irreducible representations of Raman active modes for various point groups

modes given in Table 1.2.1[4]. Note that the component of phonon polarization for these modes, which are also infrared active, is given in brackets after the symbol of the representation.

[4]Source: M. E. Lines and A. M. Glass, Principles and Applications of Ferroelectrics and Related Materials (Clarendon Press, Oxford, 1977).

1.3. Structural phase transitions

Structural phase transitions associated with the condensation (in the Bose-Einstein sense) of a zone center soft mode (SM) are generally termed ferrodistortive. Ferroelectric phase transitions involve the condensation of the lowest polar mode, which causes the long-range polar order. Therefore, in this view, ferroelectric transitions can be considered as a subgroup of ferrodistortive transitions. If the phase transition has the signature of a mode condensation that is located at a point other than at the center of the Brillouin zone, the transition is called antidistortive or sometimes antiferrodistortive. More often than not, such off-center condensation occurs at the Brillouin zone boundary of the high temperature phase, accompanied by the doubling of the unit cell for the system. If the condensing zone boundary mode is polar, the transition is called antipolar. In addition to being antipolar, if the system exhibits large dielectric anomalies near Curie temperature T_c, and if it can be transformed to an induced ferroelectric phase, by the application of an electric field, then the transition is called antiferroelectric.

1.3.1. Ferroelectric phase transitions. In addition to lowest polar mode condensation that occurs at the zone center, as the temperature is reduced above the Curie point T_c, often the approaching phase transition is signalled by a diverging differential dielectric response or permittivity $\varepsilon(0)$. The phase corresponding to this divergence for the region of temperature, above T_c is generally named the *paraelectric* phase. Closer to T_c, zero-field dielectric constant, $\varepsilon(0)$ is found to vary in an approximate Curie-Weiss manner described by:

$$\varepsilon(0) = \frac{C}{T - T_0} \tag{1.3.1}$$

where T_0 is the Curie-Weiss temperature and C is the Curie-Weiss constant. T_0 is equal to the Curie temperature T_c only when the polarization changes continuously across the

transition. This type of phase transition is named a *second-order* phase transition. Conversely, if the polarization changes abruptly at T_c , such transitions are named *first-order* phase transitions and for these, T_0 is usually greater than T_c, as will be clear when we discuss phenomenology of ferroelectric phase transitions in section (1.5).

If the transition is very strongly of first-order character, then condensation of the soft mode may not be observed noticeably close to T_c, unlike in the case of continuous second-order transitions. For such transitions, there is also the possibility that the large polarization that sets in discontinuously at T_c may not be reversible, hence the low temperature phase may only be pyroelectric.

Below T_c, in the absence of an electric field, there are at least two directions along which a spontaneous polarization can develop. Hence, for some systems, it is found that different regions of it are polarized in each of these available directions in order to minimize the depolarizing field, that originates from accumulated surface charge. These regions of uniform polarization are called *domains* and the resulting *domain structure* usually causes the near total compensation of macroscopic polarization.

1.3.2. Order-disorder versus displacive ferroelectrics. Ferroelectrics can be categorized as either *order-disorder* or *displacive* based on the atomic displacements in the paraelectric phase. If the paraelectric (PE) phase is microscopically non-polar, the system concerned is termed a displacive ferroelectric, whereas if it is only macroscopically non-polar but possesses disordered microscopic polarity in the PE phase, then it is termed a order-disorder ferroelectric. With regard to the dynamics of the soft mode, displacive ferroelectrics have a propagating soft mode, while order-disorder ferroelectrics have a diffusive (non-propagating) soft mode. In the order-disorder case, the soft mode in fact is not a phonon at all, but corresponds to large amplitude hopping motions between the potential wells of the system. Practically, many ferroelectrics are found to fall somewhere between these two extremes, thus having features of both categories, a prime example being bulk $BaTiO_3$.

1.4. Complex dielectric function

For isotropic crystals, measurements of specular normal reflectivity spectra, $R(\omega)$, are related to the complex dielectric function $\varepsilon(\omega)$, as follows :

$$R(\omega) = \left| \frac{\sqrt{\varepsilon(\omega)} - 1}{\sqrt{\varepsilon(\omega)} + 1} \right|^2 \tag{1.4.1}$$

In order to determine mode characteristics, the standard procedure is to use simple physically acceptable models for the dielectric function $\varepsilon(\omega)$, and fit them directly to the reflectivity spectrum, which has been found to be more accurate and convenient than the converse approach of Kramers–Kronig analysis over a broad-enough frequency range of reflectivity data. For a dielectric material, the dielectric function usually contains contributions from polar phonons and electron-shell vibrations about the ionic cores. The frequency dependence of $\varepsilon(\omega)$, in the low frequency infrared (IR) region can usually be modelled by considering both polar phonon and electronic contributions as sums of simple damped harmonic oscillators. The restoring forces for polar and electronic vibrations are of comparable magnitude, but the much smaller electronic mass causes the electronic oscillations to occur at much higher frequencies than polar resonant frequencies. Thus, the total electronic contributions in the IR regime can be safely approximated by a constant. Therefore, the linear dielectric function $\varepsilon(\omega)$, in this frequency regime can be given as follows:

$$\varepsilon(\omega) = \varepsilon_\infty + \varepsilon_{ph} = \varepsilon_\infty + \sum_j \frac{S_j \omega_j^2}{\omega_j^2 - \omega^2 - i\omega\gamma_j} \tag{1.4.2}$$

where ω_j,γ_j and S_j are resonant frequency, damping constant and dielectric strength of the j-th polar phonon mode, respectively. In modelling the dielectric function for some materials, it is important to account for contributions from dielectric relaxations, which are

particularly important in some ferroelectrics, relaxors and all kinds of inhomogeneous materials (ceramics, composites) at lower frequencies. Considering each to be a Debye relaxation, their contribution can be given as follows:

$$\varepsilon_{dr}(\omega) = \frac{S_r}{1 + i\omega/\omega_r} \tag{1.4.3}$$

where ω_r and S_r are frequency and dielectric strength of the Debye relaxation. For some spectra however, it is necessary to consider coupling between relaxation and the soft mode when modelling the dielectric function. Methods for how this is done will be discussed in section (4.1).

1.5. Phenomenological theory of ferroelectrics

In his now classic papers [**9, 10**] published in 1937, Landau notes that a system cannot change smoothly between two phases of different symmetry and that the continuous path a system can take between liquid and gaseous states is only possible because there is no symmetry change involved. Furthermore, since two symmetrically distinct phases must share the same thermodynamic state at their shared transition temperature, the symmetry of one of them must be higher than that of the other. Landau characterized this transition in terms of an *order* parameter–an internal physical property, that is zero in the high-symmetry phase and non-zero in the low-symmetry phase, with a continuous transition between these phases for the system concerned. For example, in the case of ferroelectric transitions, this order parameter is the polarization P. The free energy Φ, in the vicinity of the transition, was then given as a power series of the order parameter, where only terms compatible with the symmetry for a particular system is retained. Landau's approach is attractive since it allows linking of the measurable thermodynamic quantities near phase transition (PT) via coefficients of the series expansion.

Landau's symmetry based treatment of PT's was first applied to ferroelectrics by Devonshire [**11, 12, 13**]. In general, the thermodynamic state of any system in equilibrium can be

specified by the use of specific variables. For bulk ferroelectrics, they are the temperature (T), polarization ($\vec{P}$), electric field ($\vec{E}$) , strain (η) and the stress (σ). Using the free energy Φ of the unpolarized and unstrained system as the reference, Landau-Devonshire theory expresses Φ of a ferroelectric as a function of (η) and ($\vec{P}$) as follows:

$$\begin{aligned}\Phi(P,\eta) =& \frac{1}{2}\alpha_{ij}P_iP_j + \frac{1}{3}\delta_{ijk}P_iP_jP_k + \frac{1}{4}\beta_{ijkl}P_iP_jP_kP_l + \frac{1}{5}\omega_{ijklm}P_iP_jP_kP_lP_m \\ &+ \frac{1}{6}\gamma_{ijklmn}P_iP_jP_kP_lP_mP_n + \frac{1}{2}c_{ijkl}\eta_{ij}\eta_{kl} - a_{ijk}\eta_{ij}P_k - \frac{1}{2}q_{ijkl}\eta_{ij}P_kP_l - \vec{P}\,.\,\vec{E} - \sigma\,.\,\eta \end{aligned} \tag{1.5.1}$$

where α_{ij}, β_{ijkl}, γ_{ijklmn}, δ_{ijk} and ω_{ijklm} are the phenomenological Landau-Devonshire coefficients and c_{ijkl}, a_{ijk} and q_{ijkl} are respectively, the elastic, piezoelectric and electrostatic constant tensors. If the high symmetry parent phase is centrosymmetric, all odd terms are removed :

(1.5.2)

$$\Phi(P,\eta) = \frac{1}{2}\alpha_{ij}P_iP_j + \frac{1}{4}\beta_{ijkl}P_iP_jP_kP_l + \frac{1}{6}\gamma_{ijklmn}P_iP_jP_kP_lP_mP_n + \frac{1}{2}c_{ijkl}\eta_{ij}\eta_{kl} - \frac{1}{2}q_{ijkl}\eta_{ij}P_kP_l - \vec{P}\,.\,\vec{E} - \sigma\,.\,\eta$$

suppose the polarization is directed only along one of the crystallographic axes, then we can simplify further :

$$\Phi(P,\eta) = \frac{1}{2}\alpha P^2 + \frac{1}{4}\beta P^4 + \frac{1}{6}\gamma P^6 + \frac{1}{2}c\eta^2 - \frac{1}{2}q\eta P^2 - PE - \sigma\eta \tag{1.5.3}$$

now let's consider a stress free state (i.e., $\sigma = 0$) at equilibrium:

$$\frac{\partial\Phi(P,\eta)}{\partial\eta} = 0 \Rightarrow \eta = \frac{qP^2}{c}$$

substituting in Eqn.(1.5.3) gives:

$$\Phi(P,\eta) = \frac{1}{2}\alpha P^2 + \frac{1}{4}\left(\beta - \frac{2q^2}{c}\right)P^4 + \frac{1}{6}\gamma P^6 - PE \tag{1.5.4}$$

Through experimental fittings of dielectric constant, $\varepsilon(0)$, in the paraelectric phase, it is assumed that in the Landau-Devonshire theory, α can be expressed as follows:

$$\alpha = \alpha_0 (T - T_0) \tag{1.5.5}$$

Phase transition characteristics of clamped systems, such as epitaxially strained systems which are forced to have in-plane lattice constants matched to that of the substrate and is free to relax only in the out-of-plane direction can usually be described by Eqn.(1.5.4) given the above mentioned requirements are met. Examining the coefficient of P^4 in this equation, we can see how the phase transition characteristics are effected when a system is clamped. For example, if the unclamped system has a first-order transition ($\beta < 0$), clamping can result in making it even more first-order (i.e., enhanced discontinuity of P at T_c) and increase T_0. Furthermore, even the type of transition can be changed, for example if ${}^{2q^2}/_{c} > \beta > 0$, a first-order transition can become second-order when the system is clamped.

1.6. Applications of ferroelectrics

Ferroelectrics are attractive candidates for a variety of device applications due to numerous technologically important properties that they have. However, currently the great majority of these applications use the inherent piezoelectric or pyroelectric properties rather than the defining characteristic of switchable polarization of ferroelectrics. Some of the main applications of these materials are described hereafter [**6, 14**].

1.6.1. Pyroelectric detectors and thermal imaging. Although at present, single crystals of triglycine sulphate (TGS), $LiTaO_3$ and $(Sr,Ba)Nb_2O_6$ are more widely used for heat sensing applications, the use of ferroelectric thin films are more advantageous because of the high cost of growing single crystals. Studies of ferroelectric $PbTiO_3$, $(Pb,La)TiO_3$ and $Pb(Zr,Ti)O_3$ have shown a lot of promise for such thin-film application. Ferroelectrics are also used for infrared imaging, where polarization changes caused by thermal energy is the principle mechanism of operation.

1.6.2. Ultrasound device for medical imaging. The development of array transducers based on piezoelectric characteristics of ferroelectrics and their miniaturization to increase resolution has been the key for modern high quality ultrasound imaging, which has become invaluable in medical diagnosis and therapy. Crucially, piezoelectric materials enable the transducer to perform both active (sound transmission) and passive (sound reception) functions at the same time.

1.6.3. Ferroelectric memory. Presently, semiconductor memories such as dynamic random access memories (DRAM) and static random access memories (SRAM) dominate the market, despite being volatile. FLASH memory, even though highly successful, is not the long term non-volatile memory of choice, because of limitations in endurance and scalability. Ferroelectric random access memory (FeRAM) uses the switchability of the polarization via an external electric field to store data, and more importantly it is non-volatile. However, in FeRAM the read-out operation is destructive because, to determine the polarization state, it is necessary to attempt to switch the polarization, which means the data stored is then erased and must be re-written. Moreover, as ferroelectrics can suffer from fatigue with repetitive cycling, this destructive read-out places a limitation on the reliability. Even though over the years fatigue resistance has been improved by the use of oxide electrodes, further advancements must be made if FeRAM is to take over as the non-volatile memory of choice.

1.6.4. Tunable capacitors. The high electric-field tunability due to the sensitive nonlinear dielectric constant of ferroelectrics close to Curie temperature makes them extremely attractive candidates for tunable capacitors or varactors in the microwave regime. However, the high loss, compared to that of semiconductor alternatives and mainly the high voltage needed for tunning has limited the commercial use of ferroelectric varactors.

1.6.5. Microwave ferroelectric phase shifters. A phased array antenna consists of thousands of radiating elements, which should be served by phase array shifters. The phase shifters modify and control the width and angle of the steered radar beam. Currently, these phase shifters are housed semiconductor modules. Nevertheless, the use of ferroelectric films

as alternatives is being thoroughly investigated, since these films enable the integration of phase shifters with microwave circuits on one substrate leading to the substantial reduction of the size, mass and cost of these antennas.

1.7. First-principles simulations of perovskite ferroelectrics

The most widely investigated FE materials are the perovskite oxides of form ABO_3 (e.g., $BaTiO_3$). In the paraelectric phase, they all have a simple cubic structure with metal A at the cube corners, metal B (usually a transition-metal) at the cube center, and O atoms at the cube faces (see Fig. 1.0.2). As the temperature is reduced, a ferroelectric phase transition takes place, where the material develops a spontaneous electric polarization P, mainly from the off-center displacement of B atom with respect to the surrounding oxygen octahedron. For some materials (e.g., $PbTiO_3$) there is a single such transition, while in others (e.g., $BaTiO_3$) there are multiple FE transitions, corresponding to different selections of orientation for P as the temperature is reduced [**6**]. In addition, antiferrodistortive instabilities, involving a rotation of the oxygen octahedra, can also occur in some of these materials (e.g., $PbZrO_3$, $SrTiO_3$). Although structural phase transitions and ferroelectric properties of perovskite ferroelectrics have been subjected to extensive experimental and theoretical investigations, the theoretical studies have been mainly of an empirical character. Until recently, a model Hamiltonian (such as an empirical lattice-dynamical model) was typically fit to reproduce certain experimental features, and then used to broaden the understanding or predict new properties [**6**]. Even though this approach has been rather useful, forms of these phenomenological Hamiltonians were constrained by available experimental data. Thus, oversimplification of the Hamiltonian and ambiguity are major drawbacks. In recent years, first-principles approaches have been developed and have been shown to be valuable tools in expanding our understanding of ferroelectrics at the microscopic level. In brief, these approaches are based on the solution for the quantum-mechanical ground state of the system within the local density approximation (LDA) using the Kohn-Sham density-functional theory (DFT) [**15**]. In principle, the atomic numbers of the constituent atoms are

the only inputs required for this method. The breakthrough that allowed the use of DFT for ferroelectrics is the modern theory of the polarization [**16, 17, 18**]. Formulation of a proper quantum mechanical approach for the calculation of the electronic polarization in periodic solids was a challenging problem until the early 1990s. The modern theory of polarization in which the polarization of continuous periodic electronic charge densities was mapped to a Berry phase of the Bloch functions provided an elegant solution to this problem [**16**]. This technique is now applied to access various quantities such as the spontaneous polarization, the Born effective charges or the piezoelectric tensors. However, pure DFT approaches have their limitations. The most important one is that considering explicitly the electronic degrees of freedom, currently only a limited number of atoms (of the order of a hundred atoms) can be handled in a first-principles calculation. This imposes serious restrictions on the application of pure DFT calculations for the study of many technologically important ferroelectrics, since many of them are complex solid solutions such as (Ba,Sr)TiO_3 (BST), a leading candidate for dynamical random access memories (DRAMs), and Pb(Zr,Ti)O_3 (PZT), which is widely used in transducers and actuators. In spite of the rapid increase of computational power, study of these complex materials is limited to a few artificially ordered supercells which is inadequate for an accurate description. Furthermore, determination of structural phase transitions and finite temperature properties are required for meaningful comparison with experiment, which at the moment is unaffordable within DFT, mainly because the simulation box is not large enough to properly describe random thermal vibrations. In this context, the formulation of a microscopic effective Hamiltonian approach for ferroelectrics was a significant breakthrough for predictions of finite temperature properties. Initially designed by Rabe and Joannopoulos for GeTe [**19**], the technique was generalized and first applied to ferroelectric perovskites by Zhong, Vanderbilt and Rabe [**20**]. In this approach, the zone center soft mode is considered as the driving force for the phase transitions. The Hamiltonian is constructed from a Taylor expansion of the energy around the paraelectric phase in terms of the soft mode polar degree of freedom and the strains. All parameters that appear in the expansion are determined from DFT total energy calculations. The effective

Hamiltonian makes it possible to study the structural phase transitions of ferroelectrics and the temperature dependence of their properties (dielectric, piezoelectric, and optical) [**21**]. It provides also access to complex disordered solid solutions and to nanostructures via the alloy effective Hamiltonian approach [**22**]. The effective Hamiltonian is subjected to Monte Carlo (MC) or molecular dynamics (MD) simulations in order to determine the finite-temperature ferroelectric properties of a particular perovskite. The effective Hamilton approach has been remarkably successful in predicting finite-temperature properties in many perovskites. Application to $BaTiO_3$ for example, produced the exact phase transition sequence and gave transition temperatures of 385 K, 280 K and 230 K that were in good agreement with the experimentally known values of 400 K, 280 K and 180 K [**23**]. Moreover, molecular dynamics simulations confirmed the relaxational central mode (CM) observed through spectroscopic measurement and provided insight into the origin of this mode [**24**]. Alternative methods have been reported for the study of ferroelectrics: shell-model calculations fitted on first-principles results similarly allowed Tinte et al., to access their finite-temperature properties with good accuracy [**25**], and a phenomenological model based on the chemical rules obtained from DFT allowed Grinberg et al., to reproduce the behavior of PZT structures [**26**]. However, the effective Hamiltonian approach remains one of the most efficient and used approaches.

1.8. Objectives

$Pb(Zr,Ti)O_3$ (PZT) solid solutions are of immense technological importance primarily due to the huge electromechanical coefficients they have for compositions across the morphotropic phase boundary (MPB), which is a narrow composition region centered at Ti 50% at low temperature in the temperature-composition phase diagramm where many different ferroelectric phases exist. Even though PZT has been thoroughly investigated, both through numerous diffraction and spectroscopic approaches, the exact nature of the temperature-composition phase diagram near its MPB is still disputed and origins of some of the low frequency modes are unsubstantiated. Thus, the author attempts through a first-principles

effective Hamiltonian molecular dynamics approach to resolve some of these issues and make predictions, the verification of which can broaden the fundamental understanding of this important material.

(Ba,Sr)TiO_3 (BST) solid solutions are arguably the most widely examined materials among ferroelectrics. Yet, solid fundamental understanding of some spectroscopic observations are still elusive, an example being the nature and origin of the central mode (CM) in these systems. Epitaxially strained $SrTiO_3$ (STO) films have been the subject to extensive research in recent years, due to the discovery of room temperture ferroelectricity, which is very promising for technological applications because STO single crystals are found to be easier to synthesize. Appearance of a CM has also been reported for these films. Moreover, although both BST solid solutions and STO films are highly sought after for tunable applications, currently little work has been done to extend the fundamental understanding of dielectric tunability of these systems. Therefore, the author attempts, through a first-principles effective Hamiltonian molecular dynamics scheme, to provide microscopic insight into the origin and nature of the CM observed and extend the fundamental understanding of dielectric tunability of these systems.

This work is organized as follows: In chapter 2, the first-principles effective Hamiltonian schemes used to investigate both PZT and BST systems will be described; Results for PZT systems will be discussed in chapter 3; Results for BST systems will be discussed in chapter 4; Summary and concluding remarks on the investigations will be given in chapter 5.

CHAPTER 2

Methods of investigation

An alloy effective Hamiltonian is at the heart of the approach to investigate dynamical properties of perovskite structures. It is composed of the degrees of freedom, and their couplings, which are most relevant to the structure and properties under investigation. All parameters of each Hamiltonian used have been derived from first-principles calculations on relatively small cells (i.e., up to 40 atoms). The first-principles method used is the plane-wave ultrasoft-pseudopotential method [**27**] within the local density approximation [**28**](LDA) using the Virtual Crystal Approximation (VCA) approach [**29**]. The effective Hamiltonian is incorporated into a Monte Carlo (MC) scheme [**30**] to investigate static properties, for instance, the ground state ferroelectric phase at low temperature. It is incorporated into a molecular dynamics (MD) scheme in which Newton's equations of motion are solved for all the variables present in the effective Hamiltonian [**31, 32**] to investigate dynamical properties like phonon frequencies. Both MC and MD codes are written in Fortran. The MC code is designed for serial execution while the MD code used has been parallized using the message passing interface (MPI) parallel programming model. Simulations were run on Linux supercomputers, Star and Razor at the University of Arkansas. Further details of the effective Hamiltonian and simulations are given in the following subsections.

2.1. Disordered (Ba,Sr)TiO_3 bulk and epitaxially strained $(BaTiO_3)_m/(SrTiO_3)_n$ superlattices

The Alloy effective Hamiltonian used to determine dynamical properties of (Ba,Sr)TiO_3 (BST) has two main terms contributing to the total energy (E_{tot}) and can be written as follows [**23**]:

(2.1.1) $$E_{tot} = E_{VCA}(\{u_i\},\{v_i\},\{\eta_H\}) + E_{loc}(\{u_i\},\{v_i\},\{\eta_{loc}\},\{\sigma_j\})$$

where $\{u_i\}$ denotes the Ti-centered local soft mode in the unit cell i (which is directly proportional to the electric dipole at the cell and is associated with the lowest TO phonon branch); $\{v_i\}$ are dimensionless displacement variables located at the cell corner and are used to calculate the inhomogeneous strain tensor,$\{\eta_I\}$ in cell i; $\{\eta_H\}$ is the homogeneous strain tensor which allows the simulation cell to vary in size and shape [**20**]; σ_j characterizes the atomic configuration where σ_j=+1 or -1 corresponds to the presence of a Ba or Sr atom, respectively, at the A-lattice site j and $\{\eta_{loc}\}$ characterizes the strain resulting from the difference in ionic size between Ba and Sr atoms, which is relatively large ($\sim 2\%$) [**23**]. E_{VCA} gives the total energy of $Ba_{0.5}Sr_{0.5}TiO_3$ resulting from the application of the virtual crystal approximation, in which an alloy of the form $(A',A'')BO_3$ is replaced by a uniform but composition dependent "virtual" <A>BO_3 system [**29, 33**], so that the analytical expression successfully used in Ref. [**20**] for simple ABO_3 systems can be used in the case of an alloy. E_{VCA} thus consists of five parts: a local-mode self-energy that includes quadratic and quartic terms in u_i, a long-range dipole-dipole interaction, a short-range interaction between soft modes which is quadratic in u_i, an elastic energy which is quadratic in η_H and η_I, and an interaction between the local modes and local strain$\{\eta_l\}$ which is linear in strain and quadratic in local modes [**20**]:

(2.1.2) $$E_{VCA} = E^{self}(\{u_i\}) + E^{dip}(\{u_i\}) + E^{short}(\{u_i\}) + E^{elas}(\{\eta_l\}) + E^{int}(\{u_i\},\{\eta_l\})$$

E_{loc} can be thought of as the perturbation for the VCA term leading to the approximation of the total energy for *any* alloy configuration of BST [**23**]. E_{loc} is made of three parts: perturbation of local modes $\{u_i\}$ by configuration $\{\sigma_j\}$, perturbation of inhomogeneous strain $\{v_i\}$ by configuration $\{\sigma_j\}$, and interaction between local modes $\{u_i\}$ and the strain $\{\eta_{loc}\}$ arising from the relatively large size difference between Ba and Sr ions.

$$E_{loc} = E^{\sigma u}(\{\sigma_j\},\{u_i\}) + E^{\sigma v}(\{\sigma_j\},\{v_i\}) + E^{ionic}(\{\eta_{loc}\},\{u_i\}) \tag{2.1.3}$$

Previous Monte Carlo (MC) simulations of BST based on this effective Hamiltonian have produced phase transition temperatures and sequences in excellent agreement with experimental observations [**23**]. Therefore MC simulations using Eqn. (2.1.1) are first conducted to investigate an alloy with a specific Sr concentration in the following manner: a supercell of dimensions $n_x \times n_y \times n_z$ (i.e., unit cells per side) is first generated and stored in file 'BOX'. Secondly, a random disordered alloy configuration for this supercell is generated and stored in file 'Alloy'. Third, matrices associated with long range dipole-dipole interactions for this supercell are calculated and stored in file 'DIP'. These files along with two additional files ('PARAMS' and 'MCINP') are used as inputs for the MC code. The PARAMS and MCINP files contain parameters for effective Hamiltonian and parameters for simulation respectively [**23**].

In order to simulate epitaxially strained $(BaTiO_3)_m/(SrTiO_3)_n$ superlattices, a suitably configured Alloy file is generated by merging together Alloy files generated for $(BaTiO_3)_m$ and $(SrTiO_3)_n$ in the appropriate order. Biaxial strain in the plane perpendicular to the z-axis, growth direction, in each layer is forced to match that of the substrate, which is accomplished by giving the substrate lattice constant in PARAMS file and by means of a file 'strainINHOSL', which gives the biaxial strain in each layer (say layer i) due to deviation of $\eta_{loc}(i)$ from the 'ionic' averaged strain of the whole system denoted, η'_{loc} [**34**].

Simulations are conducted under a negative external pressure of -5.2 GPa to correct for the underestimation of the lattice parameter from local density approximation [**23**]. When executed, the MC code calculates the resulting energy change for a random displacement of one of the degrees of freedom ($\{u_i\},\{v_i\}$ or $\{\eta_H\}$). If the net energetic change is negative, the change in the degrees of freedom is saved, otherwise the displacement is rejected, unless another random call a gives a number that is less than $e^{\frac{\triangle E}{kT}}$, where k is the Boltzmann's

constant and T is the temperature in Kelvin. This process is repeated for each degree of freedom and for each site.

MC simulations are first conducted at a temperature well above the Curie temperature (T_c) for this alloy. Then reducing the temperature by small steps, simulations are conducted for each temperature down to 10 K. The length of an individual simulation is 120000 steps. The output of the MC simulation are the homogeneous strain tensor $\{\eta_H\}$ and the local mode vectors $\{u_i\}$. Molecular dynamics (MD) simulations are then conducted, using all of the input files of MC simulation except MCINP, which contain simulation parameters for MC simulation, as inputs. Instead simulation parameters are given in file 'MDINP' for MD simulation. A brief description follows: first the alloy is equilibrated at a given temperature through running N_{NPT} MD steps with a thermostat and barostat activated in order to mimic a canonical ensemble (NPT). The barostat is implemented by allowing the homogeneous strain variables to relax, while the thermostat implemented is the Evans-Hoover thermostat [**35, 36, 37**]. MD simulations within NPT ensemble are conducted for all of the temperatures for which MC simulations were carried out beginning with the same initial temperature and going down to 10 K. The output of the simulation are the homogeneous strain tensor $\{\eta_H\}$ and the local mode vectors $\{u_i\}$as a function of time. Phase transition temperatures, phase transition sequence, averaged local modes and averaged homogeneous strain obtained from simulations were then checked with that obtained by MC simulation for consistency. Barring any discrepancy, the thermostat and barostat are then switched off and N_{EQ} MD steps are conducted within the microcanonical ensemble (NVE) for the system to reach equilibrium at a constant energy, E. Further N_{NVE} MD steps are then conducted to derive time-dependent properties of the alloy. Each MD step was chosen to be 0.5 fs. MD code is designed to simulate systems subjected to an electric field by including a term for the energy of the local dipoles in the external field, E in the effective Hamiltonian. To conduct simulations when the system at a certain temperature is subjected to an electric field, the output NPT configuration at this temperature is first obtained for zero field as described above, and then

the electric field is gradually increased in magnitude along a direction of interest through specification of the x, y and z components of the electric field in the MDINP file.

Once the NVE output of MD simulations are obtained for a temperature and electric field of interest, complex dielectric response in the gigahertz /terahertz regime was derived using the following formula as detailed in Ref. [**31**];

$$\begin{aligned}\varepsilon_{\alpha\beta}(\nu)-1=&\frac{1}{\varepsilon_0 V k_B T}\left[\left\langle d_\alpha(t)\, d_\beta(t)\right\rangle\right.\\ &\left.+\, i2\pi\nu\int_0^\infty dt e^{i2\pi\nu t}\left\langle d_\alpha(t)\, d_\beta(0)\right\rangle\right]\end{aligned} \tag{2.1.4}$$

where ν is the frequency, α and β represent cartesian components, V is the volume in atomic units, T is the temperature and t is time. d_α is the α component of the dipole moment of the supercell and is given by $d_\alpha(t) = Z^* u_\alpha(t)$, where Z^* is the Born effective charge associated with the local mode u_α. $d_\alpha(t)\, d_\beta(0)$ is the dipole moment autocorrelation function (ACF), where for simulation of (Ba,Sr)TiO_3 (BST), it was set to a domain in which t varies from 0 to t_0 in steps of 0.5 fs, value of t_0 was set to capture all resonances arising from the local soft mode. '$\langle\rangle$'represents thermal averaging. For simulation of BST averaging was done over n_{ave} individual autocorrelation functions spread throughout NVE in order to obtain "well behaved" dielectric response.

Peaks of complex dielectric response thus derived was fitted using classical damped harmonic oscillators (DHO) of the form $\varepsilon(\nu) = S\nu_r^2/\left(\nu_r^2 - \nu^2 + i\gamma\nu\right)$ where ν_r, γ, and S are the resonant frequency, damping constant and strength of the corresponding mode, respectively (see section (1.4)). On occasions, when a peak resembled a relaxation, an overdamped oscillator Debye relaxation of the form $\varepsilon_R(\nu) = S_R\nu_R/(\nu_R + i\nu)$ was added to account for the additional dispersion, where S_R is the strength of the relaxation, and ω_R is the relaxation frequency. Form of dielectric function for such responses will be discussed in detail in section (4.1), where we would encounter them.

2.2. Disordered Pb(Zr,Ti)O_3 bulk

The alloy effective Hamiltonian utilized to investigate finite-temperature, dynamical properties near the morphotropic phase boundary (MPB) of disordered Pb(Zr,Ti)O_3 solid solutions includes, in addition to the ferroelectric (FE) degrees of freedom discussed in section 2.1, the antiferrodistortive (AFD) motions and their couplings with FE degrees of freedom. Total energy of the structure given by the Hamiltonian is the one discussed in Ref. [**38**] and has the following form:

(2.2.1)

$$E_{tot} = E_{FE}\left(\{u_i\},\{v_i\},\{\eta_H\},\{\sigma_j\}\right) + E_{AFD}\left(\{\omega_i\},\{v_i\},\{\eta_H\},\{\sigma_j\}\right) + E_C\left(\{u_i\},\{\omega_i\}\right)$$

where u_i, $\{v_i\}$and $\{\eta_H\}$have their usual meaning (see section 2.1); σ_j characterizes the atomic configuration where σ_j=+1 or -1 corresponds to the presence of a Zr or Ti atom, respectively, at the B-lattice site j [**39**]; $\{\omega_i\}$ is a (B-centered) vector characterizing the direction and magnitude of the AFD motions in unit cell i [**38**]. E_{FE} gathers the energy terms solely involving the local mode, strain, atomic configuration and their mutual couplings and is similar to the form of E_{tot} for (Ba,Sr)TiO_3 [**23**], except for the fact that E^{ionic} is omitted. E_{AFD} gathers terms involving AFD motions and their couplings with strain and atomic configuration. It consists of four parts: self-energy associated with AFD motions $\{\omega_i\}$, the short-range interaction energy between AFD degrees of freedom, the interaction energy between strain$\{\eta_l\}$ and AFD motions, and interaction between AFD motions and atomic configuration$\{\sigma_j\}$. Thus E_{AFD} has the following form:

(2.2.2) $$E_{AFD} = E^{self\omega}(\{\omega_i\}) + E^{short\omega}(\{\omega_i\}) + E^{int\omega}(\{\omega_i\},\{\eta_l\}) + E^{\sigma\omega}(\{\omega_i\},\{\sigma_j\})$$

E_C gives the interaction energy between local modes and AFD motions. It is of particular relevance to our investigation since it characterizes the interaction between FE and AFD

degrees of freedom, thus heavily influencing the low frequency modes arising from them. E_C is given by:

$$E_C\left(\{u_i\},\{\omega_i\}\right)=\sum_i \sum_{\alpha,\beta,\gamma,\delta} D_{\alpha\beta\gamma\delta}\omega_{i,\alpha}\omega_{i,\beta}u_{i,\gamma}u_{i,\delta} \tag{2.2.3}$$

where i denotes an arbitrary unit cell and $\alpha,\beta,\gamma,$ and δ denote Cartesian components. The first three terms of Eqn.(2.2.2) and E_C are terms resulting from the use of the virtual crystal approximation, VCA (via averaging of the Zr and Ti potentials) to mimic $PbZr_{0.5}Ti_{0.5}O_3$ by a hypothetical simple Pb<B> O_3 system [**29**].

Previous usage of this effective Hamiltonian in Monte Carlo (MC) simulations of PZT [**38**] produced transition temperatures to FE phases which were compatible with experimental observations [**40, 41**]. In addition, the phases P4mm, R3m, R3c, Cm, Cc and I4cm predicted were in remarkable agreement with various spectroscopic measurements with respect to both composition and temperature [**40, 41, 42, 43, 44, 45, 46, 47, 48**]. Thus to investigate a Pb(Zr,Ti)O_3 alloy of specific Ti concentration, Monte Carlo (MC) simulations are first conducted on a supercell of dimentions $12\times12\times12$ based on the total energy of Eqn. (2.2.1), following the same procedure described in section 2.1. Key differences with respect to the MC simulation using Eqn. (2.1.1) are: (1) since the local mode self energy has contributions from alloying of the VCA hypothetical Pb<B>O_3 system one needs to determine coupling parameters α and γ for each alloy. (2) For each alloy one needs to determine two sets of α and γ parameters-one for Ti and one for Zr. (3) Both MC, as well as, MD simulations are conducted under negative external pressure of 4.68GPa to correct for the underestimation of the lattice parameter from local density approximation (LDA). MC simulations are first conducted at a temperature well above the Curie temperature (Tc) for this alloy. Then reducing the temperature by small steps, simulations are conducted for each temperature down to 10 K. The length of an individual simulation is 1000000 steps[1]. Outputs of the MC procedure are the homogeneous strain tensor $\{\eta_H\}$, the $\langle\mathbf{u}\rangle$ supercell average of the local

[1]A large number of MC steps was needed to obtain well converged results

mode vectors $\{u_i\}$, and the $\langle\omega\rangle_R$ vector defined as $\langle\omega\rangle_R = \frac{1}{N}\sum_i \omega_i (-1)^{n_x(i)+n_y(i)+n_z(i)}$, where the sum runs over the N sites i and n_x(i), n_y(i) and n_z(i) are integers locating the cell i (i.e., the B-site i is centered at $\left[n_x(i)\hat{i} + n_y(i)\hat{j} + n_z(i)\hat{k}\right] a$, where a is the lattice constant of PZT and $\hat{i}$, $\hat{j}$and $\hat{k}$ are unit vectors along the Cartesian axes). Note that the magnitude of $\langle\omega\rangle_R$ corresponds to the angle of oxygen octahedra tilting and its direction is the axis of antiphase tilting. A nonvanishing $\langle\mathbf{u}\rangle$ indicates ferroelectricity while a nonzero $\langle\omega\rangle_R$ characterizes an AFD phase associated with the condensation of the R point of the cubic first Brillouin zone. MD simulations are then conducted following the same steps described in section 2.1 as follows: First the system with a certain Ti composition is equilibrated at a temperature and pressure of interest by running 3×10^5 MD steps of NPT (canonical ensemble) simulations on a $12 \times 12 \times 12$ supercell (8640 atoms). Each time step is 0.5 fs. The output of the MD simulations are the local mode vector components, AFD components and strain tensor components as a function of time. Phase transition temperatures, phase transition sequence, space groups of the phases, average local modes, average AFD vector $\langle\omega\rangle_R$ and average homogeneous strain obtained from simulations were then checked with those obtained by MC simulation for consistency. Barring any discrepancy, the thermostat and barostat are then switched off and the system is equilibrated at constant energy by conducting 10^5 MD steps of NVE (microcanonical ensemble) simulations. Subsequently, 6.8×10^6 NVE steps are performed to obtain time-dependent properties of the structure. Note that MD simulations were also conducted with applied electric field at a desired temperature as described in section 2.1.

Two different complex responses were then computed, in the gigahertz /terahertz regime, from the MD simulations. One of these is the dielectric response and was computed using Eqn.(2.1.4) discussed in section 2.1. Formula for computing the other response is given below [**32**];

$$(2.2.4)\quad \varepsilon_{\alpha\beta}^{AFD}(\nu) - 1 = \frac{1}{\varepsilon_0 V k_B T}\left[\int_0^{t_0} \frac{dt\left\langle \omega_\alpha^R(t)\,\omega_\beta^R(t)\right\rangle}{t_0} + i2\pi\nu\int_0^{\infty} dt e^{i2\pi\nu t}\left\langle \omega_\alpha^R(t)\,\omega_\beta^R(0)\right\rangle\right]$$

where $\omega_{\alpha}^{R}(t)$ is the α component of AFD motions at the R point of the cubic Brillouin zone at time t and other parameters have their usual meaning (see section 2.1). $\varepsilon_{\alpha\beta}^{AFD}(\nu)$ can be thought as the response of $\omega^{R}(t)$ to its alternating–current conjugate field [**32, 49**] and is useful in identifying contributions to the phonon spectrum originating from AFD motions. Each peak in these two responses is fit using classical damped harmonic oscillators of the form $\varepsilon(\nu) = S\nu_r^2/\left(\nu_r^2 - \nu^2 + i\gamma\nu\right)$ where ν_r, γ, and S are the resonant frequency, damping constant and strength of the corresponding mode, respectively.

2.3. Dielectric tunability of ferroelectric materials

In the previous chapter (see section 1.5) Landau-Devonshire phenomenological theory of ferroelectric phase transitions was discussed and a formula for free energy, $\Phi(P,\eta)$, which describes characteristics of uniaxial ferroelectric phase transitions of centro-symmetric bulk systems with spatially uniform polarization was derived. Here we will proceed to derive formulas for dielectric tunability, hereafter denoted by $\tau(E)$, where the electric field is applied parallel to the direction of polarization for such systems.

Considering the three lowest order terms of P in free energy from Eqn. (1.5.4), we have:

$$\Phi(P,\eta) = \frac{1}{2}aP^2 + \frac{1}{4}\beta P^4 - PE \tag{2.3.1}$$

The equation of state, $\frac{\partial\Phi(P,\eta)}{\partial P} = 0$, gives:

$$aP + \beta P^3 = E \tag{2.3.2}$$

and the dielectric constant, $\varepsilon = \frac{1}{\varepsilon_0}\frac{\partial P}{\partial E}$, is:

$$\varepsilon(E) = \frac{1}{\varepsilon_0(a + \beta P^2)}$$

In the paraelectric phase when E=0, and from Eqn.(1.5.5) we have:

$$\varepsilon(0) = \frac{1}{a\varepsilon_0} = \frac{1}{a_0\varepsilon_0(T - T_0)} \tag{2.3.3}$$

Substituting back in $\varepsilon(E)$, for the low-field linear limit (i.e., $P = \varepsilon_0\varepsilon(0)E$) we obtain :

$$\varepsilon(E) = \frac{\varepsilon(0)}{1 + \beta(\varepsilon_0\varepsilon(0))^3 E^2} \tag{2.3.4}$$

Therefore the tunability, $\tau(E) = \frac{\varepsilon(0)}{\varepsilon(E)}$, gives :

$$\tau(E) = 1 + \beta(\varepsilon_0\varepsilon(0))^3 E^2 \tag{2.3.5}$$

In the high-field non-linear limit this approach for obtaining the dielectric constant is no longer practical. Alternatively at these fields Vendik [**50, 51**] has suggested a convenient approach to obtain $\varepsilon(E)$ and $\tau(E)$. Employing that approach yields :

$$\varepsilon(E) = \frac{1}{3\beta^{\frac{1}{3}}E^{\frac{2}{3}}} \tag{2.3.6}$$

$$\tau(E) = 3(\varepsilon_0\varepsilon(0))\beta^{\frac{1}{3}}E^{\frac{2}{3}} \tag{2.3.7}$$

Note that this approach most reliably predicts the tunability at low frequency (i.e., up to GHz) range for temperatures close to transition. Thus these formulas were only used to analyze dielectric tunability at low frequency obtained from MD simulations.

Dielectric tunability from MD simulations for BST systems was found as follows: At a specific temperature close to Curie temperature T_c in the paraelectric phase, the particular system was subjected to a DC electric field of $0.1MV/m$ along an axis the system *tends* to polarize (for example [001] for $BaTiO_3$) below T_c and MD simulations were conducted.

Gradually increasing this field along the axis up to the order of $\sim 10^2 MV/m$ further MD simulations were performed and the complex dielectric response obtained from Eqn.(2.1.4) for each field was fit using suitable DHO's as described previously (see section 2.1). The fitting parameters were then used to obtain tunability at a frequency ν, for each electric field, E using the following formula;

$$\tau(E,\nu) = \frac{\varepsilon(0,\nu)}{\varepsilon(E,\nu)} \tag{2.3.8}$$

Dielectric tunability thus obtained as a function of ν, was thence fitted using Landau-Devonshire theory based phenomenological formulas derived previously and analyzed. Note that the induced polarization was plotted as a function of the applied electric field, and the highest electric field where polarization was linearly proportional to the field E was chosen as the upper limit of low-field fitting.

CHAPTER 3

Disordered $Pb(Zr,Ti)O_3$ Bulk: Results and discussion

In order to investigate the nature and origin of low frequency polar modes of $Pb(Zr,Ti)O_3$ (PZT) near its morphotropic phase boundary (MPB), the approach described in section 2.2 was employed. MD simulations were conducted for preselected Ti compositions, based on the phase diagramm (see[1] Fig. 3.0.1) of PZT of Ref.[**38**] to represent different phase transition sequences with temperature. Simulation parameters used were $N_{NPT} = 3 \times 10^5$, $N_{EQ} = 10^5$ and $N_{NVE} = 6.8 \times 10^6$. Simulations were conducted for temperature in the interval 1100-10 K, starting from 1100 K and descending.

3.1. Temperature evolution of low frequency modes near the MPB

3.1.1. Low frequency modes of $Pb(Zr_{0.55}Ti_{0.45})O_3$. Figure 3.1.1 shows the temperature evolution of the lowest resonant frequencies, ν_r, and the corresponding spectral weights

[1]Source: I. A. Kornev, L. Bellaiche, P.-E. Janolin, B. Dkhil, and E. Suard, Phys. Rev. Lett. 97, 157601 (2006).

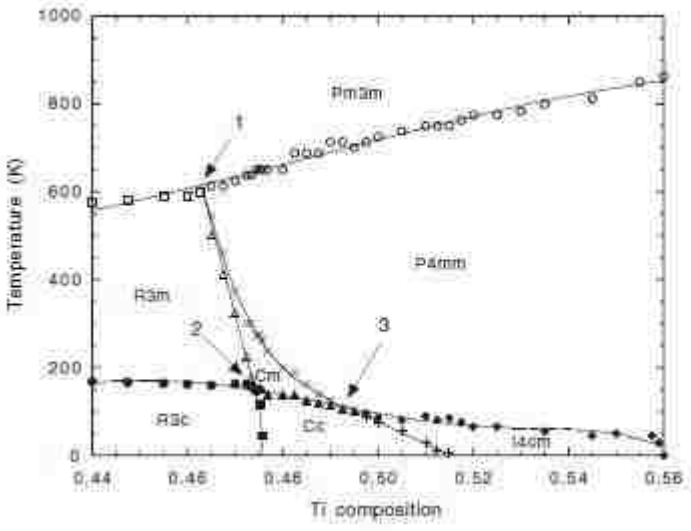

FIGURE 3.0.1. Phase diagram of $Pb(Zr,Ti)O_3$ near its MPB from first-principles effective Hamiltonian approach.

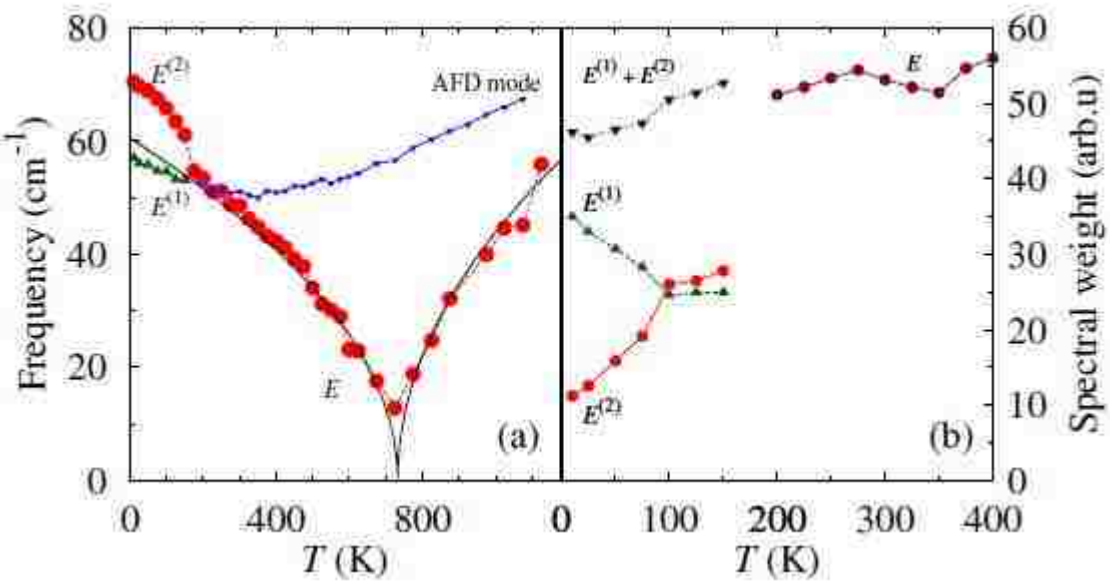

FIGURE 3.1.1. Temperature dependence of some dynamical characteristics in the $Pb(Zr_{0.55}Ti_{0.45})O_3$ solid solution. (a) The ν_r resonant frequency of the lowest-in-frequency dielectric peaks for any temperature as well as the resonant frequency of $\varepsilon_{xx}^{AFD}(\nu)$ for temperatures above 200 K (denoted AFD mode) found in our simulations. The solid lines represent fittings by square-root laws of the resonant frequency of the E(1TO) mode and of the soft mode above T_c. (b) The electric dipole spectral weight of different modes.

[**52**], $S\nu_r^2$, derived through fittings of the frequency peaks of the dielectric responses from simulations of $Pb(Zr_{0.55}Ti_{0.45})O_3$ at various temperatures. Just above the transition Curie temperature T_c, condensation of the lowest optical mode can be seen, which is the signature of a ferroelectric phase transition. Fittings of this mode by the expression $\nu_r = C\,|T - T_c|^{1/2}$ above and below T_c, shows that it behaves in the experimentally observed Curie-Weiss manner with C=2.62 $cm^{-1}K^{1/2}$ for $T > T_c$ and C=2.24 $cm^{-1}K^{1/2}$ for $T < T_c$. Furthermore, below T_c, calculations performed in a basis where the z-axis is parallel to the polarization indicates that this mode corresponds to oscillations in a plane perpendicular to the polarization and it is in fact the well-known E(1TO) mode (hereafter denoted E). Moreover, at room temperature the predicted frequency of the E mode is around 49cm^{-1}, which agrees rather well with the measured value of 60cm^{-1} in a $Pb(Zr_{0.55}Ti_{0.45})O_3$ solid solution [**53**]. All these observations highlight the accuracy of the method of simulation employed.

Further reduction of the temperature results in the appearance of an additional mode in the 50-75 cm^{-1} range below 200K coincident with the R3m to R3c phase transition, which is an anti-ferrodistortive (AFD) phase transition [**32**]. Henceforth, these two modes are denoted $E^{(1)}$ and $E^{(2)}$. Interestingly, through Raman experiments of Refs. [**41**] and [**54**], the existence of two modes exactly within this frequency range and only for temperatures below the R3m-R3c transition was previously reported. B*ä*uerle and Pinczuk [**54**] further observed that the upper mode significantly increases in frequency as the temperature decreases, while the lower mode only very slightly increases in frequency around $58cm^{-1}$, when the system is cooled down. The predictions shown in Figs. 3.1.1 and 3.1.2 are in excellent agreement with all these experimental findings. B*ä*uerle and Pinczuk [**54**] also believed that these two modes have E(TO) symmetry and that the lower mode originates from the zone-boundary AFD mode.

In order to verify these speculations and to better understand the reason behind the existence of the $E^{(1)}$ and $E^{(2)}$ modes, let's check the information provided by our simulations. Computing the complex dielectric responses in a basis in which the new z-axis is parallel to the polarization reveals that $E^{(1)}$ and $E^{(2)}$ indeed have E(TO) symmetry; that is, they both correspond to oscillations of the electric dipoles perpendicularly to the spontaneous polarization. Moreover, the sum of the electric dipole spectral weights of the $E^{(1)}$ and $E^{(2)}$ modes just below 200 K is nearly equal to that of the E mode just above 200 K [see Fig. 3.1.1(b)]. This fact hints at an interaction between the E mode and another dynamical quantity as the reason for the existence of the $E^{(1)}$ and $E^{(2)}$ vibrations. $\varepsilon^{AFD}(\nu)$ for different temperatures displayed in Fig. 3.1.2(c) reveals that the AFD degrees of freedom have two natural frequencies in the 50–75cm^{-1} range, for any temperature below 200 K [**32**] that exactly coincide with the frequencies of the $E^{(1)}$ and $E^{(2)}$ modes proving that, this dynamical quantity is in fact the AFD distortions. On the other hand, only a single frequency around 50 cm^{-1} can be found for the AFD dynamics above 200 K, as indicated by Fig(s). 3.1.1(a) and 3.1.2(c). These results imply that, in the R3c phase, the fluctuations of the AFD degrees of freedom become coupled with the transverse fluctuations of the FE degrees of freedom.

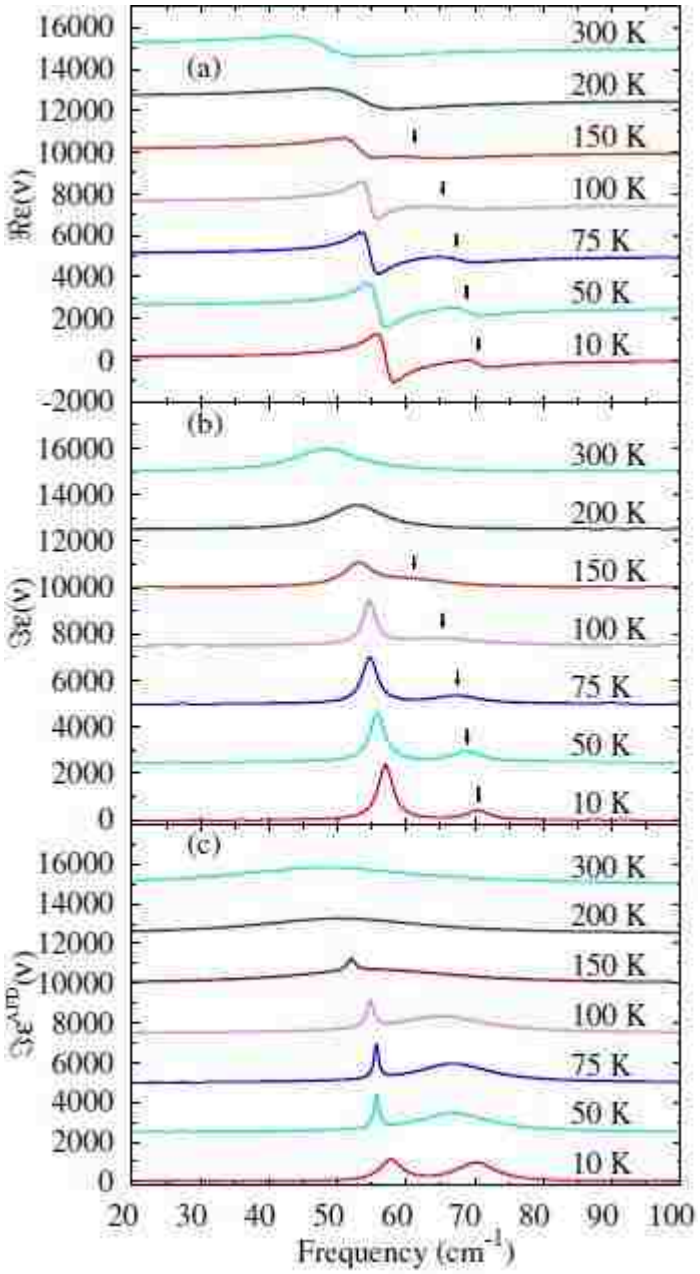

FIGURE 3.1.2. Complex responses of the $Pb(Zr_{0.55}Ti_{0.45})O_3$ solid solution in the 20–100 cm^{-1} frequency range at different temperatures. The (a) real and (b) imaginary parts of the $\varepsilon_{xx}(\nu)$ dielectric response. (c) The imaginary part of the AFD-related $\varepsilon_{xx}^{AFD}(\nu)$ function. The displayed data correspond to a fit of the raw data by classical damped harmonic oscillators. The data for 50, 75, 100, 150, 200, and 300 K have been vertically shifted by 2500, 5000, 7500, 10 000, 12 500, and 15 000, respectively, in order to distinguish them from the 10 K data.

The AFD mode acquires some polarity due to this coupling, which explains why it can now be seen in the dielectric spectra (as the $E^{(1)}$ mode) below 200 K, while the "usual" E dielectric mode loses some polar character due to that coupling, which explains why the electric dipole spectral weight of $E^{(2)}$ decreases below 200 K [**32**] [see Fig. 3.1.1(b)]. In other words, $E^{(1)}$ originates from the AFD motions (as correctly guessed by Bäuerle and Pinczuk [**54**]) once these motions are allowed to dynamically couple with the FE distortions[2], that is, once the AFD and FE degrees of freedoms both adopt a long-range order [**55, 56**]. $E^{(2)}$ is the remaining signature of the original E mode. Numerical computations further reveal that $E^{(1)}$ and $E^{(2)}$ modes both mostly originate from the coupling between the E polar mode and the oscillations of the AFD motions perpendicular to the polarization's direction. More insight into this coupling is provided in section 3.4.

3.1.2. Low frequency modes of $Pb(Zr_{0.52}Ti_{0.48})O_3$. Figure 3.1.3 displays the temperature evolution of the lowest resonant frequencies, ν_r, and the corresponding spectral weights, $S\nu_r^2$, from simulations of $Pb(Zr_{0.52}Ti_{0.48})O_3$ at various temperatures. Just as in Ti 45%, one can witness the condensation of the lowest optical mode above the Curie temperature T_c as the temperature is decreased, and the appearence of the E(1TO) mode below T_c. Intriguingly, upon further reduction of the temperature, the doubly degenerate E(1TO) mode slightly softens just above 200 K and splits into two modes below 200K coincident with the tetragonal (P4mm) to monoclinic (Cm) ferroelectric phase transition. Thus the lowering of the ferroelectric symmetry results in the lifting of the degeneracy of the E(1TO) mode. Calculations of dielectric tensor components done in a basis where the z-axis is aligned with the polarization reveal that these two modes also represent dipole oscillations perpendicular to the direction of polarization, and that the lower of the two has A' symmetry and the other has A'' symmetry [**57**] in line with group theory predictions. Further cooling of the system results in the appearance of a second pair of modes below 130 K coinciding with the Cm to Cc (monoclinic) AFD phase transition. These modes originate from the coupling between AFD motions and ferroelectric motions [**57**]. The origin and splitting of these modes will

[2]Only a single peak with E symmetry is found if one sets to zero the $D_{\alpha\beta\gamma\delta}$ matrix elements of Eqn.(2.2.3).

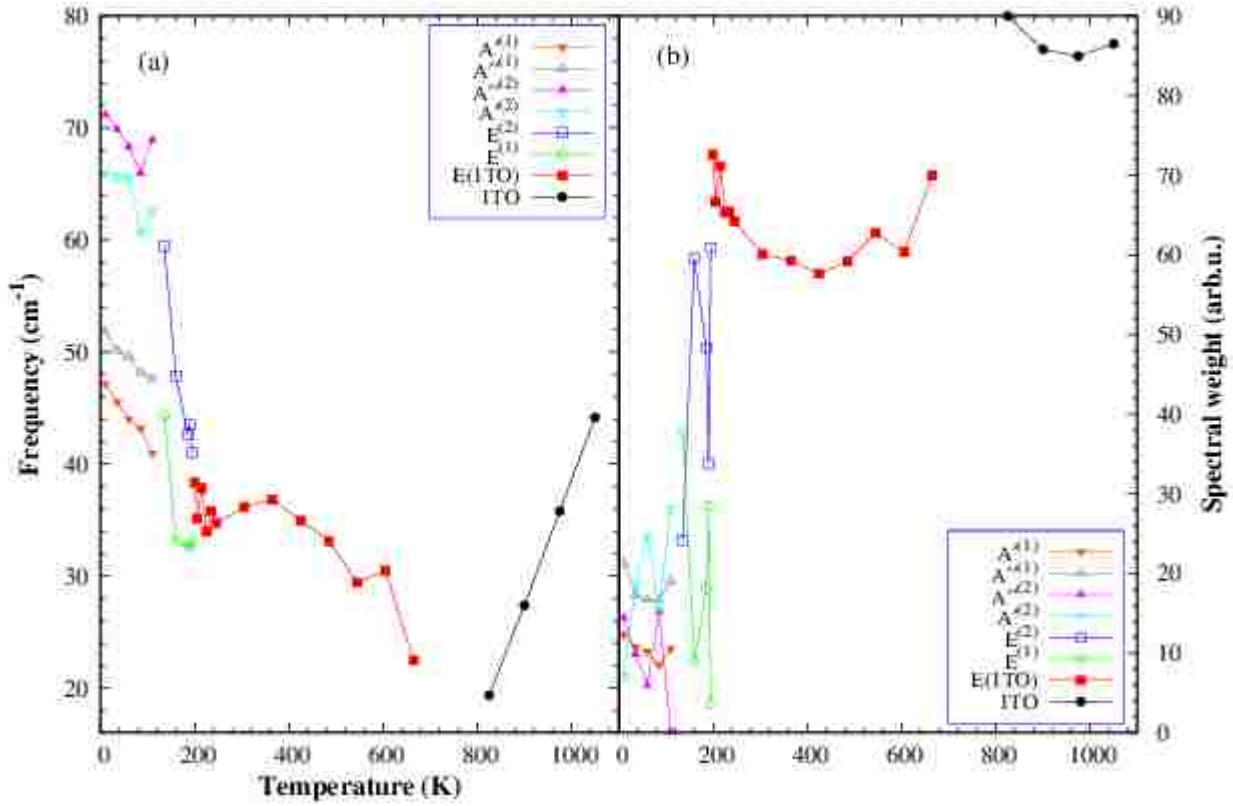

FIGURE 3.1.3. Temperature dependence of some dynamical characteristics in the $Pb(Zr_{0.52}Ti_{0.48})O_3$ solid solution. (a) The ν_r resonant frequencies of the lowest-in-frequency dielectric peaks for any temperature. (b) The electric dipole spectral weight of the corresponding low frequency modes.

be discussed in detail in sections 3.3 and 3.4. All these modes increase in frequency with decreasing temperature, as similar to the behavior seen in the R3c of $Pb(Zr_{0.55}Ti_{0.45})O_3$ phase previously.

3.1.3. Low frequency modes of $Pb(Zr_{0.48}Ti_{0.52})O_3$. Figure 3.1.4 displays the temperature evolution of the lowest resonant frequencies, ν_r, and the corresponding spectral weights $S\nu_r^2$, from simulations of $Pb(Zr_{0.48}Ti_{0.52})O_3$ at various temperatures. Similar to PZT with Ti 45% and 48%, one can witness the condensation of the lowest optical mode above the curie temperature T_c, as the temperature is decresed and the appearence of the E(1TO) mode below T_c. Upon further reduction of the temperature an additional peak appears below 130K in the vicinity of the tetragonal, P4mm to I4cm (still tetragonal) AFD

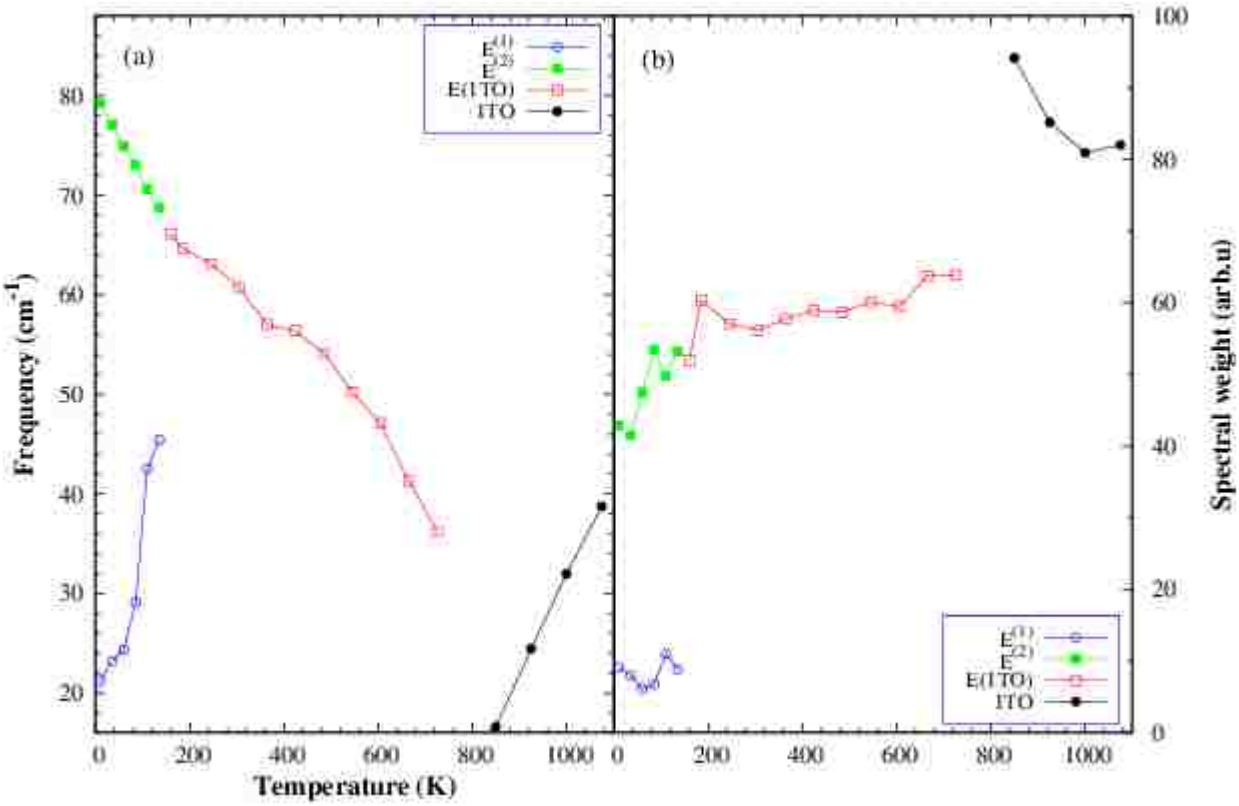

FIGURE 3.1.4. Temperature dependence of some dynamical characteristics in the $Pb(Zr_{0.48}Ti_{0.52})O_3$ solid solution. (a) The ν_r resonant frequencies of the lowest-in-frequency dielectric peaks for any temperature. (b) The electric dipole spectral weight of the corresponding low frequency modes.

phase transition. These two modes are in fact similar to the $E^{(1)}$ and $E^{(2)}$ modes found in R3c phase for PZT with Ti 45% except that $E^{(1)}$ softens with decreasing temperature rather than hardening. Moreover the appearance of these modes in the I4cm phase have been confirmed by recent various spectroscopic measurements [**41, 44, 48**]. Also coupling between the modes are lessor than in R3c as indicated by the reversal of the spectral weight magnitudes signifying lower polarity of the $E^{(1)}$ mode in the I4cm phase.

3.2. Effect of direct-current(DC) field

Let's now use our scheme to simulate the effect of a direct-current electric field applied along the polarization direction, on the $E^{(1)}$ and $E^{(2)}$ modes of disordered $Pb(Zr_{0.55}Ti_{0.45})O_3$.

Figures 3.2.1(a) and 3.2.1(b) show the resonant frequencies and the relative square of the oscillator strengths of these two modes extracted from the dielectric responses for DC electric fields of different magnitudes at 10 K. Figure 3.2.1 reveals a text book example of a so-called anticrossing [**58**]: the $E^{(1)}$ and $E^{(2)}$ modes exchange their character as the field increases (i.e., the $E^{(1)}$ mode becomes less polar, while the $E^{(2)}$ mode gains significant polarity), while their frequencies never cross. To gain further insight into these results, coupled dynamical equations of FE and AFD distortions within the harmonic approximation were constructed where the 2×2 dynamical matrix D(E), of these equations is given by Eqn. (3.2.1).

$$D(E) = \begin{bmatrix} (\nu_u^{(0)})^2 + fE & \kappa \\ \kappa & (\nu_\omega^{(0)})^2 + aE \end{bmatrix} \tag{3.2.1}$$

In this matrix, the two diagonal terms are assumed to be linear functions of the magnitude of electric field and the off diagonal terms represent coupling between distortions and are considered to be independent of electric field. Resonant frequencies and the relative square of the oscillator strengths of the two modes from MD simulations were fitted by means of eigenvalues and eigenvectors of this matrix. The fittings confirms the assumptions incorporated in the dynamical matrix. The dashed lines in Fig. 3.2.1(a) are the uncoupled resonant frequencies (i.e., diagonal terms of Eqn. (3.2.1)). The author is not aware of any previously reported field-induced dynamical anticrossing involving FE and AFD degrees of freedom. Note, however, that such anticrossings can be expected on symmetry grounds since $E^{(1)}$ and $E^{(2)}$ have the same symmetry, namely, they are both E(TO) modes.

3.3. Composition evolution near MPB of low-frequency coupled modes

MD simulations are carried out for *disordered* PZT solid solutions, with Ti compositions ranging from 45.2% to 56.0% in intervals of 0.2% and for a temperature of 10 K. Simulation parameters used were $N_{NPT} = 3 \times 10^5$, $N_{EQ} = 10^5$ and $N_{NVE} = 6.8 \times 10^6$. Figure 3.3.1(a) provides the magnitude of the local mode vector ($|\langle \boldsymbol{u} \rangle|$) and its Cartesian components ($\langle u_x \rangle$, $\langle u_y \rangle$, and $\langle u_z \rangle$) –averaged over the MD steps and the supercell sites – as a function of

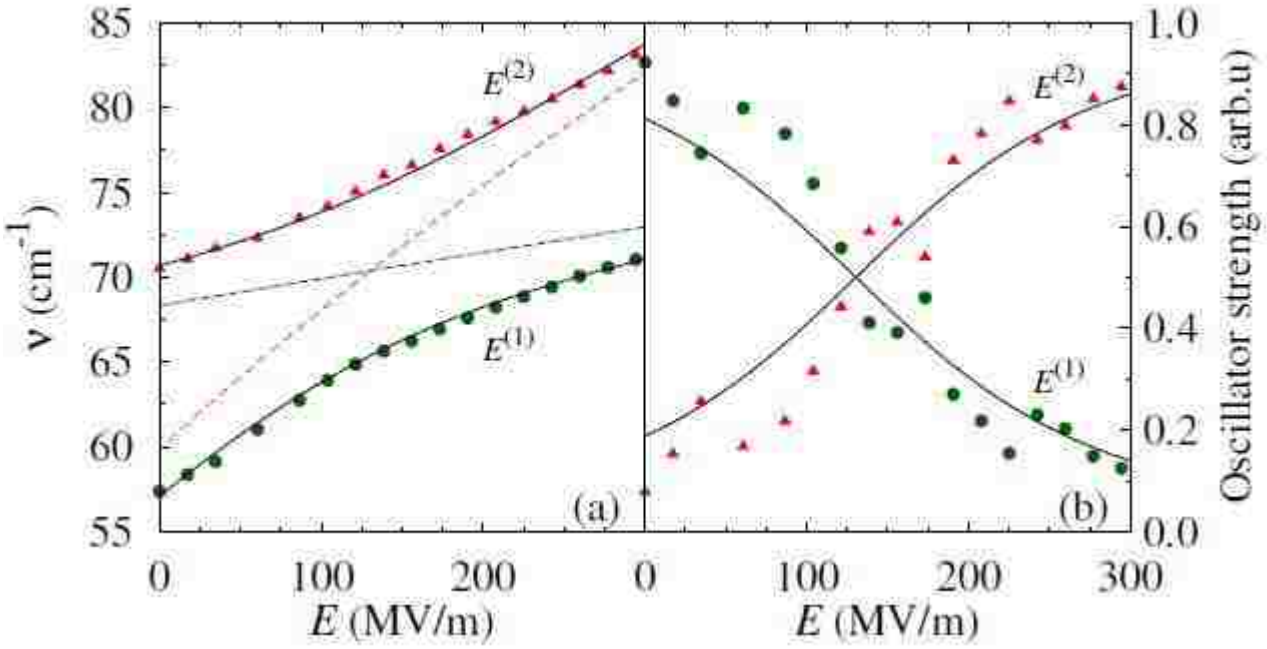

FIGURE 3.2.1. (a) Resonant frequency and (b) relative square of the strength of the oscillator of the $E^{(1)}$ and $E^{(2)}$ modes . Solid lines in (a) and (b) represent fittings by the eigenvalues and eigenvectors of a 2 × 2 matrix, respectively. Dashed lines in (a) are frequencies that linearly depend (off diagonal terms of 2 × 2 matrix) on the magnitude of the electric field.

composition in disordered PZT solid solutions. Note that the x-, y- and z-axes are chosen along the pseudo-cubic [100], [010] and [001] directions, respectively. Figure 3.3.1(b) provides similar information, but for the magnitude of the antiphase AFD vector ($|\langle \boldsymbol{\omega}_R \rangle|$) and its Cartesian components ($\left\langle \omega_{x,R} \right\rangle$, $\left\langle \omega_{y,R} \right\rangle$, and $\left\langle \omega_{z,R} \right\rangle$). For compositions in the 45.2%-47.5% range, all components found for both local mode and AFD motions were non-zero with $\langle u_x \rangle = \langle u_y \rangle = \langle u_z \rangle$ and $\left\langle \omega_{x,R} \right\rangle = \left\langle \omega_{y,R} \right\rangle = \left\langle \omega_{z,R} \right\rangle$. This is indicative of the rhombohedral $R3c$ phase, as consistent with the measurements of Refs.[**54, 41, 42**]. Within the 47.5%-51.0% range, all components found for both local mode and AFD motions were similarly non-zero, but in this case $\langle u_z \rangle$ was larger than $\langle u_x \rangle$ and $\langle u_x \rangle = \langle u_y \rangle$, while $\left\langle \omega_{z,R} \right\rangle$ was larger than $\left\langle \omega_{x,R} \right\rangle$ and $\left\langle \omega_{x,R} \right\rangle = \left\langle \omega_{y,R} \right\rangle$. Such equalities and inequalities are consistent with a monoclinic Cc phase. Furthermore, since the ratio $\langle u_z \rangle / \langle u_x \rangle$ is different from $\left\langle \omega_{z,R} \right\rangle / \left\langle \omega_{x,R} \right\rangle$, the axis of rotation of the oxygen octahedra does not coincide with the direction of polarization in this Cc state. Finally, for compositions varying between 51.0% and 56.0%, $\langle u_z \rangle$ and $\left\langle \omega_{z,R} \right\rangle$ were the

only non-zero components found for the local mode vector and AFD motions, respectively, indicating the occurrence of a tetragonal $I4cm$ phase. It is also interesting to realize that Figs. 3.3.1(a) and 3.3.1(b) reveal that the *magnitudes* of both the local mode vector and the antiphase AFD vector are nearly constant within the compositional range defining the Cc state. Thus, we can conclude that both polarization and AFD vectors are "simply" rotating from the [111] to the [001] pseudo-cubic direction as the overall Ti concentration increases within the Cc phase.

Furthermore, Figures 3.3.1(c) and (d) display the composition dependence of the resonant frequencies, ν_r, and the corresponding spectral weights $S\nu_r^2$, of low-frequency modes (i.e., below 100 cm^{-1}), obtained through fittings of the frequency peaks of the dielectric responses for the same temperature of 10 K. As previously indicated, the existence of two (double degenerate) E(TO) modes – denoted by $E^{(1)}$ and $E^{(2)}$ – in the $R3c$ state, are found as consistent with experiments [**41, 45, 48**] conducted at low temperature. The origin of these two modes was revealed to be the coupling between the AFD and FE degrees of freedom and will be discussed in more detail in section 3.4 [**32**]. As the Ti composition increases from 45%, both $E^{(1)}$ and $E^{(2)}$ modes' frequencies slightly decrease (in agreement with the measurements of Ref.[**48**]) and then undergo a clear splitting starting from 47.6%. This splitting is exactly coincident with the advent of the Cc phase for PZT at 10 K, as evidenced from Figs. 3.3.1(a) and 3.3.1(b). Each E mode splits into $A' + A''$ modes. Let's denote the two modes resulting from the splitting of $E^{(1)}$ as $A'^{(1)}$ and $A''^{(1)}$. Similarly, the two modes originating from $E^{(2)}$ are denoted by $A'^{(2)}$ and $A''^{(2)}$. We numerically find that the $A'^{(1)}$, $A''^{(1)}$, $A'^{(2)}$ and $A''^{(2)}$ peaks observed in the dielectric response have corresponding peaks (with identical resonant frequencies) in the $\varepsilon_{\alpha\beta}^{\text{AFD}}(\nu)$ AFD response. This proves that these four modes all possess both FE and AFD characters, thanks to the couplings between these two different structural degrees of freedom [**57**]. Moreover, computing the tensor components of $\varepsilon_{\alpha\beta}(\nu)$ and $\varepsilon_{\alpha\beta}^{\text{AFD}}(\nu)$ in a new basis where the z-axis is along the polarization reveals that all these modes correspond to electric dipole oscillations being perpendicular to the direction of polarization in the Cc phase. Furthermore, Fig. 3.3.1(c) indicates that

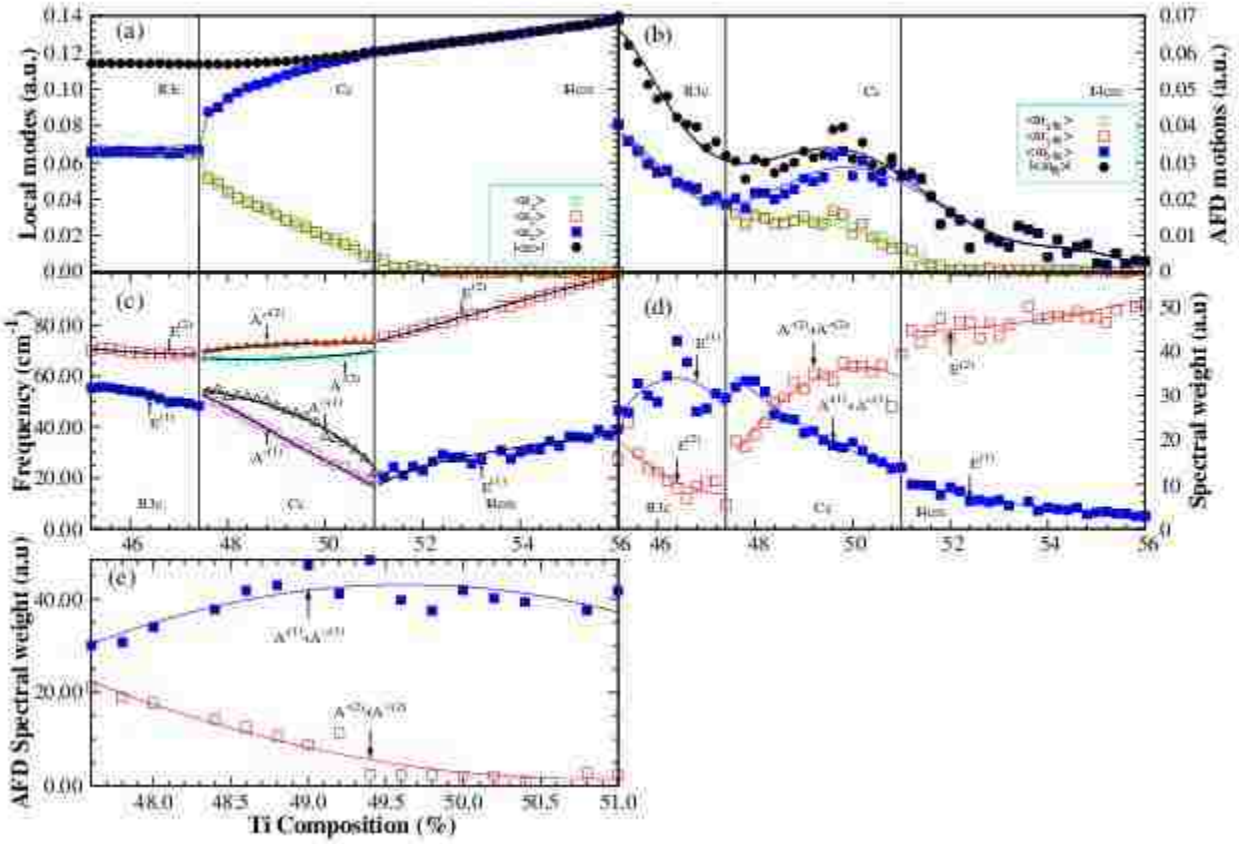

FIGURE 3.3.1. Predicted compositional dependency of some physical properties in disordered PZT at 10 K. Panel (a) shows the magnitude and Cartesian components of the local mode. Panel (b) displays the same information than Panel (a), but for the AFD vector. Panel (c) provides the resonant frequency of the lowest optical phonon modes seen in the dielectric spectra. Panel (d) gives the spectral weight of the $E^{(1)}$ and $E^{(2)}$ modes in the R3c and I4cm states, as well as, the sum of the spectral weights of the $A'^{(1)}$ and $A''^{(1)}$ modes and the sum of the spectral weights of the $A'^{(2)}$ and $A''^{(2)}$ modes for the *dielectric spectra* of the Cc phase. Panel (e) is similar to Panel (d) but only for the Cc state and for the $\varepsilon^{\rm AFD}_{\alpha\beta}(\nu)$ *AFD* response. The solid lines in Panel (c) provides the fitting of the resonant frequencies by Eqs. (3.4.5) in the $R3c$ and $I4cm$ states and by Eqs. (3.4.6) in the Cc phase.

the frequency difference between the $A'^{(1)}$ and $A''^{(1)}$ (and also between $A'^{(2)}$ and $A''^{(2)}$) is relatively small in the Cc state. For instance, these differences are typically smaller than the frequency difference between $E^{(1)}$ and $E^{(2)}$ in the $R3c$ phase. Figure 3.3.1(c) further shows that these frequency differences between the A' and A'' modes originating from $E^{(1)}$ and $E^{(2)}$, to be denoted by $\Delta\nu(E^{(1)})$ and $\Delta\nu(E^{(2)})$, respectively, are largest near the compositional

mid-point of the Cc phase (that is located around a Ti composition of 49.4 %) and decrease to either side of it. To better understand and quantify this point, let's introduce a parameter quantifying how far away is a Cc state with respect to its delimiting $R3c$ and $I4cm$ "borders". Here, this parameter is denoted by m_{dep}, is termed the "monoclinic depth", and is defined by [**57**]:

$$m_{\mathrm{dep}} = \frac{\left(\hat{\boldsymbol{P}}.\hat{\boldsymbol{m}}\right)\left(\hat{\boldsymbol{\omega}}.\hat{\boldsymbol{m}}\right)}{\left(\hat{\boldsymbol{P}}.\hat{\boldsymbol{\omega}}\right)} - \cos^2\theta_m \tag{3.3.1}$$

where $\hat{m}$ is the unit vector along the direction that equally divides the [001] and [111] pseudo-cubic directions. As a result, $\hat{\boldsymbol{m}} = \frac{\hat{\boldsymbol{i}}+\hat{\boldsymbol{j}}+\left(1+\sqrt{3}\right)\hat{\boldsymbol{k}}}{\sqrt{2\sqrt{3}\left(1+\sqrt{3}\right)}}$, with $\hat{\boldsymbol{i}}$, $\hat{\boldsymbol{j}}$ and $\hat{\boldsymbol{k}}$ being the unit vectors along the pseudo-cubic [100], [010] and [001] directions, respectively. In Eq.(3.3.1), $\hat{\boldsymbol{P}}$ and $\hat{\boldsymbol{\omega}}$ are the unit vectors along the direction of polarization and along the axis about which the long-range-ordered oxygen octahedra tilt, respectively. θ_m is the polar angle of $\hat{\boldsymbol{m}}$, therefore yielding $\cos^2\theta_m = \frac{1+\sqrt{3}}{2\sqrt{3}}$. Note that Eq.(3.3.1) ensures that m_{dep} is zero in the $R3c$ and $I4cm$ phases and equal to $\frac{\sqrt{3}-1}{2\sqrt{3}}$ if $\hat{\boldsymbol{P}}$ and $\hat{\boldsymbol{\omega}}$ both lie along $\hat{\boldsymbol{m}}$. Figure 3.3.2 displays $\Delta\nu(E^{(1)})$ and $\Delta\nu(E^{(2)})$ *versus* m_{dep} within the Cc compositional region and at 10 K, as well as their fittings by polynomials of first or second order. One can indeed see that $\Delta\nu(E^{(1)})$ and $\Delta\nu(E^{(2)})$ can be reasonably well fitted by these polynomials. Interestingly, these polynomials are monotonically increasing functions of the "monoclinic depth", which therefore quantitatively confirms that the closer the Cc state is from its mid-point (between the $R3c$ and $I4cm$ phases), the larger are the frequency splittings. In Fig. 3.3.1(d), the sum of the spectral weights of $A'^{(1)}$ and $A''^{(1)}$, and the sum of of the spectral weights of $A'^{(2)}$ and $A''^{(2)}$, are plotted in the Cc phase (along with the spectral weight of the $E^{(1)}$ and $E^{(2)}$ modes in the $R3c$ and $I4cm$ phases), as a function of composition. Such figure reveals that, at the rhombohedral "border" of this monoclinic phase, the strength of the $E^{(1)}$ mode is larger than that of the $E^{(2)}$ mode, while the $E^{(2)}$ becomes much more polar with respect to $E^{(1)}$ at the "tetragonal" compositional border of the Cc phase. This change in polarity occurs via the gain in the sum of the spectral weights of $A'^{(2)}$ and $A''^{(2)}$ at the expense of

the sum of the spectral weights of $A'^{(1)}$ and $A''^{(1)}$, when the Ti composition increases within the Cc state. Figure 3.3.1(e) further shows that, conversely, the modes derived from $E^{(2)}$ (i.e., $A'^{(2)}$ and $A''^{(2)}$) lose more and more their AFD character during that compositional increase, while the modes that are originating from $E^{(1)}$ strengthen their AFD character. Such features are indicative of a compositionally-induced *anticrossing* (between the "bare" FE and AFD modes) occurring within the Cc phase. Note that an anticrossing between the $E^{(1)}$ and $E^{(2)}$ modes were previously predicted for a specific composition in the $R3c$ state of PZT and discussed in section 3.2.1, but it was generated by an electric field [**32**]– which contrasts with the presently discussed one which is induced by the composition in the Cc phase of PZT [**57**].

Figure 3.3.1(c) further indicates that the splittings of both the $E^{(1)}$ and $E^{(2)}$ modes into $A' + A''$ modes start to disappear for a composition around 51%, which is coincidentally in the vicinity of the Cc to $I4cm$ phase transition at 10K [see Figs. 3.3.1(a) and 3.3.1(b)]. As a result, in the $I4cm$ phase and as consistent with symmetry, *doubly-degenerated* $E^{(1)}$ and $E^{(2)}$ modes are again observed – exactly as in the (Ti-poorer) $R3c$ phase and in agreement with recent spectroscopic observations [**41, 44, 48**]. Thus the symmetry of these modes for all low temperature phases across the MPB are consistent with predictions from group theory. Nevertheless, the frequency difference between these two modes is larger in the $I4cm$ phase than in the $R3c$ phase, and further increases when increasing the Ti composition within the $I4cm$ state (as also seen in the measurements of Ref.[**48**]). Furthermore, the spectral weight of $E^{(2)}$ in the dielectric spectra increases while the spectral weight of $E^{(1)}$ significantly reduces until almost vanishing when the Ti concentration increases in the $I4cm$ phase [see Fig. 3.3.1(d)].

3.4. Analytical models for coupled modes

To understand features found in previous sections via the use and analysis of our atomistic effective Hamiltonian technique, let's develop analytical models for structural phases (such as $R3c$, $I4cm$ and Cc) that exhibit both long-range ordered FE and AFD motions. In such

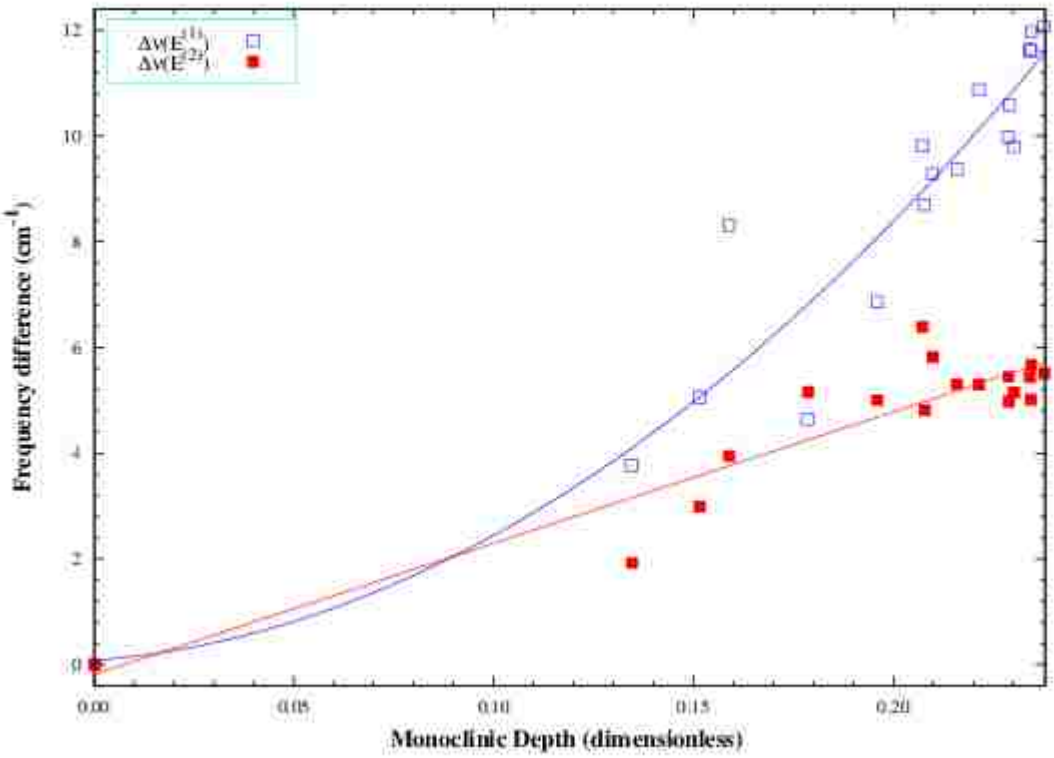

FIGURE 3.3.2. Difference in frequency between the A′ and A″ modes derived from the $E^{(1)}$ (in blue) and $E^{(2)}$ (in red) modes, as a function of the monoclinic depth (see text). The solid lines represent fit of these data by linear and quadratic functions in case of $\Delta\nu(E^{(2)})$ and $\Delta\nu(E^{(1)})$, respectively.

cases, these motions at site i can be represented as:

$$\begin{cases} \mathbf{u_i}(\mathbf{t}) = \langle \mathbf{u} \rangle + \tilde{\mathbf{u}}_\mathbf{i}(\mathbf{t}) \\ \boldsymbol{\omega}_\mathbf{i}(\mathbf{t}) = \langle \boldsymbol{\omega}_\mathbf{R} \rangle + \tilde{\boldsymbol{\omega}}_\mathbf{i}(\mathbf{t}) \end{cases} \tag{3.4.1}$$

where t represents time, $\langle \mathbf{u} \rangle$ and $\langle \boldsymbol{\omega}_\mathbf{R} \rangle$ are the equilibrium, spontaneous values of the FE and AFD motions, respectively. Finally, $\tilde{\mathbf{u}}_\mathbf{i}$ and $\tilde{\boldsymbol{\omega}}_\mathbf{i}$ are the deviations of the FE motions and AFD motions at site i, respectively, from their equilibrium values. It can be then shown (see appendix A), by plugging Eq.(3.4.1) into Eq.(2.2.3), that the essential FE-AFD *linear*

coupling energetic term that influences the dynamics of $\tilde{\mathbf{u}}_\mathbf{i}$ and $\tilde{\boldsymbol{\omega}}_\mathbf{i}$ has the following form:

$$H_{\text{FE-AFD}} \simeq \sum_i \kappa \left|\langle \boldsymbol{u} \rangle\right| \left|\langle \boldsymbol{\omega_R} \rangle\right| \tilde{\mathbf{u}}_\mathbf{i} \cdot \tilde{\boldsymbol{\omega}}_\mathbf{i}, \tag{3.4.2}$$

where the "| |" symbol represents the magnitude of a vector, and where κ is a coupling coefficient involving the $\mathrm{D}_{\alpha\beta\gamma\delta}$ parameters of Eq.(2.2.3). Note that the precise combination of the $\mathrm{D}_{\alpha\beta\gamma\delta}$ coefficients yielding the κ parameter is different between the $R3c$, Cc and $I4cm$ states since it depends on the direction of the polarization.

3.4.1. In case of the R3c and I4cm states. Equation (3.4.2) implies that, for the doubly-degenerate E modes of the $R3c$ and $I4cm$ states, the dynamical *coupled* equations for $\tilde{\mathbf{u}}_\mathbf{i}$ and $\tilde{\boldsymbol{\omega}}_\mathbf{i}$ are given within the harmonic approximation by:

$$\begin{cases} \frac{d^2\tilde{\mathbf{u}}_\mathbf{i}}{dt^2} + 4\pi^2\nu_u^2\tilde{\mathbf{u}}_\mathbf{i} + \frac{\kappa\left|\langle \boldsymbol{u} \rangle\right|}{m_u}\left|\langle \boldsymbol{\omega_R} \rangle\right| \tilde{\boldsymbol{\omega}}_\mathbf{i} = & \frac{Z^*\mathbf{E(t)}}{m_u} \\ \frac{d^2\tilde{\boldsymbol{\omega}}_\mathbf{i}}{dt^2} + 4\pi^2\nu_\omega^2\tilde{\boldsymbol{\omega}}_\mathbf{i} + \frac{\kappa\left|\langle \boldsymbol{u} \rangle\right|}{m_\omega}\left|\langle \boldsymbol{\omega_R} \rangle\right| \tilde{\mathbf{u}}_\mathbf{i} = & 0 \end{cases} \tag{3.4.3}$$

where ν_u and ν_ω are natural frequencies of the "bare" FE soft mode and "bare" AFD mode respectively. m_u, m_ω are the effective masses of the "bare" FE mode and the "bare" AFD mode, respectively. Z^* is the Born effective charge associated with the FE soft mode and $\boldsymbol{E}(t)$ is an applied ac electric field.

One important information resulting from Eq. (3.4.3) is that the dynamical coupling between the FE and AFD motions is reduced (respectively, vanishes) as the $\left|\langle \boldsymbol{\omega_R} \rangle\right|$ magnitude of the spontaneous AFD motion decreases (respectively, is annihilated). This explains why the spectral weight of the $E^{(1)}$ mode diminishes in the dielectric spectra as the Ti composition increases in the $I4cm$ state (see Fig. 3.3.1(d)). In other words, the $E^{(1)}$ mode does not have significant polarity anymore for large compositions in the $I4cm$ state (and thus can not be easily seen in the dielectric spectra) because the dynamical coupling between FE and AFD motions is rather small there as a result of small $\left|\langle \boldsymbol{\omega_R} \rangle\right|$.

Moreover, let's assume that, within the $R3c$ or $I4cm$ phase, the compositional dependencies of the natural frequencies of the "bare" FE and AFD modes are given by:

$$\text{(3.4.4)} \qquad \begin{cases} \nu_u^2 = & (\nu_u^{(0)})^2 + fx \\ \nu_\omega^2 = & (\nu_\omega^{(0)})^2 + ax \end{cases}$$

where x is the Ti composition, and where $\nu_u^{(0)}$, f, $\nu_\omega^{(0)}$ and a are composition-independent parameters within the $R3c$ or $I4cm$ phase.

For small magnitude of the *ac* electric field, one can prove that combining Eqs. (3.4.3) and (3.4.4) provides two resonant frequencies (whose associated peaks should be seen in both the dielectric and AFD responses and that both correspond to doubly-degenerate E modes) that are given by:

$$\text{(3.4.5)} \qquad \begin{cases} (\nu_1)^2 = & \frac{(\nu_u^{(0)})^2+(\nu_\omega^{(0)})^2}{2} + \left(\frac{a+f}{2}\right)x - \sqrt{\left(\frac{(\nu_u^{(0)})^2-(\nu_\omega^{(0)})^2}{2} + \frac{(f-a)x}{2}\right)^2 + \frac{(\kappa|\langle \boldsymbol{u}\rangle||\langle \boldsymbol{\omega_R}\rangle|)^2}{16\pi^4 m_u m_\omega}} \\ (\nu_2)^2 = & \frac{(\nu_u^{(0)})^2+(\nu_\omega^{(0)})^2}{2} + \left(\frac{a+f}{2}\right)x + \sqrt{\left(\frac{(\nu_u^{(0)})^2-(\nu_\omega^{(0)})^2}{2} + \frac{(f-a)x}{2}\right)^2 + \frac{(\kappa|\langle \boldsymbol{u}\rangle||\langle \boldsymbol{\omega_R}\rangle|)^2}{16\pi^4 m_u m_\omega}} \end{cases}$$

Interestingly and as shown by Fig. 3.3.1(c), Equations (3.4.5) can fit very well the resonant frequency of the $E^{(1)}$ and $E^{(2)}$ modes for all the investigated compositions in the $R3c$ and $I4cm$ phases – which validates the relevance of this analytical model based on the coupling between FE and AFD degrees of freedom. Note that, as expected, a different set of parameters (κ, $\nu_u^{(0)}$, f, $\nu_\omega^{(0)}$, a) has to be used to fit the data of the $R3c$ *versus* $I4cm$ states.

3.4.2. In case of the Cc state. In the Cc state, the degeneracy of both $E^{(1)}$ and $E^{(2)}$ modes has been lifted, giving $A'^{(1)}$ and $A''^{(1)}$ from $E^{(1)}$ and $A'^{(2)}$ and $A''^{(2)}$ from $E^{(2)}$, as discussed previously. As indicated by our MD data (see Fig. 3.3.2), this lifting is related to the monoclinic depth introduced earlier. As inferred from Fig. 3.3.2, we can thus assume

that the frequencies of the $A'^{(1)}$, $A''^{(1)}$, $A'^{(2)}$ and $A''^{(2)}$ modes are given, respectively, by:

$$\begin{cases} \nu_1' = & \nu_1 + f_1\left(m_{dep}\right) \\ \nu_1'' = & \nu_1 - f_1\left(m_{dep}\right) \\ \nu_2' = & \nu_2 + f_2\left(m_{dep}\right) \\ \nu_2'' = & \nu_2 - f_2\left(m_{dep}\right) \end{cases} \tag{3.4.6}$$

where ν_1 and ν_2 are given by Eqn.(3.4.5) – and are thus solutions of the *coupled* Eqns(3.4.3) – and where f_1 and f_2 are second-order and first-order polynomials respectively, of m_{dep}. As can be seen in Fig. 3.3.1(c), these equations fit nicely the resonant frequencies of all $A'^{(1)}$, $A''^{(1)}$, $A'^{(2)}$ and $A''^{(2)}$ modes in the Cc phase for a given set of parameters (κ, $\nu_u^{(0)}$,f, $\nu_\omega^{(0)}$, a) and for given f_1 and f_2 functionals (note that the m_{dep} value used is obtained from the MD data for each Ti composition ranging within the Cc state). Such good fits further confirm the validity of our analytical models, in general, and the role of the coupling between FE and AFD motions on characteristics of low-optical phonon modes, in particular.

3.5. Non-linear dynamical coupling near MPB

So far nature and origin of dynamical phenomena related to low frequency modes at low temperature, in phases possessing *both* long-range ordered FE and AFD motions near MPB have been discussed. Close inspection of dielectric responses at higher temperature, i.e., in *purely* FE phases near MPB leads to the uncovering of an intriguing phenomenon too. Figures 3.5.1(a) and 3.5.1(b) display the real and imaginary parts of the isotropic dielectric response – i.e., $[\varepsilon_{xx}(\nu)+\varepsilon_{yy}(\nu)+\varepsilon_{zz}(\nu)]/3$ – of a $Pb(Zr_{0.47}Ti_{0.53})O_3$ system versus frequency at 600 K and 400 K, respectively. The insets of these figures show the $\varepsilon_{zz}(\nu)$ dielectric response, where z is along the direction of polarization. Figure 3.5.1(a) indicates that $Pb(Zr_{0.47}Ti_{0.53})O_3$ behaves "normally" at 600 K, i.e. it possesses a doubly-degenerate E mode at lower frequencies and a single A_1 mode at higher frequencies. Note that the A_1 mode corresponds to atomic vibrations parallel to the direction of the spontaneous polarization. One important feature revealed by Fig. 3.5.1(b) is the "abnormal" existence of two

A_1 modes at 400 K [**59**]. These two modes are denoted as $A_1^{(1)}$ and $A_1^{(2)}$ hereafter and their resonant frequencies are around 136 and 161 cm^{-1}, respectively, at 400 K. It is important to realize that the crystallographic phase is identical between 400K and 600K (i.e., P4mm). In other words, the doubling of the A_1 modes is not associated with a phase transition, unlike the extra E mode that occurs at low temperature [**32, 55**]. Further simulations for PZT systems with different compositions near the morphotropic phase boundary (MPB), as well as using different supercell sizes, were also performed at 300 K and 400 K, and two A_1 modes were also found in these systems. This doubling of the A_1 mode thus appears to be a general feature of PZT systems near their MPB. Moreover, to uncover the origin of this phenomena, additional simulations were conducted in which alloying effects are switched off in PZT. This was achieved by treating the studied solid solution as a simple $Pb\langle B\rangle O_3$ crystal for which $\langle B\rangle$ represents a virtual atom that is intermediate between Ti and Zr atoms [**29**]. In that simplified case, the doubling of the A_1 mode is still present at 300 K, which implies that such doubling has nothing to do with the presence of two B-atoms in PZT (Ti and Zr). Interestingly, one Raman experiment [**60**] previously reported an active mode with a frequency of $\approx 125 cm^{-1}$ while another infrared measurement indicated a resonant frequency around $160 cm^{-1}$ at room temperature in $Pb(Zr_{0.55}Ti_{0.45})O_3$ solid solution [**53**]. The fact that these two experimental frequencies are very close to our predictions strongly hints towards the possibility that one measurement determined the frequency of what we denoted as the $A_1^{(1)}$ mode while the other measurement "saw" the $A_1^{(2)}$ mode – with none of them suspecting that two modes with A_1 symmetry can exist in PZT at room temperature within the $\approx$ 100 - 170 cm^{-1} range[3] .

More thoughtfully acquired MD simulation data will now be presented to gain insight in to the origin and nature of this unusual doubling of the A_1 mode. Figure 3.5.2 shows the temperature dependence of the resonant frequencies for the A_1 modes obtained from the simulations for $Pb(Zr_{0.47}Ti_{0.53})O_3$. Just below T_c and down to 525K, only a single

[3]Such overlooking of these two modes likely arises from the broadness and thus overlap of the $A_1^{(1)}$ and $A_1^{(2)}$ modes in the Raman spectra. In this frequency range, there is also an E(LO) mode at 100 cm^{-1} (depending on temperature), which creates some confusion in the symmetry assignment of Raman peaks.

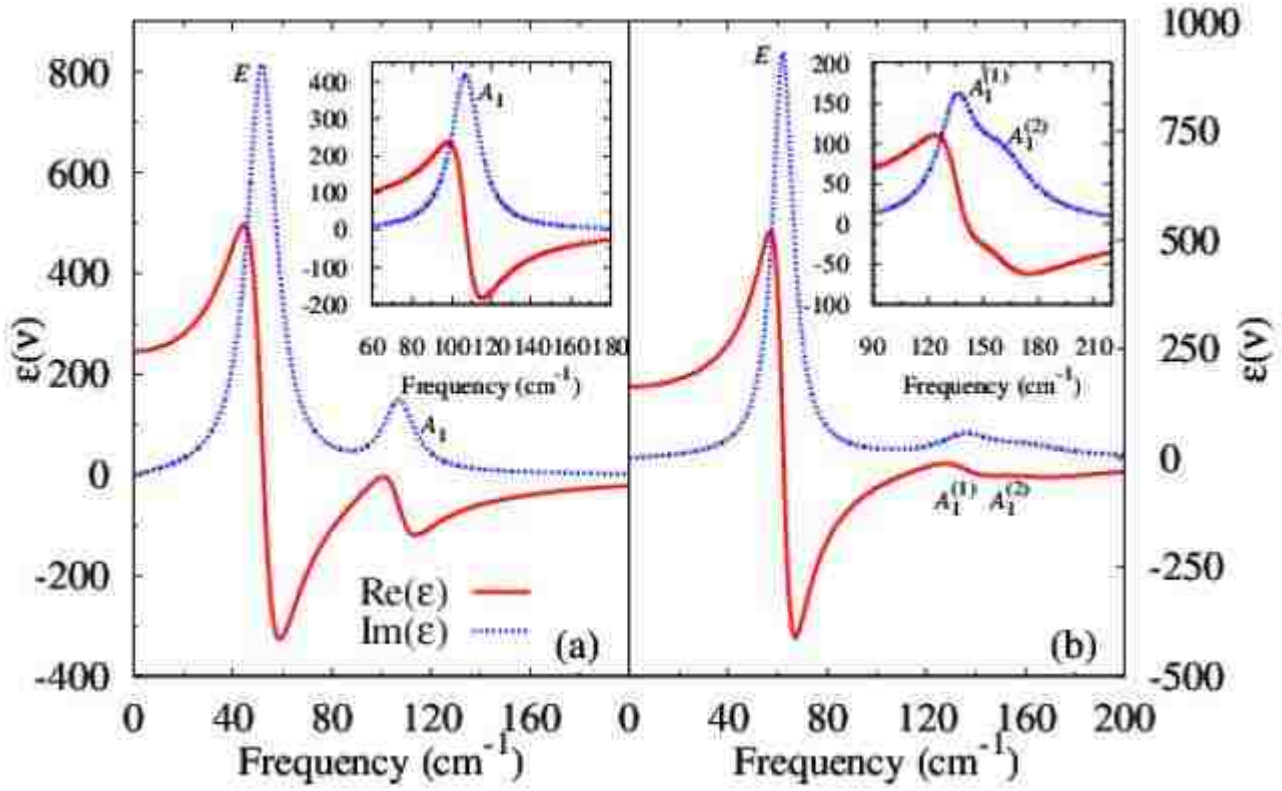

FIGURE 3.5.1. The isotropic dielectric response of the $Pb(Zr_{0.47}Ti_{0.53})O_3$ solid solution versus frequency, at (a) 600 K and (b) 400 K. The insets show the ε_{zz} dielectric response, where z corresponds to the direction of the polarization. Solid and dotted lines represent the real and imaginary parts, respectively, of the complex dielectric responses.

A_1 mode exists. The frequency of this mode follows the usual Curie-weiss behavior, i.e., $\nu_r = C\,|T_c - T|^{1/2}$. On the other hand, for temperatures ranging between 500K and 100 K, two modes of A_1 symmetry exist, with evidently the $A_1^{(1)}$ (respectively, $A_1^{(2)}$) mode having a frequency lower (respectively, higher) than that given by the Curie-Weiss law. Furthermore, for temperatures below 100 K, the $A_1^{(1)}$ and $A_1^{(2)}$ modes merge into a single mode of A_1 symmetry that once again follow this square-root law. Interstingly Fig. 3.5.2 further reveals that when cooling the system the A_1 mode first disappears in favor of the $A_1^{(1)}$ and $A_1^{(2)}$ modes, at a temperature where the frequency of this single A_1 mode is nearly equal to twice the main resonant frequency associated with the antiphase AFD motions[4] (that are

[4]In fact, we found that there is another AFD resonant frequency, in addition to the main one shown in Fig. 3.5.2. For instance, at 500 K, this second frequency occurs at 105 cm^{-1} versus 58 cm^{-1} for the main AFD frequency. Such a second AFD frequency has a peak that is much weaker than the one associated with the main AFD resonant frequency and is caused by alloy effects. Note that, when using the virtual crystal

associated with the R-point of the first-Brillouin zone [**32**]). This phenomena is further confirmed [**59**] by additional calculations in which the resonant frequency of the AFD motions is varied by hand, and strongly suggests that the coupling between the AFD and the soft modes is responsible for the doubling of the A_1 mode. This latter possibility is consistent with the results of additional simulations in which we turned off the AFD motions or switch off the D parameters of Eq. (2.2.3): in such cases, only a single A_1 mode can be seen in the dielectric spectra down to the lowest temperature. For symmetry reasons, only three different kinds of D elements are nonzero and different from each other, namely, $D_{xxxx} = D_{yyyy} = D_{zzzz}$, $D_{xxyy} = D_{yyxx} = D_{yyzz} = D_{zzyy} = D_{zzxx} = D_{xxzz}$, and $D_{xyxy} = D_{yxyx} = D_{yzyz} = D_{zyzy} = D_{zxzx} = D_{xzxz}$. These three kinds of coefficients are hereafter denoted by D_1, D_2, and D_3, respectively. We also numerically found that the D_2 parameter has a stronger effect than the D_1 coefficient on the doubling of the A_1 modes, while the D_3 parameter has essentialy no effect on such doubling. It thus appears that the doubling of the A_1 modes mostly originates from an interaction between longitudinal FE displacement and transverse AFD motions.

The fact that the unusual A_1 mode doubling requires an overtone of the AFD mode to be close to the resonant frequency of the single A_1 mode points towards a a Fermi resonance (FR) associated with non-linear couplings [**62**]. Such phenomenon is well known in molecules [**63, 64**], but much less documented in inorganic crystals, especially in perovskites [**65, 66, 67**]. Note that if the overtone of the AFD mode becomes too far away in frequency from the "bare" single A_1 mode (that can be assumed to coincide with the fitted, Curie-Weiss solid line of Fig. 3.5.2) then the FR cannot occur anymore. This explains the disappearance of the $A_1^{(1)}$ and $A_1^{(2)}$ modes in favor of a single A_1 mode for temperatures below 100 K, as seen in Fig. 3.5.2.

In order to confirm and further understand the proposed FR, let's develop a analytical model considering a structural phase that possesses a spontaneous polarization but in which the AFD $\boldsymbol{\omega}_i$'s do not organize themselves into a long-range order – exactly as in P4mm

approximation [**29**] to treat PZT, only one single AFD peak therefore exists, and two dielectric peaks of A_1 symmetry also occur when twice the frequency of this single AFD mode is near the FE A_1 frequency.

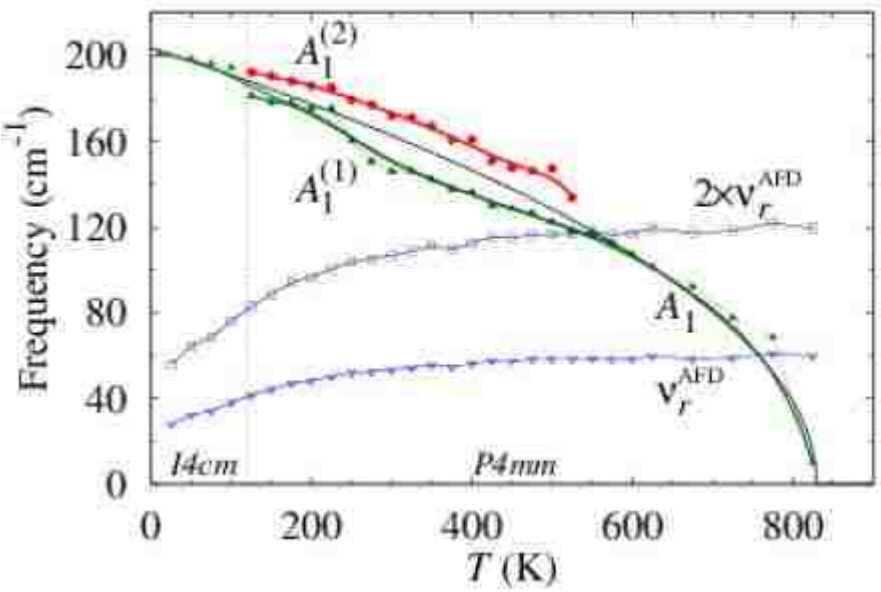

FIGURE 3.5.2. Temperature dependence of the resonant frequency of the A_1 modes and of twice the resonant frequency of the AFD mode in $Pb(Zr_{0.47}Ti_{0.53})O_3$. The thin black solid line represents the fitting of the single A_1 mode, for temperatures above 525 K and its interpolation down to 0 K by the Curie-Weiss square-root law (see text). The crystallographic ferroelectric phases of the system at different temperatures are also indicated.

phase[5]. To simplify the investigation of the dynamics of $\boldsymbol{u}_i$ and $\boldsymbol{\omega}_i$ due to their non-linear couplings, following section 3.4, $\tilde{\mathbf{u}}_\mathbf{i}$ and $\tilde{\boldsymbol{\omega}}_\mathbf{i}$ are introduced such as:

$$\begin{cases} \mathbf{u_i}(\mathbf{t}) = \langle \mathbf{u} \rangle + \tilde{\mathbf{u}}_\mathbf{i}(\mathbf{t}) \\ \boldsymbol{\omega}_\mathbf{i}(\mathbf{t}) = \langle \boldsymbol{\omega}_\mathbf{R} \rangle + \tilde{\boldsymbol{\omega}}_\mathbf{i}(\mathbf{t}) = \quad \tilde{\boldsymbol{\omega}}_\mathbf{i}(\mathbf{t}) \end{cases} \tag{3.5.1}$$

Since here $\langle \boldsymbol{\omega}_\mathbf{R} \rangle = \mathbf{0}$. Plugging Eqn. (3.5.1) into Eqn. (2.2.3), one finds that the essential FE-AFD non-linear coupling term that governs the dynamics of $\tilde{\mathbf{u}}_\mathbf{i}$ and $\tilde{\boldsymbol{\omega}}_\mathbf{i}$ has the following form (see Appendix A):

[5]Note that the present FR occurs well within the stability range of the P4mm phase, which implies that phenomena that are strictly restricted to the vicinity of the ferroelectric phase transition are not fully relevant here.

$$H_{\text{FE-AFD}} \simeq \sum_i \kappa \left|\langle \boldsymbol{u} \rangle\right| \tilde{u}_{\mathbf{i}} (\tilde{\boldsymbol{\omega}}_i)^{\mathbf{2}}, \tag{3.5.2}$$

where $\tilde{\mathbf{u}}_{\mathbf{i}}$ corresponds to the (small and long-range correlated) motion along the polarization direction, and $\tilde{\boldsymbol{\omega}}_{\mathbf{i}}$ corresponds to (small and long-range correlated) AFD motions either perpendicularly to the polarization direction (in that case, the parameter is related to the D_2 parameter) or parallel to that direction (in that case, is proportional to D_1). The dynamical equation for $\tilde{u}_{\mathbf{i}}$ is thus:

$$\frac{d^2 \tilde{u}_{\mathbf{i}}}{dt^2} + 4\pi^2 \nu_{A_1}^2 \tilde{u}_i + \frac{\kappa \left|\langle \boldsymbol{u} \rangle\right|}{m_u} (\tilde{\omega}_{\mathbf{i}})^2 = \frac{Z^* E(\mathbf{t})}{m_u}, \tag{3.5.3}$$

where ν_{A_1} is the natural frequency of the "bare" FE soft mode along the direction of polarization, and m_u is the soft mode effective mass. $E(t)$ is an applied ac electric field. Equation (3.5.3) further proves the existence of a coupling between the dynamical small (long-range correlated) displacement of the square of the AFD motion and the dynamical small (long-range correlated) displacement of the soft mode in a polar phase, which is consistent with the proposed occurrence of FR involving AFD overtone. One can prove (see Appendix A) that when ν_{A_1} is close to twice the AFD resonance frequency, Eqn. (3.5.3) leads to two resonant frequencies for the A_1 mode that are given by $\nu_r^2 = \nu_{A_1}^2 \pm \Omega^2$, where Ω^2 depends on the κ coupling parameter, as well as, on the value of the spontaneous polarization. As Eqn. (3.5.3) and ν_r^2 bear similarities to the analogous expressions for typical FR (see e.g., Ref.[**68**] and references therein), simulations indeed predict that, as a consequence of the coupled dynamics of the FE and AFD modes, a FR occurs in PZT and manifests itself as the doubling of the A_1 mode.

CHAPTER 4

Disordered (Ba,Sr)TiO_3 bulk and epitaxially strained $SrTiO_3$ thick films: Results and discussion

In this section, the dielectric response of (Ba,Sr)TiO_3 (BST) and epitaxially strained $SrTiO_3$ (STO) thick films at finite temperatures and for different Ba compositions will be first examined to uncover/confirm new modes and their charactersitics will be discussed. Special attention will be given to the central mode (CM) reported/speculated in these systems for temperatures lying in the vicinity of the FE phase transition. Second, subjecting these systems to direct-current (DC) electric fields, their dielectric tunability will be computed and compared with Landau-Devonshire based phenomenological predictions formulated in section 2.3.

4.1. Temperature evolution of low-frequency modes

4.1.1. $SrTiO_3$ bulk. MD simulations of $SrTiO_3$ (STO) bulk were carried out on $12 \times 12 \times 12$ supercells. Simulation parameters used were $N_{NPT} = 100000$, $N_{EQ} = 40000$ and $N_{NVE} = 7300000$. Simulations were conducted for temperature in the interval 700-130 K, starting from 700 K and descending. No ferroelectric (FE) phase transition (PT) occurred for STO in this interval in agreement with experimental observations [**69**]. An example of the dielectric response obtained through Eqn.(2.1.4) is shown in Fig. 4.1.1(a), where the imaginary part of the isotropic dielectric response is given at 340 K. For all temperatures investigated, a single classical damped harmonic oscillator (DHO) of the form $\varepsilon(\nu) = S\nu_r^2 / \left(\nu_r^2 - \nu^2 + i\gamma\nu\right)$, where ν_r, γ and S are the resonant frequency, damping constant and strength of the corresponding mode, respectively, was sufficient to fit the dielectric response successfully. Soft mode (SM) frequencies and their respective dielectric strengths found from such fittings for each temperature are shown in Fig. 4.1.2.

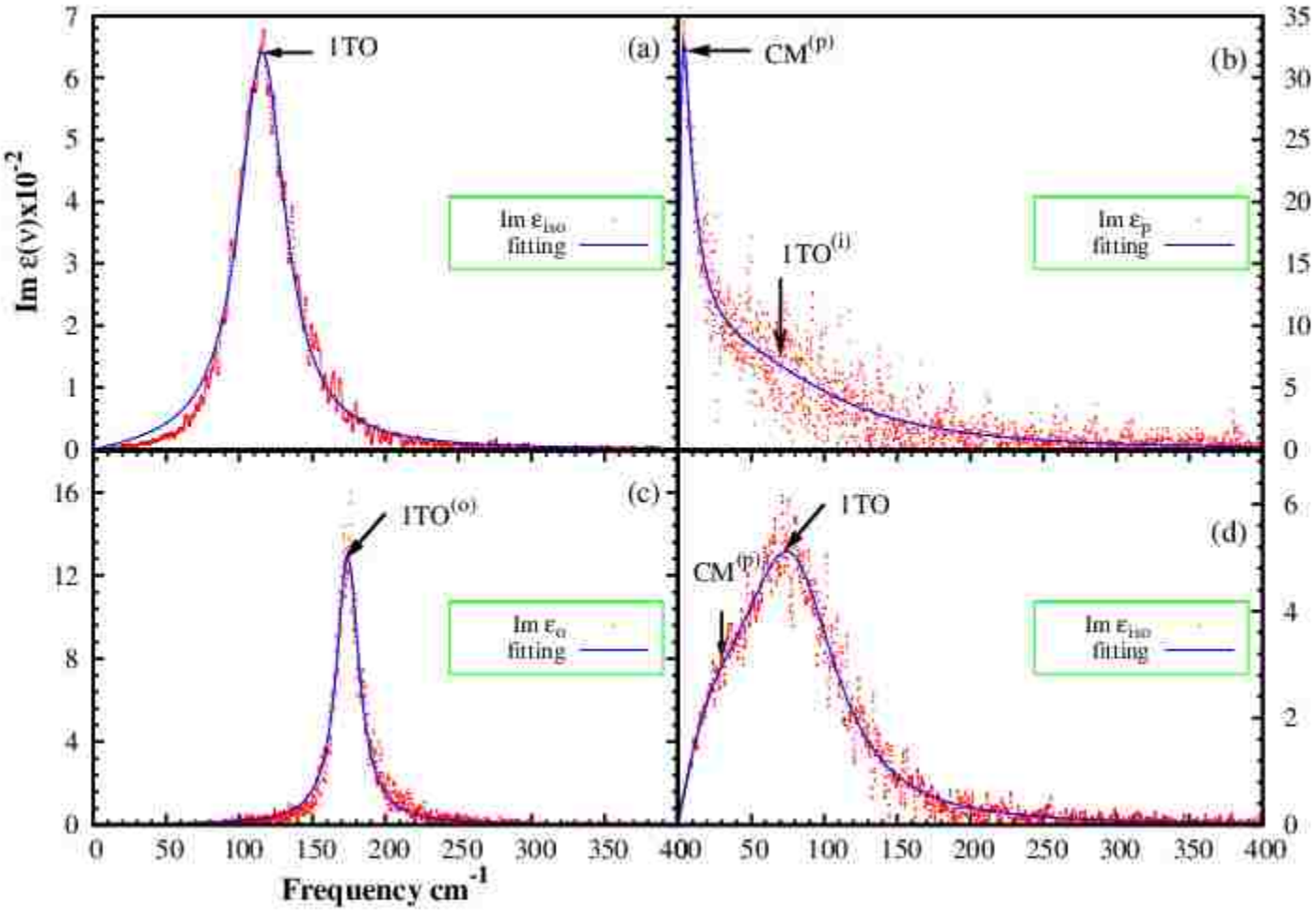

FIGURE 4.1.1. Imaginary part of the dielectric response as a function of frequency at 340 K from MD simulations(in red) and its fitting(in blue) using an appropriate oscillator model (see text). Panel (a) shows the isotropic dielectric response, Im ε_{iso} of $SrTiO_3$ bulk. Panel (b) displays the in-plane dielectric response, Im $\varepsilon_p(\nu)$ of strained $SrTiO_3$ film. Panel (c) displays the out-of-plane dielectric response, Im $\varepsilon_o(\nu)$ of strained $SrTiO_3$ film. Panel (d) shows the isotropic dielectric response, Im ε_{iso} of $Ba_{0.5}Sr_{0.5}TiO_3$ bulk.

4.1.2. Epitaxially strained $SrTiO_3$ thick films. MD simulations of epitaxially strained STO thick films were conducted on $14 \times 14 \times 14$ supercells. Simulation parameters used were $N_{NPT} = 160000$, $N_{EQ} = 100000$ and $N_{NVE} = 25500000$. Substrate lattice constant (a_{sub}) was chosen to be 7.577 Bohr so that it induces an epitaxial strain of ~+1.6% comparable to that induced by $DyScO_3$ on STO, which is known to be ~+1% [**70**]. Simulations were

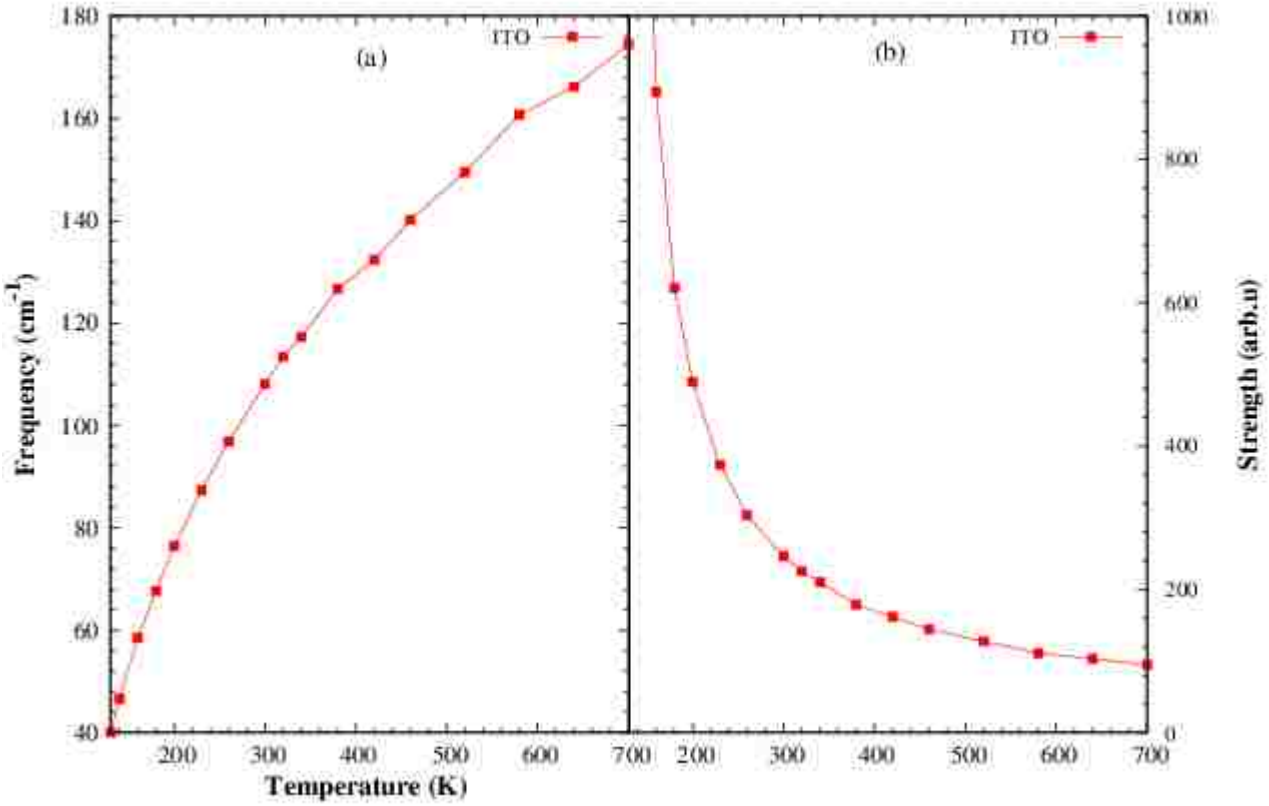

FIGURE 4.1.2. Temperature dependence of some soft mode (1TO) characteristics. Panel (a) displays resonant frequency of soft mode. Panel (b) displays dielectric strength.

conducted for temperatures in the interval 900-130 K, starting from 900 K and descending. FE phase transition to orthorhombic, Amm2 phase was seen at the Curie temperature T_c~305 K, in accordance with the PT observed for STO grown on $DyScO_3$ with a critical temperature T_c~293 K or T_c~270 K [**70, 71**], proving the accuracy and reliability of the approach. An example of the imaginary part of the in-plane dielectric response obtained using Eqn.(2.1.4) at 340 K is shown in Fig. 4.1.1(b). Unlike in Fig. 4.1.1(a) for STO bulk, one can clearly see in this figure the presence of a lower frequency Debye-like mode in addition to the higher frequency soft mode (SM). Spectroscopic measurements carried out by J. Hlinka et al. [**24**] on $BaTiO_3$ confirmed the existence of such a relaxational mode, which is generally referred to as central mode (CM). These authors went on to show that hopping between

potential minima is the cause of this central mode. This second peak is in fact visible for all temperatures investigated in the interval of 500-180 K. To account simultaneously for SM and CM appearing in the in-plane dielectric response $\varepsilon(\omega)$ - a model consisting of a damped harmonic oscillator (DHO) and a Debye mode can be constructed as follows;

for two degrees of freedom :

$$\varepsilon(\omega) = \begin{bmatrix} S_1 & S_2 \end{bmatrix} \begin{bmatrix} 1 - i\omega/\omega_R & \delta \\ \delta & \omega_0^2 - \omega^2 - i\omega\gamma \end{bmatrix}^{-1} \begin{bmatrix} S_1 \\ S_2 \end{bmatrix}$$

considering central mode (CM) to be a silent mode (i.e. S_1=0) we obtain :

$$\varepsilon(\omega) = \frac{S_2^2}{\omega_0^2 - \omega^2 - i\omega\gamma - \delta^2/(1 - i\omega/\omega_R)} \tag{4.1.1}$$

where S_2, ω_0, γ are the dielectric strength, frequency and damping constant of the SM, respectively; ω_R and δ are the relaxation frequency of the CM and the coupling coefficient between SM and CM, respectively. Successful and physically meaningful fits of the in-plane dielectric response for all temperatures investigated in the interval of 500-180 K were obtained using Eqn.(4.1.1). For temperatures above 500 K, a single damped harmonic oscillator was sufficient to fit the in-plane dielectric response. In fact, three distinct peaks were visible in the in-plane dielectric response for temperatures below 270 K. Examination of the dielectric response along the direction of polarization [110] and perpendicular to it (i.e., $\left[\bar{1}10\right]$) shows that the third mode arose because of the splitting of the in-plane SM in the FE phase giving a lower frequency mode of B_2 symmetry corresponding to oscillations in the (001) plane and a higher frequency A_1 mode with oscillations along [110]. Hence, this A_1 mode was accounted for, by fitting the response after the addition of an uncoupled DHO to Eqn.(4.1.1). Interestingly for all temperatures investigated a single peak was visible in the out of plane dielectric response (see Fig. 4.1.1(c)). This peak was fitted using the customary single DHO model and it has B_1 symmetry with oscillations along [001]. Symmetries of all these modes are inline with that of group theory predictions. Mode frequencies, spectral weights, and the

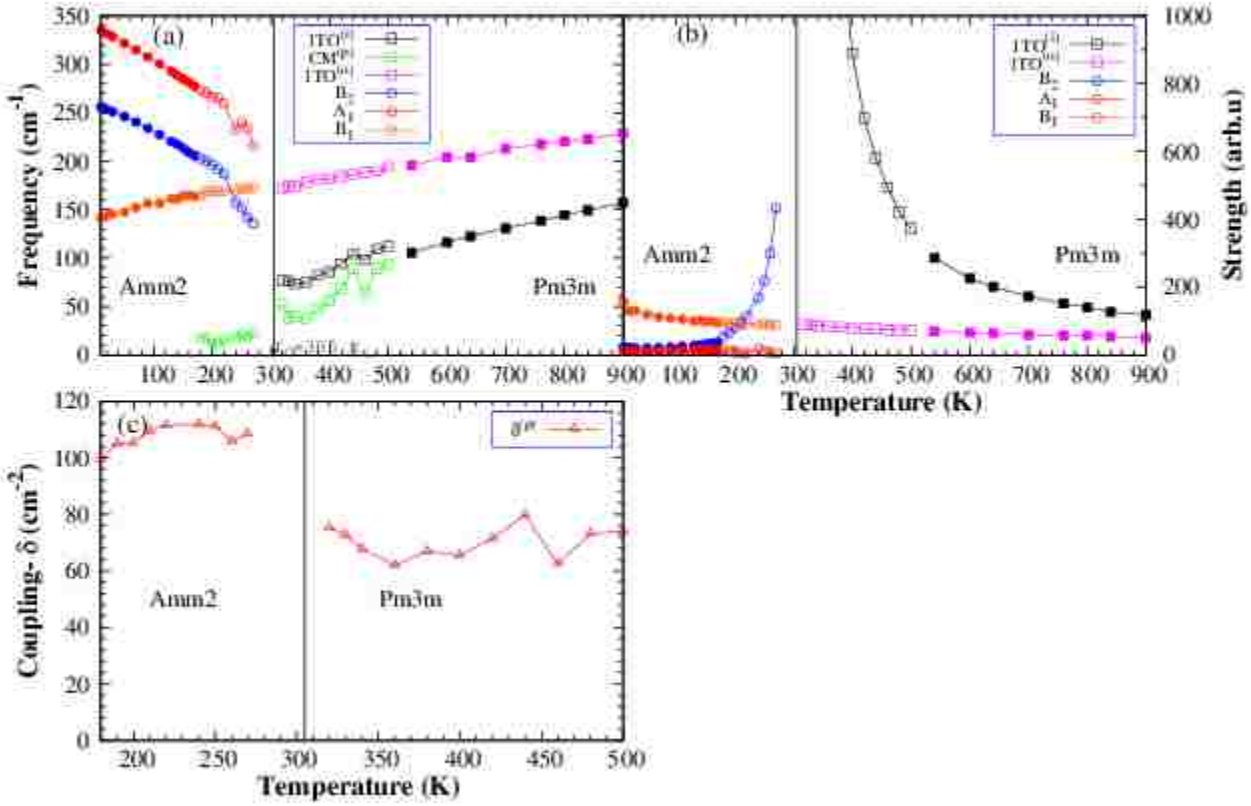

FIGURE 4.1.3. Temperature dependence of some properties of lowest-in-frequency modes of strained $SrTiO_3$ films. Panel (a) displays resonant frequencies of modes. Panel (b) displays dielectric strength of modes. Panel (c) shows coupling coefficient between CM and other modes from fitting (see text). Solid vertical lines mark phase boundaries and FE phases are indicated.

coupling constants obtained through these fittings are shown in Fig. 4.1.3 as a function of temperature. Data for ω_R and SM are in remarkable agreement with those obtained from Fourier transform infrared reflectence (FTIR) spectra in Ref.[**71**] for 100 nm thick STO films grown on $DyScO_3$. The coupling coefficient for the cubic phase as well as the FE phase was found to be nearly constant in each phase, although in the FE phase, δ was slightly higher with respect to that of the cubic phase.

4.1.3. $Ba_{0.5}Sr_{0.5}TiO_3$bulk. MD simulations for $Ba_{0.5}Sr_{0.5}TiO_3$(BST) bulk were carried out on $12 \times 12 \times 12$ supercells. Simulation parameters used were $N_{NPT} = 100000$,

$N_{EQ} = 40000$ and $N_{NVE} = 13060000$. Simulations were conducted for temperature in the interval 700-130 K, starting from 700 K and descending. Cubic ($Pm\bar{3}m$) to tetragonal (P4mm), Tetragonal to Orthorhombic (Amm2), and Orthorhombic to Rhombohedral (R3m) phase transitions occurred at transition temperatures that were in excellent agreement with experimental measurements [**69, 72**]. An example of imaginary part of the isotropic dielectric response obtained using Eqn.(2.1.4) at 340 K is shown in Fig. 4.1.1(d). Similar to strained STO films, here we can see an additional peak of Debye relaxation (CM) type. This peak was observed for all temperatures investigated below 400 K, thus the model given by Eqn.(4.1.1) was employed to fit these two peaks. It is noteworthy that, a recent first-principles-based investigation [**73**] of BST using the effective Hamiltonian method also yielded similar output but in this case the SM and CM were fitted using two uncoupled DHO's, which the author believe does not adequately account for the Debye like nature of the CM and more importantly neglects the important coupling between SM and CM. The present approach gives CM frequencies in much better agreement with experiment [**71**], especially in the FE phase. Below T_c, three peaks were observed in the dielectric response parallel to the direction of polarization in both P4mm and Amm2 phases, which were fitted using an extra uncoupled DHO added to Eqn.(4.1.1). The lowest is a relaxational mode and is denoted $CM^{(f)}$ and the highest frequency peak is found to be of A_1 symmetry while the other peak has B_2 symmetry. Perpendicular to the direction of polarization two peaks are observed, of which the lower is a relaxational mode, denoted $CM^{(p)}$ and was fitted using Eqn.(4.1.1). $CM^{(p)}$ occurs due to transitions between ferroelectric phases while the other mode is found to have B_1 symmetry and it 'drives' the transitions between ferroelectric phases as evidenced by its softening approaching the phase boundaries and the spike in its spectral weight crossing the phase boundaries (see Fig. 4.1.4(b)). Symmetries of all these modes in each FE phase are compatible with group theory predictions. Mode frequencies, spectral weights and the coupling coeffiecient obtained from these fittings are shown in Fig. 4.1.4. Similar to strained STO films, coupling coefficients, δ are constant in each phase, but δ for $CM^{(p)}$ is lower to that of $CM^{(f)}$ in FE phases.

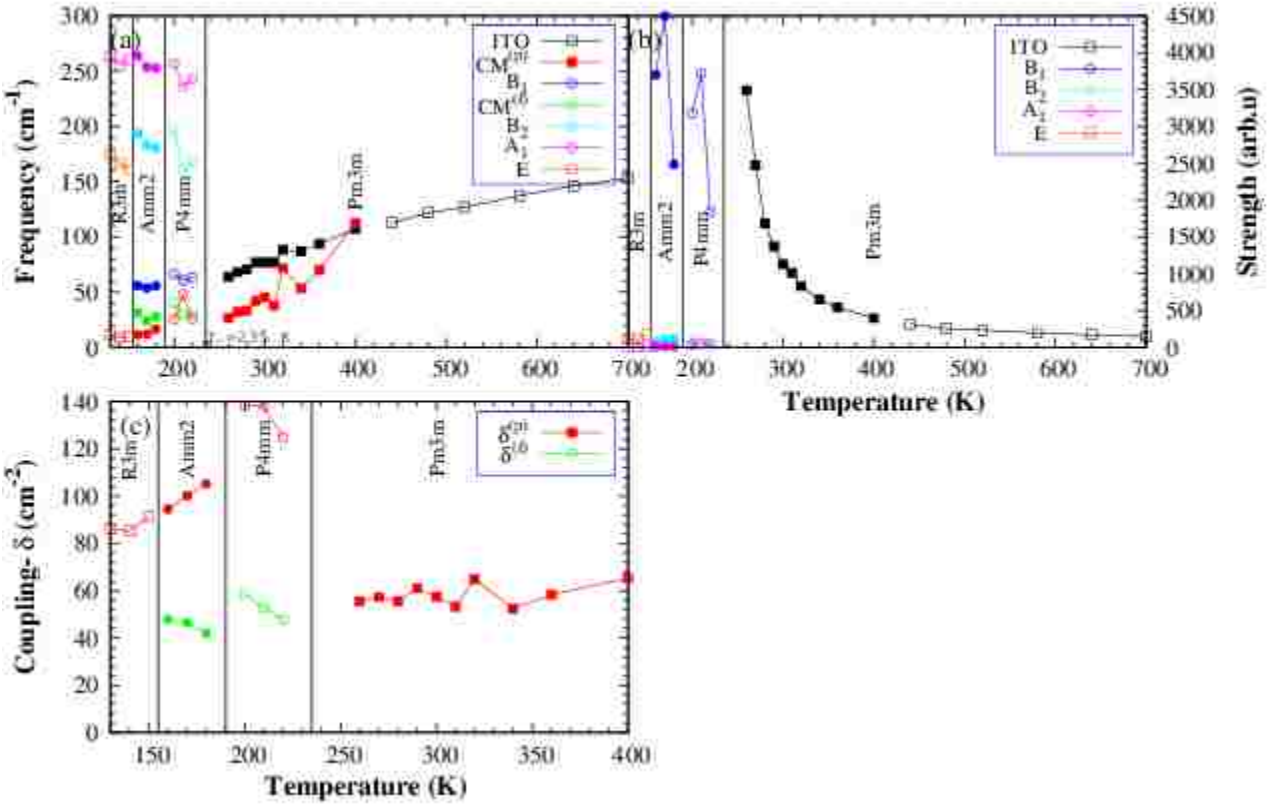

FIGURE 4.1.4. Temperature dependence of some properties of lowest-in-frequency modes of $Ba_{0.5}Sr_{0.5}TiO_3$ bulk. Panel (a) displays resonant frequencies of modes. Panel (b) displays dielectric strength of modes. Panel (c) shows coupling coefficient between CM and other modes from fitting (see text). Solid vertical lines mark phase boundaries and FE phases are indicated.

Comparison of MD simulation results of Fig(s). 4.1.2, 4.1.3 and 4.1.4 confirms that chemical substitution with Ba or epitaxial strain in STO can cause an increase in Curie temperature and generate a relaxation mode not seen in STO bulk. Furthermore, effective Hamiltonian approach predicts temperature evolution with striking accuracy for the CM frequencies, observed through various measurements in strained STO and BST [**71, 74**]. Yet, it raises many important questions such as why does the transition temperature T_c, change from system to system? what causes the CM? Why is the CM visible in BST systems and not in some other perovskite systems such as PZT? Why is the range in paraelectric

phase in which the CM appears different among these systems? Let's attempt to answer these questions with the aid of further information obtained from the MD simulations.

4.1.4. Mechanics of transition temperature, T_c, in BST systems. MD simulations were performed for BST bulk systems with atomic Ba compositions that change by steps of 10%. Simulation parameters are those of $Ba_{0.5}Sr_{0.5}TiO_3$ described above. To answer the first question above, the Curie temperatures (T_c) of these systems were found and plotted against their respective low-temperture ferroelectric potential well depths ϕ, for each system and are shown in Fig. 4.1.5(a). The linear relationship which has a proportionality constant in the order of the Boltzmann constant (i.e. $\phi \sim kT_c$) between T_c and ϕ proves that chemical substitution or strain causes ϕ, to change which in turn causes a proportional change in T_c.

In order to understand what causes ϕ to change among these systems we need to closely examine the alloy effective Hamiltonian (Eqn.(2.1.1)). Terms involving the local soft mode $\{u_i\}$ in this Hamiltonian are the ones that directly affects the dynamics of the local soft mode. Moreover, among these terms E^{ionic} given in Eqn.(2.1.3) and E^{int} given in Eqn.(2.1.2) are the ones that are primarily affected by chemical substitution and/or strain and they can be coalesced to give electrostriction energy, E^{str} as follows;

$$E^{str}(\{u_i\},\{\eta_l\}) = E^{ionic} + E^{int} = \frac{1}{2}\sum_i \sum_{l\alpha\beta} B_{l\alpha\beta}\eta_{tot,l}(i)\, u_{i,\alpha} u_{i,\beta} \tag{4.1.2}$$

where i runs over all the unit cells, α and β denote Cartesian components, $B_{l\alpha\beta}$ are coupling parameters [**20, 22**] and $\eta_{tot,l}(i) = \eta_{H,l}(i) + \eta_{I,l}(i) + \eta_{loc,l}(i)$. The coefficient signifying total harmonic contribution of the local soft mode, say is κ'_α for the α cartesian component of the local mode. Then from Eqn.(2.1.2) and Eqn.(4.1.2) κ'_α can be given by;

$$\kappa'_\alpha = \kappa + \frac{1}{2}\left[B_{1\alpha\alpha}\eta_{H,1}(i) + B_{2\alpha\alpha}\eta_{H,2}(i) + B_{3\alpha\alpha}\eta_{H,3}(i) + (B_{1\alpha\alpha} + B_{2\alpha\alpha} + B_{3\alpha\alpha})\,\eta_{loc}(i))\right] \tag{4.1.3}$$

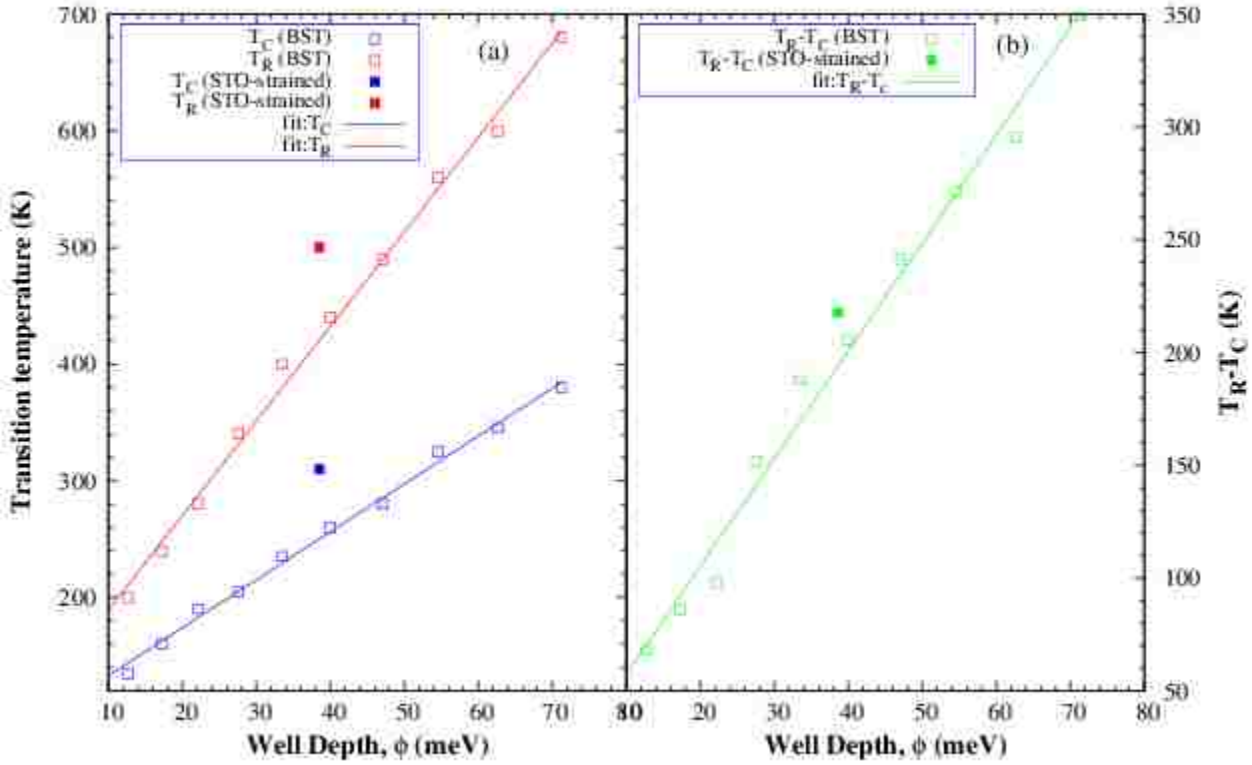

FIGURE 4.1.5. Transition temperature charcteristics of BST bulk and epitaxially strained STO films as a function of potential well-depth ϕ. Panel (a) displays Curie temperature T_c, and CM emergence temperature T_R. Panel (b) shows the temperature range in which the CM is visible in the paraelectric phase (T_R-T_c).

where κ is total harmonic contribution from E^{self}, E^{dip} , and E^{short} terms of Eqn.(2.1.2). κ'_α computed from Eqn.(4.1.3) for some of the systems investigated are shown in Table 4.1.1. It is thus clear that the differences in E^{str} drives the change in κ'_α which in turn affects the well-depth, ϕ. Furthermore, one can see that the FE phase to which each system transforms below T_c is also determined by how κ'_x, κ'_y, and κ'_z compare with each other for a particular system. That is κ'_α has the highest values for STO bulk explaining the absense of PT in this system. For epitaxially strained STO films $\kappa'_x = \kappa'_y < \kappa'_z$, which explains why we observe an $Pm\bar{3}m$ to orthorhombic Amm2 transition in this system. Moreover, the inequality between the in-plane coefficients and out of plane cofficient is the cause of the splitting in the SM

System	κ'_x	κ'_y	κ'_z
$SrTiO_3$	-0.015303	-0.015303	-0.015303
$Ba_{0.5}Sr_{0.5}TiO_3$	-0.026472	-0.026472	-0.026472
$BaTiO_3$	-0.037641	-0.037641	-0.037641
Strained $SrTiO_3$	-0.032388	-0.032388	-0.015303

TABLE 4.1.1. Cartesian components, κ'_α of harmonic contribution of local soft mode, $\{u_i\}$, for different systems investigated.

in this system in the paraelectric phase. For $Ba_{0.5}Sr_{0.5}TiO_3$ and $BaTiO_3$, $\kappa'_x = \kappa'_y = \kappa'_z$, but are lower than STO explaining the cause of Pm3m to P4mm transition and the closely spaced other FE transitions down to R3m.

4.1.5. Origin of central mode (CM) in perovskites. As mentioned earlier, previous MD simulation of $BaTiO_3$ supported by spectroscopic measurements [**24**] showed that hopping between potential minima of the local mode is responsible for the appearance of the CM in its ferroelectric phase. Time evolution of the local modes of an arbitrary site of BST systems indicate that such hopping exists in both FE and PE phases of all systems investigated. As an example, time evolution of an arbitrary $Ba_{0.5}Sr_{0.5}TiO_3$ site is shown in Fig. 4.1.6 for different temperatures (and thus for different phases). So what causes this hopping?

The short answer is that strong E^{str} term is the cause of this hopping in BST. E^{str} prefers the polarized state of a site, thus when tensile $\eta_{loc,l}(i)$ increases due to Ba substitution or when $\eta_{H,l}(i)$ is increased due to epitaxial strain the local mode become increasingly unstable in the PE phase. Let's denote T_R as the highest temperature at which the CM is visible, $T_R - T_c$ is displayed as a function of well depth ϕ, in Fig. 4.1.5(b). The linear proportionality clearly indicates that strengthening E^{str} results in the expansion of the temperature range in which the CM appears in the PE phase, supporting the above claim.

But why does CM arise in BST and not in some of the other well known perovskites like PZT, which have even higher T_c? A possible reason is that E^{str} is considerably weaker in these systems. In PZT for instance, B_{1xx}- by far the largest expansion parameter among the $B_{l\alpha\beta}$ coefficients in both BST and PZT is an order of a magnitude smaller in PZT.

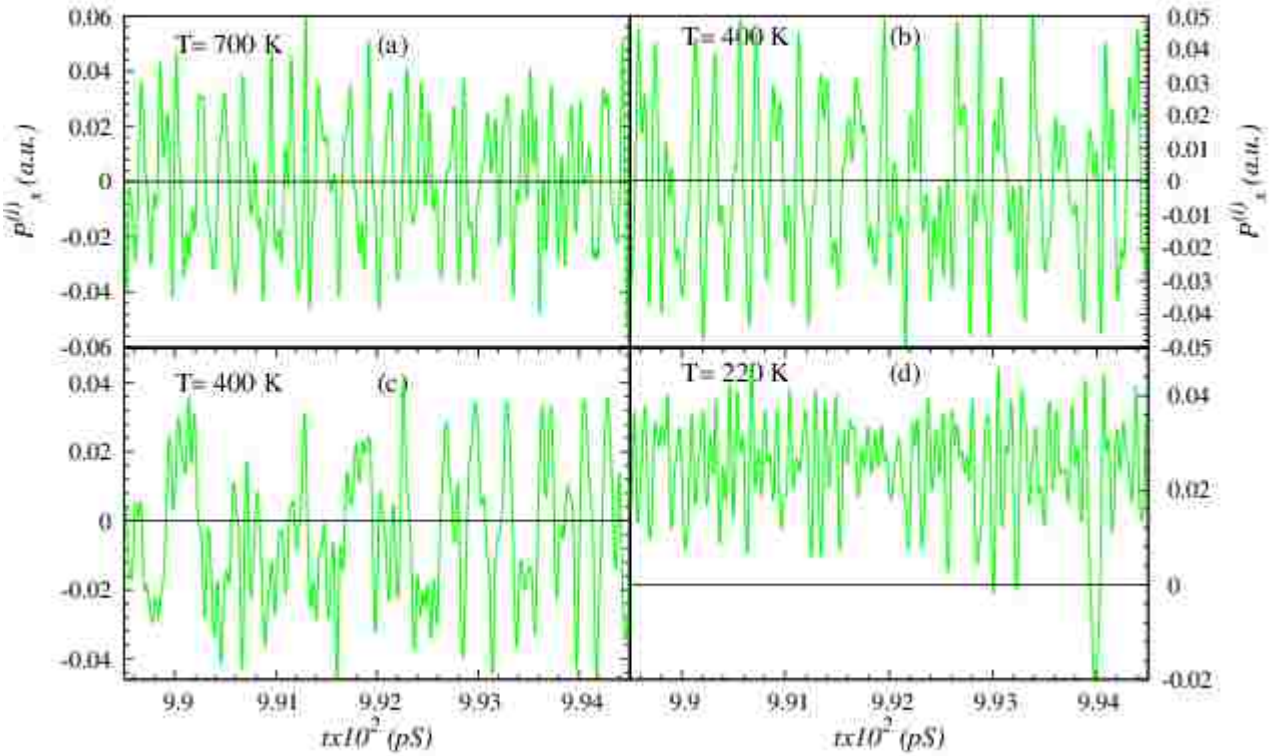

FIGURE 4.1.6. Time evolution of the x-component of an arbitrarly selected site of $Ba_{0.5}Sr_{0.5}TiO_3$ bulk for different temperatures.

Furthermore, $\eta_{loc,l}(i)$ is insignificant in the effective Hamiltonian of PZT. Thus, E^{str} is much weakened in PZT and CM does not arise.

4.2. Dielectric Tunability of (Ba,Sr)TiO_3 bulk and epitaxially strained $SrTiO_3$ thick films

4.2.1. $SrTiO_3$ bulk. Dielectric tunability $\tau(E)$, at ν=10 GHz of $SrTiO_3$ bulk was obtained following the method described in section 2.3, as a function of DC electric field applied along [001] through MD simulations conducted at 320 K. Simulations were conducted up to a maximum field of 240 MV/m. Figures 4.2.1(a), (b) and (c) display $\tau(E)$, the soft mode frequency, and its corresponding strength determined from the complex dielectric response as a function of the bias electric field. $\tau(E)$ and soft mode frequencies thus obtained were in

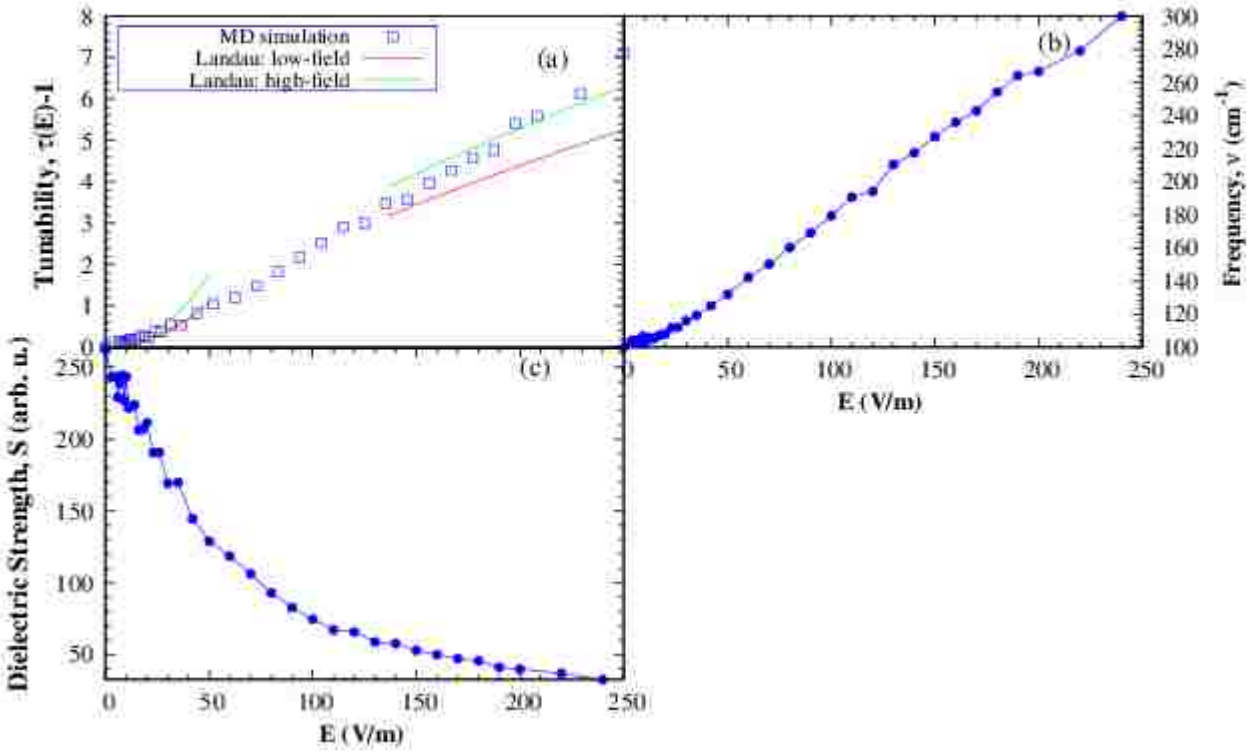

FIGURE 4.2.1. Electric field dependence of dynamical properties of STO bulk at 300 K. Panel (a) display low-field (green) and high-field (red) Landau-Devonshire fittings of simulation data for tunability. Panel (b) shows resonant frequency of soft-mode. Panel (c) shows dielectric strength of soft-mode.

remarkable agreement with spectroscopic measurements for $SrTiO_3$ [**75, 14**] and shows the low tunability of this system. Furthermore, the soft mode "hardened" with increased field-E as speculated by measurements [**75**].

Fitting of $\tau(E)$ was accomplished as follows: first the zero-field dielectric constant $\varepsilon(0)$ at 10 GHz, obtained from MD simulations as a function of temperature in the PE phase, was fitted (see Fig. 4.2.2) using Eqn.(2.3.3) and thence $\varepsilon(0)$ at 300 K was determined. Then, Eqn.(2.3.5) was used to fit the low-field tunability after substituting with this $\varepsilon(0)$. The fitting parameter β thus determined was thereafter substituted into Eqn. (2.3.7) for high-field tunability and was plotted together with Eqn.(2.3.5) for low-field tunability (see Fig. 4.2.1(a)). Apparently and as expected from Landau-Devonshire theory, the high-field

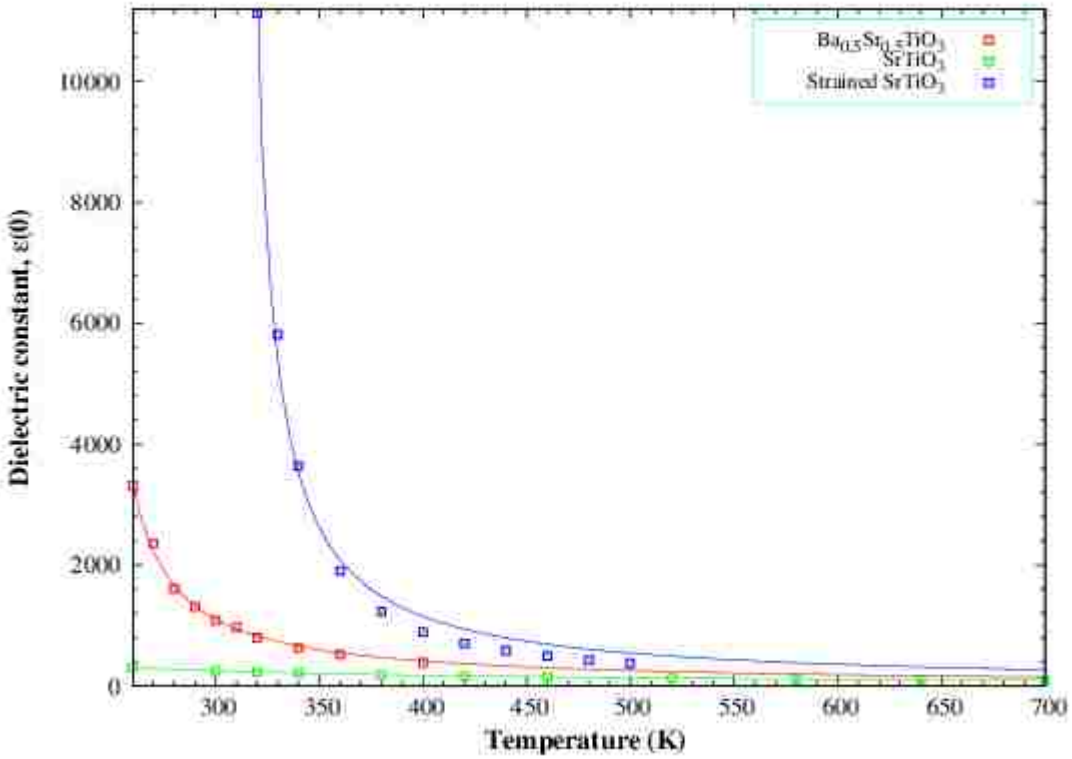

FIGURE 4.2.2. Temperature dependence of zero-field dielectric constant $\varepsilon(0)$ at 10GHz for $SrTiO_3$ (green), $Ba_{0.5}Sr_{0.5}TiO_3$ (red) and strained $SrTiO_3$ (blue). Points are computations from MD simulations while lines represent fittings by Curie-Weiss Law.

plot has roughly the same β value as that of the low-field plot. High-field tunability was then fitted using Eqn. (2.3.7) and with β deduced from this fit, subsequently Eqn.(2.3.5) for low-field tunability was plotted. Once again, we can see that the high-field fitting parameter for β is similar that of low-field supporting the Landau-Devonshire theory. The β values obtained in both instances as well as $\varepsilon(0)$ at 300 K from the Curie-Weiss fit are in good agreement with known experimental data [**75, 14**] for $SrTiO_3$ and are given in Table 4.2.1.

4.2.2. Epitaxially strained $SrTiO_3$ thick films. Now let's examine the effect of epitaxial strain on dielectric tunability. For this purpose the strained $SrTiO_3$ thick film discussed in section 4.1 was considered and $\tau(E)$ at $\nu = 10GHz$ was obtained, following the method described in section 2.3 as a function of a DC electric field applied along [110],

through MD simulations conducted at 320 K. Simulations were conducted up to a maximum field of 100MV/m. Figures 4.2.3(a), (b) and (c) display $\tau(E)$, mode frequencies, and their corresponding strengths determined from the complex dielectric response as a function of the bias electric field. Recently $SrTiO_3$ films grown on $DyScO_3$ have been receiving a lot of attention due to its enormous tunability close to room temperture [**14, 77, 78**]. The system investigated here is similar and $\tau(E)$ displayed in Fig. 4.2.3(a) confirms the gigantic leap in tunability of $SrTiO_3$ when under epitaxial strain. Moreover the soft mode (SM) as well as the central mode (CM) have frequencies shown in Fig. 4.2.3(b), which are in excellent agreement with reported spectroscopic measurements [**71, 78**] and the SM hardens in a strikingly similar manner with the applied electric field [**78**]. However, the CM somewhat softens with increasing electric field especially in the low-field limit. This is in contrast to the assumption held that CM is a constant of electric field, in fitting spectroscopic measurements [**78**]. Next, $\tau(E)$ in the low-field limit and high-field limit was fitted using Eqns. (2.3.5) and (2.3.7) respectively, following the same approach discussed for $SrTiO_3$. It is found that $\varepsilon(0)$ for 320 K, obtained from the PE phase Curie-Weiss fit using Eqn.(2.3.3) is two order of magnitude larger, to that of $SrTiO_3$ bulk and has excellent agreement with experimental measurements [**78**]. Unsurprisingly, β deduced from the high-field fit is of the same order as of $SrTiO_3$ bulk as expected from Landau-Devonshire theory. But intriguingly, β for low-field is couple of orders of magnitude smaller comparatively. Hence, Landau-Devonshire theory is no longer accurate in predicting tunability when $SrTiO_3$ is epitaxially strained. Since the CM softens considerably and is stronger in the low-field limit with respect to the high-field range correlating with the descripancy of β values, the author believe's that the appearance of the CM causes β to lower drastically resulting in a much lower tunability at low-field than predicted by Landau-Devonshire theory. Subsequent investigation of the tunability of $Ba_{0.5}Sr_{0.5}TiO_3$ bulk will substantiate this claim further.

4.2.3. $Ba_{0.5}Sr_{0.5}TiO_3$bulk. Effect of chemical substitution on dielectric tunability will now be examined by considering $Ba_{0.5}Sr_{0.5}TiO_3$ bulk system. Dielectric tunability $\tau(E)$, at $\nu = 10GHz$ was obtained following the method described in section 2.3, as a function

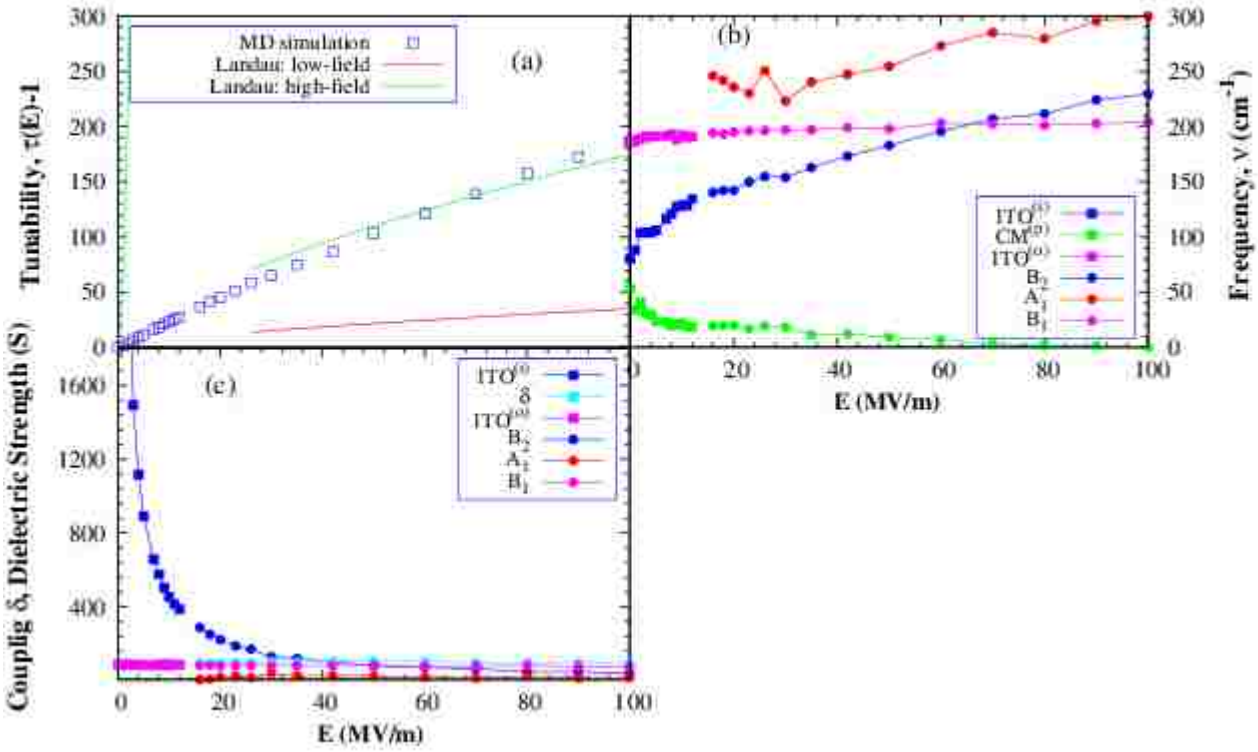

FIGURE 4.2.3. Electric field dependence of dynamical properties of strained STO thick film at 320 K. Panel (a) displays low-field (red) and high-field (green) Landau-Devonshire fittings of simulation data for tunability. Panel (b) shows resonant frequencies of peaks in dielectric response. Panel (c) shows dielectric strength of modes and coupling coefficient (δ).

System	Temperature(K)	Dielectric constant,$\varepsilon(0)$	Low-field β-β_L	High-field β-β_H
$SrTiO_3$	300	247	1.49E+10	2.38E+10
Strained $SrTiO_3$	320	11230	1.75E+8	2.04E+10
$Ba_{0.5}Sr_{0.5}TiO_3$	270	2216	2.71E+9	1.75E+11

TABLE 4.2.1. Comparison of zero-field dielectric constant and β from low-field, β_L and high-field, β_H for systems from MD simulations.

of a DC electric field applied along [100] through MD simulations conducted at 270 K. Simulations were conducted up to a maximum field of 100 MV/m. Figures 4.2.4(a), (b) and (c) show $\tau(E)$, the mode frequencies, and their corresponding strengths determined from the complex dielectric response as a function of the bias electric field. $Ba_{0.5}Sr_{0.5}TiO_3$ has been investigated extensively over a lengthy period of time due its high permittivity and

tunability at room temperature [**14**]. Tunability$\tau(E)$, SM frequencies as well as the electric field hardening of SM at low fields displayed in Figs. 4.2.4(a) and (b) are compatible with spectroscopic measurments [**79**]. Just as in strained $SrTiO_3$, the CM softens appreciably with increasing field, noticeably in the low-field region. Dielectric tunability $\tau(E)$, in the low-field limit and high-field limit was fitted using Eqns. (2.3.5) and (2.3.7) respectively, following the same approach discussed before. Zero-field dielectric constant, $\varepsilon(0)$ for 270 K calculated from the PE phase Curie-Weiss fit using Eqn.(2.3.3) is two orders of magnitude larger to that of $SrTiO_3$ bulk and has excellent agreement with spectroscopic measurements [**14, 79**]. Parameter β, deduced from the high-field fit is in good agreement with experimental values reported in literature [**79**]. Moreover, as in strained $SrTiO_3$ film, β for low-field is couple of orders of magnitude smaller comparatively with $SrTiO_3$ bulk. Peculiarly, similar to strained $SrTiO_3$ film the CM is stronger and soften considerably more in the low-field region as opposed to the high-field region coincident with substantially lower tunability at low-field than predicted by Landau-Devonshire theory. Therefore our claim that the CM in low-field limit is causing the drastic drop in tunability than anticipated by Landau-Devonshire theory is further strengthened.

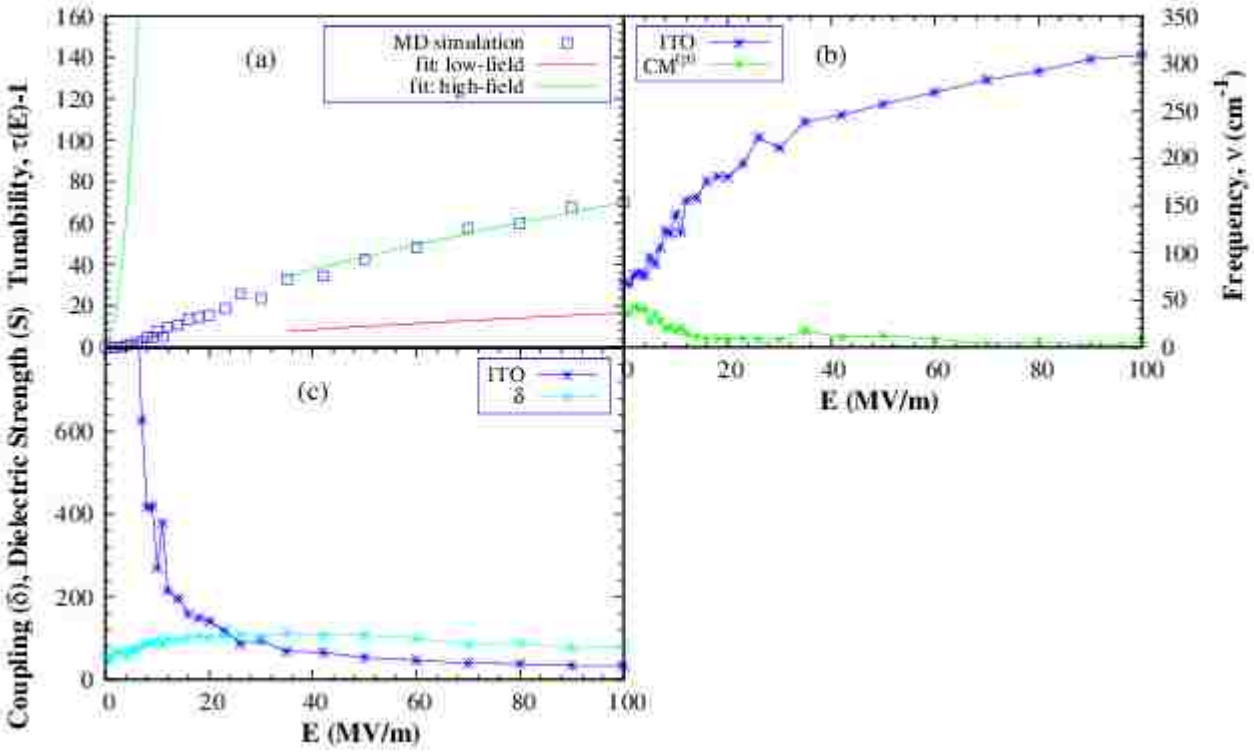

FIGURE 4.2.4. Electric field dependence of dynamical properties of $Ba_{0.5}Sr_{0.5}TiO_3$ bulk at 270 K. Panel (a) displays low-field (red) and high-field (green) Landau-Devonshire fittings of simulation data for tunability. Panel (b) shows resonant frequencies corresponding to peaks of dielectric response. Panel (c) shows dielectric strength of soft-mode and coupling coefficient (δ).

CHAPTER 5

Conclusions

5.1. Disordered Pb(Zr,Ti)O_3 Bulk

In brief, MD simulations incorporating the first-principles alloy effective Hamiltonian were performed for Pb(Zr,Ti)O_3 bulk systems, at finite temperatures for each composition investigated across the MPB. Resonant frequencies and spectral weights of the low frequency modes were determined from the output of the simulations.

The appearance of an unknown low frequency mode in $Pb(Zr_{0.55}Ti_{0.45})O_3$ for temperatures below 200 K was confirmed. The origin of this mode was revealed to be the linear coupling between FE motions and AFD motions, when both degrees of freedom adopt long-range ordering within a R3c space group. Moreover, this additional low frequency mode was shown to involve the R-point AFD mode and to have E(TO) symmetry giving credence to speculations of Bäuerle and Pinczuk through Raman spectroscopic measurements [**54**]. Furthermore resonant frequencies and spectral weights of these two modes were obtained as a function of bias electric field applied along the direction of polarization for this system. Analysis by means of a 2×2 dynamical matrix predicted an electric field induced anti-crossing between the modes and provided more insight into the nature of the coupling.

Moreover, MD simulations conducted for various compositions of Pb(Zr,Ti)O_3 at 10 K confirmed the appearance of additional low frequency polar AFD modes in the dielectric spectra, in systems adopting to both the Cc and I4cm space groups. In particular, a compositional-induced anticrossing is predicted to occur in the Cc state, and the polarity of one mode is expected to significantly decrease and nearly vanish when increasing the Ti composition within the $I4cm$ state. Consistent with group theory, a lifting of degeneracy of E modes into $A' + A''$ modes is also occurring in the Cc state, with the resulting difference in frequency being related to a quantity that we introduced and denote here as the monoclinic

depth and which involves the directions of the polarization and AFD vector. Analytical models were constructed that are based on the linear coupling between FE and AFD motions in structural phases exhibiting both long-range-ordered polarization and oxygen octahedra tiltings. Such analytical models accurately reproduced characteristics of the low-frequency optical modes, and provided more insight into the significant role played by the coupling between ferroelectric and AFD degrees of freedom on such characteristics.

Inspection of dielectric reponses purely in the FE phase derived from MD simulations for compositions across the MPB revealed the existence of two A_1 modes denoted as $A_1^{(1)}$ and $A_1^{(2)}$, instead of the known single A_1 mode. Raman measurements of $Pb(Zr_{0.47}Ti_{0.53})O_3$ validated the doubling of the A_1 mode. It was shown that this doubling of the A_1 modes mostly originates from an interaction between longitudinal FE displacement and transverse AFD motions and that the unusual A_1 mode doubling requires an overtone of the AFD mode to be close to the resonant frequency of the single A_1 mode. Such charactersitics were shown to be in line with the occurrence of a Fermi resonance. This hypothesis was substantiated by the use of an analytical model involving non-linear coupling between FE and AFD motions in a purely FE phase, which unveiled characteristics typical of a Fermi resonance.

The alloy effective Hamiltonian approach has been highly successful in confirming observed phenomena both of static and dynamical nature in $Pb(Zr,Ti)O_3$ near its MPB. Moreover, the nature and origin of such phenomena has been revealed. Therefore, the scheme employed here can serve as a basis for predicting dynamical properties of systems (such as $BiFeO_3$) that exhibit couplings not only between ferroelectric and antiferrodistortive motions but also between ferroelectric and other degrees of freedom (such as magnetic dipoles). In this work, dynamical properties such as the lifting of degeneracy of the E modes in the Cc phase, arising from ferroelectricity has been predicted, of which the occurrence of a Fermi resonance has since been verified. The author thus hopes other predictions made here will soon be verified through measurements, leading to a broadening of the fundamental understanding of this technologically important compound.

5.2. Disordered (Ba,Sr)TiO_3 Bulks and epitaxially strained $SrTiO_3$ thick films

Dielectric responses as a function of Ba composition and temperature of (Ba,Sr)TiO_3 bulk, and the dielectric response of epitaxially strained $SrTiO_3$ films were probed. In strained $SrTiO_3$ films, occurrence of a Debye like relaxational mode (CM) near the Curie temperature T_c, in both PE and FE phases is confirmed. Furthermore, splitting of the soft mode (SM) into out-of-plane and in-plane modes as a result of epitaxial strain is predicted. Splitting of the in-plane SM in the FE phase into two modes is corroborated and it was shown that these modes possess A_1 and B_2 symmetry respectively, while the out-of-plane mode has B_1 symmetry in the FE phase in conformity with group theory predictions.

Analysis of the dielectric response of $Ba_{0.5}Sr_{0.5}TiO_3$ revealed a second CM mode in the FE phase in addition to the reported single CM in $BaTiO_3$. In both the ferroelectric (FE) P4mm and Amm2 phases, modes originating from the soft-mode were shown to have A_1, B_1 and B_2 symmetries, where B_1 corresponds to dipole oscillations perpendicular to the polarization and A_1 corresponds to oscillations parallel to the polarization.

The mechanics of the Curie temperature, T_c, in (Ba,Sr)TiO_3 systems was investigated through close inspection of the effective Hamiltonian of these systems. Microscopic electrostrictive energy of these systems is shown to drive the mechanics of T_c and the type of FE phase transition in these systems. The occurrence and characteristics of the CM in both PE and FE phases were shown to depend on the variations of the strong electrostrictive energy in these systems and the non-existence of CM in other perovskites such as Pb(Zr,Ti)O_3 was linked to the relatively weak electrostriction in these systems.

The dielectric tunability $\tau(E)$, the static dielectric constant $\varepsilon(0)$ and the characteristics of the modes at ν=10 GHz of $SrTiO_3$ bulk, strained $SrTiO_3$ films and $Ba_{0.5}Sr_{0.5}TiO_3$ bulk were obtained as a function of electric field applied along the polarization. SM frequencies as well as CM frequencies for systems investigated were in excellent agreement with spectroscopic measurements. The CM was found to soften somewhat with electric field, in contrast to the common assumption that it is a constant of electric field. The dielectric constant $\varepsilon(0)$ and computations of tunability $\tau(E)$ were in agreement with measurements

for all these systems. In particular, the high tunability resulting from chemical substitution or epitaxial strain in $SrTiO_3$ was confirmed. Fittings of low-field and high-field tunability of $SrTiO_3$ using respective Landau-Devonshire-theory-based formulas gave β values consistent with measurements and showed the validity of the Landau-Devonshire theory. However, similar fittings done for $Ba_{0.5}Sr_{0.5}TiO_3$ and strained $SrTiO_3$ films revealed that Landau-Devonshire theory does not describe the tunabiliy satisfactorily in the low-field regime. In fact, predicted tunability by Landau-Devonshire theory was a couple of orders of magnitude higher than the 'actual' computed tunability. It is claimed that the presence of a strong CM in the low-field regime in these systems causes this discrepancy.

Finally, the alloy effective Hamiltonian scheme used here for BST systems has been highly successful in verifying observations from measurement for dynamical as well as static properties related to the FE soft mode. Such accuracy makes this approach very reliable in uncovering the microscopic origin of observed phenomena as we have seen for the origin of CM discussed here. As of now, although there is not much experimental work published on the technologically important dielectric tunability of these systems, the author is confident the predictions made here in this respect and with respect to mode characteristics will be successfully verified in the near future. The author also believes the incorporation of other degrees of freedom like AFD for example, can lead to deeper fundamental understanding of these systems.

Bibliography

[1] J. Curie and P. Curie, C. R. Acad. Sci. Paris 91, 294 (1880).

[2] J. Valasek, Phys. Rev. 17, 475 (1921).

[3] G. Busch and P. Scherrer, Naturwissenschaft. 23, 737 (1935).

[4] G. Busch, Helv. Phys. Acta. 11, 269 (1938).

[5] B. Wul and I. M. Goldman, C. R. Acad. Sci. URSS. 46, 139; 49, 177 (1945).

[6] M. E. Lines and A. M. Glass, Principles and Applications of Ferroelectrics and Related Materials (Clarendon Press, Oxford, 1977).

[7] P. W. Anderson, In G. Skanavi (Eds.): Fizika Dielectrikov (Akad. Nauk. SSR, Moscow, 1960).

[8] W. Cochran, Adv. Phys. 9, 387 (1960).

[9] L. D. Landau, Phys. Z. Sowjun. 11, 545 (1937).

[10] L. D. Landau, Zh. Eksp. Teor. Fiz. 7, 627 (1937).

[11] A. F. Devonshire, Philos. Mag. 40, 1040 (1949).

[12] A. F. Devonshire, Philos. Mag. 42, 1065 (1951).

[13] A. F. Devonshire, Adv. Phys. 3, 85 (1954).

[14] A. K. Tagantsev , V.O. Sherman, K.F. Astafiev, J. Venkatesh and N. Setter, J. Electroceram. 11, 5-66 (2003).

[15] W.Kohn and L. J. Sham, Phys. Rev. 140, A1133-1138 (1965) .

[16] R. D. King-Smith and D. Vanderbilt, Phys. Rev. B 47, 1651 (1993).

[17] D. Vanderbilt and R. D. King-Smith, Phys. Rev. B 48, 4442 (1993).

[18] R. Resta, Rev. Mod. Phys. 66, 899 (1994).

[19] K. M. Rabe and J. D. Joannopoulos, Phys. Rev. Lett. 59, 570 (1987).

[20] W. Zhong, D. Vanderbilt, and K. M. Rabe, Phys. Rev. Lett. 73, 1861 (1994); Phys. Rev. B 52, 6301 (1995).

[21] P. Ghosez and J. Junquera, In Michael Rieth, Wolfram Schommers (Eds.): Handbook of theoretical and computational nanotechnology (2006).

[22] L. Bellaiche, A. Garcı´a, and D. Vanderbilt, Phys. Rev. Lett. 84, 5427 (2000); Ferroelectrics 266, 41 (2002).

[23] L. Walizer, S. Lisenkov, and L. Bellaiche, Phys. Rev. B 73, 1144105 (2006).

[24] J. Hlinka, T. Ostapchuk, D. Nuzhnyy, J. Petzelt, P. Kuˇzel, C. Kadlec, P. Vanˇek, I. Ponomareva and L. Bellaiche, Phys. Rev. Lett. 101, 167402 (2008).

[25] S. Tinte, M. G. Stachiotti, M. Sepliarsky, R. L. Migoni, and C. O. Rogrguez, J. Phys.: Condens. Matter 11, 9679 (1999).

[26] I. Grinberg, V. R. Cooper, and A. M. Rappe, Nature (London) 419, 909 (2002).

[27] D. Vanderbilt, Phys. Rev. B 41, R7892(1990).

[28] P. Hohenberg and W. Kohn, Phys. Rev. 136, B864 (1964); W. Kohn and L. J. Sham, ibid. 140, A1133 (1965).

[29] L. Bellaiche and D. Vanderbilt, Phys. Rev. B 61, 7877 (2000).

[30] N. Metropolis, A. W. Rosenbluth, M. N. Rosenbluth, A. H. Teller, and E. Teller, J. Chem. Phys. 21, 1087 (1953).

[31] I. Ponomareva, L. Bellaiche, T. Ostapchuk, J. Hlinka, and J. Petzelt, Phys. Rev. B 77, 012102 (2008).

[32] D. Wang, J. Weerasinghe, L. Bellaiche, and J. Hlinka, Physical Review B 83, 020301(R) (2011).

[33] N. J. Ramer and A. M. Rappe, J. Phys. Chem. Solids 61, 317 (2000).

[34] L. Walizer, Dissertation: Modeling of Compositionally Graded Barium Strontium Titanate from First Principles, University of Arkansas (2009).

[35] D. Rapaport, The Art of Molecular Dynamics Simulation Cambridge University Press, Cambridge, (2001).

[36] W. G. Hoover, A. J. C. Ladd, and B. Moran, Phys. Rev. Lett. 48, 1818 (1982).

[37] D. J. Evans, J. Chem. Phys. 78, 3297 (1983).

[38] I. A. Kornev, L. Bellaiche, P.-E. Janolin, B. Dkhil, and E. Suard, Phys. Rev. Lett. 97, 157601 (2006).

[39] L. Bellaiche, A. Garcı´a, and D. Vanderbilt, Phys. Rev. Lett. 84, 5427 (2000); Ferroelectrics 266, 41 (2002).

[40] B. Noheda, L. Wu, and Y. Zhu, Phys. Rev. B 66, 060103 (2002).

[41] M. Deluca, H. Fukumura, N. Tonari, C. Capiani, N. Hasuike, K. Kisoda, C. Galassi, and H. Harima, J. Raman Spectros. 42, 488 (2010).

[42] B. Noheda, J. A. Gonzalo, L. E. Cross, R. Guo, S.-E. Park, D. E. Cox, G. Shirane, Phys. Rev. B61, 8687(2000).

[43] B. Noheda, Curr. Opin. Solid StateMater. Sci. 6, 27 (2002).

[44] F. Cordero, F. Craciun, C. Galassi, Phys. Rev. Lett. 98, 255701 (2007).

[45] G. Fraysse, J. Haines, V. Bornand, J. Rouquette,M. Pintard, Ph. Papet, S. Hull, Phys. Rev. B 77, 064109 (2008).

[46] K. C. V. Lima, A. G. Filho, A. P. Ayala, J. Mendes Filho, P. T. Freire, F. E. Melo, E. B. Arajo, and J. A. Eiras, Phys. Rev. B 63, 184105 (2001).

[47] D. I. Woodward, J. Knudsen, and I. M. Reaney, Phys. Rev. B 72, 104110 (2005).

[48] E. Buixaderas, D. Nuzhnyy, J. Petzelt, Li Jin, and D. Damjanovic, Phys. Rev. B. 84, 184302 (2011).

[49] Phase Transitions and Critical Phenomena, edited by C. Domb and M. S. Green (Academic, New York, 1972), Vol. I-V.

[50] O.G. Vendik, L.T. Ter-martirosyan, and S.P. Zubko, J. Appl. Phys., 84, 993 (1998).

[51] O.G. Vendik, Sov. Phys. Solid State, 14, 849 (1972).

[52] A. B. Sushkov, M. Mostovoy, R. V. Aguilar, S.-W. Cheong, and H. D. Drew, J. Phys. Condens. Matter 20, 434210 (2008).

[53] V. Sivasubramanian, V. R. K. Murthy, B. Viswanathan, and M. Sieskind, J. Phys. Condens. Matter 8, 2447 (1996).

[54] D. Bäuerle and A. Pinczuk, Solid State Commun. 19, 1169 (1976).

[55] P. A. Fleury, J. F. Scott, and J. M. Worlock, Phys. Rev. Lett. 21, 16 (1968).

[56] J. Petzelt and V. Dvorak, J. Phys. C 9, 1571 (1976).

[57] J. Weerasinghe, D. Wang, and L. Bellaiche, Physical Review B 85, 014301 (2012).

[58] C. Cohen-Tannoudji, B. Diu, and F. Laloe, Quantum Mechanics (Hermann, Paris, 1977), Vol. I.

[59] D. Wang, E.Buxideras, J. Íñiguez, J. Weerasinghe, H. Wang, and L. Bellaiche, Phys. Rev. Lett. 107, 175502 (2011).

[60] J. Meng, R. Katiyar, G. Zou, and X. Wang, Phys. Status Solidi (a) 164, 851 (1997).W. Hayes and R. Loudon, Scattering of Light by Crystals (Wiley, New York, 1978).

[61] J. Frantti et al., Jpn. J. Appl. Phys. 38, 5679 (1999).

[62] E. Fermi, Z. Phys. 71, 250 (1931).

[63] E. Wilson, Phys. Rev. 46, 146 (1934).

[64] W. Low, Phys. Rev. 97, 1664 (1955).

[65] G. M. Gale, P. Guyot-Sionnest, W. Q. Zheng, and C. Flytzanis, Phys. Rev. Lett. 54, 823 (1985).

[66] A. Yaremko and D. Ostrovskii, J. Phys. Condens. Matter 7, 7833 (1995).

[67] A. Yaremko, J. Mol. Struct. 511–512, 57 (1999).

[68] S. Prants, J. Phys. B 21, 397 (1988).

[69] V. V. Lemanov, E. P. Smirnova, P. P. Syrnikov, and E. A. Tarakanov, Phys. Rev. B 54, 3151(1996).

[70] J.H. Haeni, P. Irvin, W. Chang, R. Uecker, P. Reiche, Y.L. Li, S. Choudhury, W. Tian, M.E. Hawley, B. Craigo, A.K. Tagantsev, X.Q. Pan, S.K. Streiffer, L.Q. Chen, S.W. Kirchoefer, J. Levy and D.G. Schlom, Nature, 430, 758 (2004).

[71] D. Nuzhnyy, J. Petzelt, S. Kamba, P. Kužel,1 C. Kadlec, V. Bovtun, M. Kempa, J. Schubert, C. M. Brooks, and D. G. Schlom, APL, 95, 232902 (2009).

[72] C. Menoret, J. M. Kiat, B. Dkhil, M. Dunlop, H. Dammak, and O. Hernandez, Phys. Rev. B 65, 224104(2002).

[73] S. Lisenkov, I. Ponomareva and L. Bellaiche, Conference proceedings (IEEE), DOD HPCMP, 2011 Users Group Conference (2011).

[74] T. Ostapchuk, J. Petzelt, J. Hlinka, V. Bovtun, P. Kuzel, I. Ponomareva, S. Lisenkov, L. Bellaiche, A. Tkach, and P. Vilarinho, J. Phys. Condens. Matter 21, 474215 (2009).

[75] P. Kužel, F.Kadlec, Comptes Rendus Physique, 9, 197-214 (2008).

[76]

[77] P. Kuˇzel, F. Kadlec, J. Petzelt, J. Schubert and G. Panaitov, Appl. Phys. Lett. 91 232911 (2007).

[78] C. Kadlec, F. Kadlec, H. Nemec, P. Kuˇzel, J. Schubert, and G Panaitov, J. Phys.: Condens. Matter, 21, 115902 (2009).

[79] Jingji Zhang, Jiwei Zhai, Xiujian Chou, Jun Shao, Xiang Lu, Xi Yao, Acta Materialia, 57, 4491–4499 (2009).

APPENDIX A

In order to gain insight into the low frequency peaks appearing in the dielectric responses of $Pb(Zr,Ti)O_3$, one needs to determine the essential form of the contribution from FE-AFD coupling term of the effective Hamiltonian, and examine the resulting dynamical equations for the FE and AFD motions. The FE-AFD coupling, E_C, is given by:

$$E_C\left(\{u_i\},\{\omega_i\}\right)=\sum_i\sum_{\alpha,\beta,\gamma,\delta}D_{\alpha\beta\gamma\delta}\omega_{i,\alpha}\omega_{i,\beta}u_{i,\gamma}u_{i,\delta} \tag{A.0.1}$$

Linear Coupling

In structural phases that exhibit both long-range ordered FE and AFD motions (such as $R3c$, $I4cm$ and Cc), FE and AFD motions at site i can be represented as:

$$\begin{cases}\mathbf{u_i}\left(\mathbf{t}\right)=\langle\mathbf{u}\rangle+\tilde{\mathbf{u}}_\mathbf{i}\left(\mathbf{t}\right)\\ \boldsymbol{\omega}_\mathbf{i}\left(\mathbf{t}\right)=\langle\boldsymbol{\omega}_\mathbf{R}\rangle+\tilde{\boldsymbol{\omega}}_\mathbf{i}\left(\mathbf{t}\right)\end{cases} \tag{A.0.2}$$

where t represents time, $\langle\mathbf{u}\rangle$ and $\langle\boldsymbol{\omega}_\mathbf{R}\rangle$ are the equilibrium, spontaneous values of the FE and AFD motions, respectively. Finally, $\tilde{\mathbf{u}}_\mathbf{i}$ and $\tilde{\boldsymbol{\omega}}_\mathbf{i}$ are the deviations of the FE motions and AFD motions at site i, respectively, from their equilibrium values. Plugging Eqn.(A.0.2) into Eqn.(A.0.1) and expanding, for the essential form of the expression, we have:

(A.0.3)

$$\begin{aligned}E_C=\ &\textstyle\sum_i\sum_{\alpha,\beta,\gamma,\delta}\left(D_{\alpha\beta\gamma\delta}\left\langle\omega_{\mathbf{i},\alpha,\mathbf{R}}\right\rangle\left\langle\omega_{\mathbf{i},\beta,\mathbf{R}}\right\rangle\right)\tilde{u}_{i,\gamma}\tilde{u}_{i,\delta} &&+\textstyle\sum_i\sum_{\alpha,\beta,\gamma,\delta}\left(D_{\alpha\beta\gamma\delta}\left\langle\omega_{\mathbf{i},\alpha,\mathbf{R}}\right\rangle\left\langle u_{i,\delta}\right\rangle\right)\tilde{\omega}_{i,\beta}\tilde{u}_{i,\gamma}\\ &\textstyle+\sum_i\sum_{\alpha,\beta,\gamma,\delta}\left(D_{\alpha\beta\gamma\delta}\left\langle\omega_{\mathbf{i},\alpha,\mathbf{R}}\right\rangle\left\langle u_{i,\gamma}\right\rangle\right)\tilde{\omega}_{i,\beta}\tilde{u}_{i,\delta} &&+\textstyle\sum_i\sum_{\alpha,\beta,\gamma,\delta}\left(D_{\alpha\beta\gamma\delta}\left\langle\omega_{\mathbf{i},\beta,\mathbf{R}}\right\rangle\left\langle u_{i,\delta}\right\rangle\right)\tilde{\omega}_{i,\alpha}\tilde{u}_{i,\gamma}\\ &\textstyle+\sum_i\sum_{\alpha,\beta,\gamma,\delta}\left(D_{\alpha\beta\gamma\delta}\left\langle\omega_{\mathbf{i},\beta,\mathbf{R}}\right\rangle\left\langle u_{i,\gamma}\right\rangle\right)\tilde{\omega}_{i,\alpha}\tilde{u}_{i,\delta} &&+\textstyle\sum_i\sum_{\alpha,\beta,\gamma,\delta}\left(D_{\alpha\beta\gamma\delta}\left\langle u_{i,\gamma}\right\rangle\left\langle u_{i,\delta}\right\rangle\right)\tilde{\omega}_{i,\alpha}\tilde{\omega}_{i,\beta}\end{aligned}$$

where the first order terms of $\tilde{u}_{i,\alpha}$ and $\tilde{\omega}_{i,\alpha}$ disappears because equilibrium conditions require that $\partial E_{FE-AFD}/\partial\tilde{u}_{i,\alpha} = 0$ and $\partial E_{FE-AFD}/\partial\tilde{\omega}_{i,\alpha} = 0$. Although the first and last terms in Eqn.(A.0.3) can influence the natural frequencies of the soft mode and AFD mode. The remaining peaks are of particular significance, since they will give rise to new resonance peaks in the dielectric response arising from AFD motions. They show that the *linear* coupling between FE and AFD motions can be collectively taken to have the form:

$$H_{\text{FE-AFD}} \simeq \sum_i \kappa \left|\langle \boldsymbol{u} \rangle\right| \left|\langle \boldsymbol{\omega_R} \rangle\right| \tilde{\mathbf{u}}_\mathbf{i} \cdot \tilde{\boldsymbol{\omega}}_\mathbf{i}, \tag{A.0.4}$$

where κ is a constant depending on the $D_{\alpha\beta\gamma\delta}$ matrix.

Non-linear coupling [59]

In structural phases that exhibit only long-range ordered FE motions (such as $R3m$, $P4mm$ and Cm), FE and AFD motions at site i can be represented as:

$$\begin{cases} \mathbf{u}_i(t) = \langle \mathbf{u} \rangle + \tilde{\mathbf{u}}_i(t) & , \\ \boldsymbol{\omega}_i(t) = \langle \boldsymbol{\omega}_i \rangle + \tilde{\boldsymbol{\omega}}_i(t) = \tilde{\boldsymbol{\omega}}_i(t) & . \end{cases} \tag{A.0.5}$$

where $\langle \boldsymbol{\omega}_i \rangle = 0$. The dynamic equation for $\mathbf{u}_i(t)$ is given by

$$\frac{d^2}{dt^2} u_{i,\delta} = \ldots - 2 \sum_{i,\alpha,\beta,\gamma} D_{\alpha\beta\gamma\delta} \omega_{i,\alpha} \omega_{i,\beta} u_{i,\gamma} + \ldots, \tag{A.0.6}$$

where only the term due to the FE-AFD non-linear couplings is explicitly shown. Plugging Eq. (A.0.5) into the above equation gives:

$$\begin{aligned} \frac{d^2}{dt^2} \tilde{u}_{i,\delta}(t) = \ldots &- 2 \sum_{i,\alpha,\beta,\gamma} D_{\alpha\beta\gamma\delta} \tilde{\omega}_{i,\alpha} \tilde{\omega}_{i,\beta} \langle u \rangle_\gamma \\ &- 2 \sum_{i,\alpha,\beta,\gamma} D_{\alpha\beta\gamma\delta} \tilde{\omega}_{i,\alpha} \tilde{\omega}_{i,\beta} \tilde{u}_{i,\delta} \ldots . \end{aligned} \tag{A.0.7}$$

Assuming $\tilde{\mathbf{u}}_i(t)$ is small compared to $\langle \mathbf{u} \rangle$, we can neglect the last term in Eq. (A.0.7), having

$$\frac{d^2}{dt^2}\tilde{u}_{i,\delta}(t) \simeq \ldots - 2\sum_{i,\alpha,\beta,\gamma} D_{\alpha\beta\gamma\delta}\tilde{\omega}_{i,\alpha}\tilde{\omega}_{i,\beta}\langle u \rangle_\gamma . \tag{A.0.8}$$

For $\boldsymbol{\omega}_i(t)$, there is a similar equation. We then find that, if we view $\tilde{\mathbf{u}}_i(t)$ and $\boldsymbol{\omega}_i(t)$ as dynamic variables, the essential FE-AFD non-linear coupling term that governs the dynamics of $\tilde{\mathbf{u}}_i$ and $\tilde{\boldsymbol{\omega}}_i$ has the following form

$$H_{FE-AFD} = \sum_i \kappa \langle u \rangle \tilde{u}_i (\tilde{\omega}_i)^2 , \tag{A.0.9}$$

Analytical solution to the non-linear dynamical equations [59]

To better understand the non-linear coupling between the local mode and the antiferrodistortions (AFD) motions, let's adopt a simplified model whose dynamics can effectively represent that of the whole system, in which $\tilde{u}_i$ and $\tilde{\omega}_i$ are the two coupled dynamical variables and the coupling term is given in Eqn. (A.0.9).

The dynamical equations for $\tilde{u}$ and $\tilde{\omega}$ (we remove the subscript i hereafter to simplify notations) are given, in the limit of small *ac* electric fields, by:

$$\begin{cases} \frac{d^2\tilde{u}}{dt^2} = & -4\pi^2 \left(\nu_r^{\mathrm{FE}}\right)^2 \tilde{u} - \frac{\kappa\langle u \rangle}{m_{\tilde{u}}}\tilde{\omega}, \\ \frac{d^2\tilde{\omega}}{dt^2} = & -4\pi^2 \left(\nu_r^{\mathrm{AFD}}\right) \tilde{\omega} - \frac{2\kappa\langle u \rangle \tilde{u}\tilde{\omega}}{m_{\tilde{\omega}}}, \end{cases} \tag{A.0.10}$$

where ν_r^{FE} (respectively, ν_r^{AFD}) is the frequency of the electric dipole (respectively, AFD motions) that is related to the derivatives of the E_{FE} (respectively, E_{AFD}) energy term, and $m_{\tilde{u}}$ (respectively, $m_{\tilde{\omega}}$) is the effective mass associated with the local soft mode (respectively, AFD distortions).

To further analyze Eqs. (A.0.10), which are coupled non-linear differential equations, we Fourier-transform to the frequency representation and obtain, using the convolution theorem:

$$\text{(A.0.11)} \qquad \begin{cases} -\nu^2 \rho_{\tilde{u}}(\nu) = & -\left(\nu_r^{\mathrm{FE}}\right)^2 \rho_{\tilde{u}}(\nu) - \frac{\kappa\langle u\rangle}{4\pi^2 m_{\tilde{u}}} \int_{-\infty}^{\infty} \rho_{\tilde{\omega}}(\nu')\, \rho_{\tilde{\omega}}(\nu-\nu')\, d\nu', \\ -\nu^2 \rho_{\tilde{\omega}}(\nu) = & -\left(\nu_r^{\mathrm{AFD}}\right)^2 \rho_{\tilde{\omega}}(\nu) - \frac{\kappa\langle u\rangle}{2\pi^2 m_{\tilde{\omega}}} \int_{-\infty}^{\infty} \rho_{\tilde{u}}(\nu')\, \rho_{\tilde{\omega}}(\nu-\nu')\, d\nu', \end{cases}$$

where $\rho_{\tilde{u}}(\nu) = \int_{-\infty}^{\infty} \tilde{u}(t) \exp(-i2\pi\nu t)\, dt$ and $\rho_{\tilde{\omega}}(\nu) = \int_{-\infty}^{\infty} \tilde{\omega}(t) \exp(-i2\pi\nu t)\, dt$.

While the spectral densities $\rho_{\tilde{\omega}}(\nu)$ and $\rho_{\tilde{u}}(\nu)$ are in principle arbitrary, we know they present their maximum values for frequencies around ν_r^{AFD} and ν_r^{FE}, respectively. This implies that, for example, the product $\rho_{\tilde{u}}(\nu')\, \rho_{\tilde{\omega}}(\nu-\nu')$ will be significant only if $\nu' \simeq \nu_r^{\mathrm{FE}}$ and $\nu - \nu' \simeq \nu_r^{\mathrm{AFD}}$, which results in the condition $\nu \simeq \nu_r^{\mathrm{FE}} + \nu_r^{\mathrm{AFD}}$. This means that, according to the second equation in Eq. (A.0.11), the FE-AFD coupling will modify the spectrum of the AFD mode at frequencies $\nu_r^{\mathrm{FE}} + \nu_r^{\mathrm{AFD}}$ that will be well separated from the main AFD spectral feature at ν_r^{AFD} *unless* $\nu_r^{\mathrm{FE}} \simeq 0$. In our case, because ν_r^{FE} is large for the temperature range of interest (cf. Fig. 3.5.2 in section (3.5)), the equation ρ_ω can be approximately written as

$$\text{(A.0.12)} \qquad -\nu^2 \rho_{\tilde{\omega}}(\nu) = -\left(\nu_r^{\mathrm{AFD}}\right)^2 \rho_{\tilde{\omega}}(\nu),$$

which represents a well defined harmonic oscillator in the frequency space.

A similar analysis shows that the non-linear coupling term in the equation for $\rho_{\tilde{u}}$ will play a significant role for frequencies $\nu \simeq \nu_r^{\mathrm{FE}} \simeq 2v_r^{\mathrm{AFD}}$. Hence, in this case, the FE-AFD coupling affects the spectral density of the FE mode near its maximum, making it doubly-peaked. Indeed, we can rewrite the first line in Eq. (A.0.11) and readily identify the resonant frequencies for $\tilde{u}$. We have

$$\text{(A.0.13)} \qquad \left[\nu^2 - \left(\nu_r^{\mathrm{FE}}\right)^2\right] = \frac{\kappa\langle u\rangle}{4\pi^2 m_{\tilde{u}} \rho_{\tilde{u}}(\nu)} \int_{-\infty}^{\infty} \rho_{\tilde{\omega}}\left(\nu'\right) \rho_{\tilde{\omega}}\left(\nu-\nu'\right) d\nu',$$

and, because $\rho_{\tilde{\omega}}(-\nu) = \rho^*_{\tilde{\omega}}(\nu)$, we also have

$$\left[\nu^2 - \left(\nu_r^{\mathrm{FE}}\right)^2\right] = \frac{\kappa \langle u \rangle}{4\pi^2 m_{\tilde{u}} \rho^*_{\tilde{u}}(\nu)} \left[\int_{-\infty}^{\infty} \rho_{\tilde{\omega}}\left(\nu'\right) \rho_{\tilde{\omega}}\left(\nu - \nu'\right) d\nu'\right]^*. \tag{A.0.14}$$

Eqs. (A.0.13) and (A.0.14) can then be combined to yield

$$\left[\nu^2 - \left(\nu_r^{\mathrm{FE}}\right)^2\right]^2 = \Omega^4, \tag{A.0.15}$$

with

$$\Omega^2 \simeq \left| \frac{\kappa \langle u \rangle \rho^2_{\tilde{\omega}}\left(\nu_r^{\mathrm{FE}}/2\right) \Delta\nu}{4\pi^2 m_{\tilde{u}} \rho_{\tilde{u}}\left(\nu_r^{\mathrm{FE}}\right)} \right| \tag{A.0.16}$$

where $\Delta\nu$ is the range of frequency in which the integrand $\rho_{\tilde{\omega}}(\nu')\rho_{\tilde{\omega}}(\nu - \nu')$ has significant values.

Thus, the resonance frequencies for the A_1 ferroelectric mode(s) are doubled and given by:

$$\nu^2 = \left(\nu_r^{\mathrm{FE}}\right)^2 \pm \Omega^2. \tag{A.0.17}$$

To obtain an explicit expression for Ω^2, we can assume that $\rho_{\tilde{u}}$ and $\rho_{\tilde{\omega}}$ have distribution that describes damped harmonic oscillators, e.g., Lorentzian functions with damping coefficients. As a result,

$$\rho_{\tilde{u}}\left(\nu_r^{\mathrm{FE}}\right) \simeq \frac{S_{\tilde{u}}}{\left(\nu_r^{\mathrm{FE}}\right)^2 - \left(\nu_r^{\mathrm{FE}}\right)^2 + i\gamma_{\tilde{u}}\nu_r^{\mathrm{FE}}} = \frac{S_{\tilde{u}}}{i\gamma_{\tilde{u}}\nu_r^{\mathrm{FE}}}, \tag{A.0.18}$$

$$\rho_{\tilde{\omega}}\left(\nu_r^{\mathrm{FE}}/2 \simeq \nu_r^{\mathrm{AFD}}\right) \simeq \frac{S_{\tilde{\omega}}}{i\gamma_{\tilde{\omega}}\nu_r^{\mathrm{AFD}}}. \tag{A.0.19}$$

This results in

$$\Omega^2 \simeq \left| \frac{\kappa \langle u \rangle}{\pi^2 m_{\tilde{u}}} \frac{\gamma_{\tilde{u}}}{\gamma^2_{\tilde{\omega}}} \frac{S^2_{\tilde{\omega}}}{S_{\tilde{u}}} \frac{\Delta\nu}{\nu_r^{\mathrm{FE}}} \right|. \tag{A.0.20}$$

let's conclude by noting that the above argument and formulas differ in some ways from the usual derivation of the Fermi-resonance frequency splitting that one can find in the literature. When discussing a Fermi resonance in molecules or molecular crystals, it is common to solve the non-linear dynamical equations by assuming a strong resonance condition (i.e., $\nu_r^{\mathrm{FE}} = 2\nu_r^{\mathrm{AFD}}$) and/or a single-frequency approximation for the spectral density of the oscillators involved. However, such approximations are clearly incompatible with the results of our simulations; we thus needed to consider a more general and complex scenario.